Chem Soc Rev

REVIEW ARTICLE

View Article Online
View Journal | View Issue

Cite this: *Chem. Soc. Rev.*, 2025, **54**, 12080

Twisted intramolecular charge transfer (TICT) based fluorescent probes and imaging agents

Yueci Wu, [ab] Han-Min Wang, [ceh] Xi-Le Hu, [d] Yi Zang, [f] Jia Li, *[ceh] Hai-Hao Han, *[ceh] Xiao-Peng He, *[dg] Simon E. Lewis, *[a] Hanafy M. Ismail *[b] and Tony D. James *[ai]

Received 16th July 2025

DOI: 10.1039/d3cs01118f

rsc.li/chem-soc-rev

Twisted Intramolecular charge transfer (TICT)-based fluorescent probes are crucial in chemical sensing due to their sensitivity and specificity. These probes undergo conformational changes upon interacting with target analytes, resulting in measurable fluorescence responses. Their environment-dependent emission characteristics make them ideal for detecting variations in solvent polarity, microviscosity, and specific chemical species. Recent advances have expanded their applications to organic optoelectronics and non-linear optics. This review discusses the design principles, mechanisms, and applications of TICT-based probes, emphasizing their role in detecting cations, anions, and neutral molecules. We describe their advantages, such as fluorescence turn-on or turn-off responses and potential for ratiometric detection, which inherently corrects for interferences. Challenges in developing these probes, including fluorescence quantum yield and photostability, are also addressed. Potential directions for future research are highlighted, including the need for improved biocompatibility and multimodal imaging capabilities, with the aim of enhancing their utility in environmental monitoring, biomedical research, and clinical diagnostics.

1. Introduction

With the concept of fluorescence proposed by Sir George Gabriel Stokes in 1845 and additional reports about the observed fluorescence in natural compounds, the modern theoretical understanding of fluorescence began to take shape and continues to develop to this day.[1–4] The characteristics of the phenomenon of fluorescence make it a potential tool for the visual detection of target analytes, especially against dark backgrounds. At the same time, the structures of fluorescent probes can be varied to facilitate control over excitation and emission wavelengths, chemical reactivity and localization, enabling highly selective and easy-to-observe detection methods for target analytes.[5,6] Therefore, over the past several decades, fluorescent probes have been widely used in chemical biology, biochemistry, pharmacology, environmental science and medical theranostics, due to their advantages in terms of low cost, ease of operation, high sensitivity, non-invasiveness and the ability to monitor biological processes *in situ*.[7–10] Generally, the most commonly exploited mechanisms of fluorescence in fluorescent probe design include PeT (Photoinduced Electron Transfer), ICT (Internal Charge Transfer), FRET (Föster Resonance Energy Transfer), AIE (Aggregation-Induced Emission) and ESIPT (Excited-State Intramolecular Proton Transfer). In this review, we focus on fluorescent probes based on twisted intramolecular charge transfer (TICT), or combined mechanisms (AIE/TICT and PeT/TICT) for detecting biologically and/or environmentally important species.

1.1 Fluorescence of DMABN

Half a century ago, Lippert *et al.* discovered that 4-(dimethylamino)benzonitrile (**DMABN**) has dual fluorescence emission, consisting of two bands: the A band (^1L_a) with a longer

[a] *Department of Chemistry, University of Bath, Bath, BA2 7AY, UK. E-mail: t.d.james@bath.ac.uk, s.e.lewis@bath.ac.uk*
[b] *Vector Biology, Liverpool School of Tropical Medicine, Liverpool, L3 5QA, UK. E-mail: hanafy.ismail@lstmed.ac.uk*
[c] *Shandong Laboratory of Yantai Drug Discovery, Bohai Rim Advanced Research Institute for Drug Discovery, Yantai, Shandong 264117, P. R. China. E-mail: jli@simm.ac.cn, hanhaihao@simm.ac.cn*
[d] *Key Laboratory for Advanced Materials and Joint International Research Laboratory of Precision Chemistry and Molecular Engineering, Feringa Nobel Prize Scientist Joint Research Center, Frontiers Center for Materiobiology and Dynamic Chemistry, School of Chemistry and Molecular Engineering, East China University of Science and Technology, 130 Meilong Rd., Shanghai 200237, P. R. China. E-mail: xphe@ecust.edu.cn*
[e] *Molecular Imaging Center, National Center for Drug Screening, State Key Laboratory of Chemical Biology, Shanghai Institute of Materia Medica, Chinese Academy of Sciences, Shanghai 201203, P. R. China*
[f] *Lingang laboratory, Shanghai, 201203, P. R. China*
[g] *The International Cooperation Laboratory on Signal Transduction, National Center for Liver Cancer, Eastern Hepatobiliary Surgery Hospital, Shanghai 200438, P. R. China*
[h] *University of Chinese Academy of Sciences, No. 19A Yuquan Road, Beijing 100049, P. R. China*
[i] *School of Chemistry and Chemical Engineering, Henan Normal University, Xinxiang 453007, P. R. China*

"anomalous" wavelength and a B band (^1L_b) with a shorter "normal" wavelength.[11,12] This kind of dual fluorescence could be fine-tuned using solvents of different polarities (Fig. 1(A) and (B)).[12,13] In nonpolar solvents, **DMABN** emits only B band fluorescence. When dissolved in more polar solvents, the A band appears and undergoes a red shift as the polarity of the solvent increases. At the same time, the fluorescence intensity ratio of the A band to the B band increases.[14,15]

1.2 Mechanism of TICT

Subsequently, Grabowaski *et al.* studied **DMABN** and proposed the mechanism of TICT.[16,17] As shown in Fig. 2, **DMABN** is

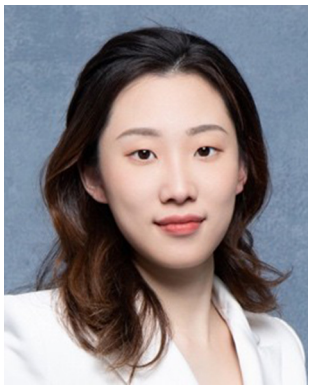

Yueci Wu

Yueci Wu is a postdoctoral research associate working under the supervision of Dr. Hanafy M. Ismail at Vector Biology, Liverpool School of Tropical Medicine. She received her PhD in 2023 from the University of Bath under the supervision of Prof. Tony D. James. Her research interests include developing novel chemical sensors for detecting reactive oxygen species, advancing the development of photoaffinity labelling probes and protein degraders for uncovering insecticide resistance in malaria vectors, and pharmacokinetic analysis.

Han-Min Wang

Han-Min Wang is a postdoctoral research fellow working under the supervision of Prof. Jia Li. Her research focuses on the biological research of new targets for MASH treatment and development of new chemical probe tools for monitoring the development of MASH.

Xi-Le Hu

Xi-Le Hu obtained his PhD in 2017 from ECUST. His research mainly focuses on construction of new methods and technologies for the diagnosis and treatment of superbugs.

Yi Zang

Yi Zang obtained her PhD from SIMM (CAS) in 2008 and is currently a professor at Lingang Laboratory. Her research mainly focuses on the biological research of AMPK, drug discovery for organ fibrosis and development of new chemical biology probe tools.

Jia Li

Jia Li received his PhD from SIMM (CAS) in 2000 and was promoted to professor in 2005. He has been the director of SIMM (CAS) since 2019. His research interests are centered on the investigation of mechanisms of metabolic diseases and medicinal chemical biology.

Hai-Hao Han

Hai-Hao Han is an Associate Professor at SIMM (CAS). He received his PhD in 2020 from ECUST under the supervision of Prof. Xiao-Peng He. His research interests include glycosylated fluorescent probes for disease theranostic applications and targeted drug development.

excited into the locally excited state (LE) from the ground state (GS) upon photoexcitation. In nonpolar solvents, the molecule tends to keep a coplanar conformation stabilized by electronic conjugation so that only the B band can be observed. In contrast, in polar solvents, because of the unstable coplanar conformation, the dimethylamino group will twist so that the dihedral angle between the benzonitrile and dimethylamino motifs will change from planar to perpendicular. Due to this structural change, the ICT process will be promoted. At the same time, the electron will transfer from the dimethylamino group (the electron donor) to the benzonitrile group (the electron acceptor).[14,18] A distribution between the two geometries occurs, which ultimately results in the dual fluorescence: the fluorescence emission of the B band, produced by the radiative transition from LE/ICT to GS, and the other fluorescence emission of the A band, produced by the radiative transition from TICT to GS′. Alternatively, the molecule may relax from TICT to GS′ through nonradiative decay, which would lead to a fluorescence quenching of the A band.[18] In TICT fluorescence, the quasi-planar emission state is defined as the "LE" state in nonpolar molecules, whereas it is defined as the "ICT" state in dipolar molecules.[14,19]

Because of the geometric structural change from the ground state to the TICT state, the emission from the TICT state usually has a red shift, which results in a large Stokes shift.[19] At the same time, this kind of emission shift can be used to generate systems exhibiting near infrared emission which is helpful for detection and tracking *in vivo*.[19–21] Due to intramolecular charge transfer being affected by the polarity of solvents, TICT-based fluorophores are sensitive to their local environment.[22–27] Significantly, the dual emission of TICT-based fluorophores can enable ratiometric detection. Pointedly, ratiometric fluorescent probes can avoid interference and ensure more reliable and accurate results, due to the built-in correction.[22,27–31] On the other hand, the nonradiative decay from TICT to GS′ contributes to an increase in heat production, which can lead to applications in photothermal therapy (PTT).[21,32–35] Nevertheless, due to radiationless transitions, the fluorescence quantum yield of TICT-based fluorophores can be low.[21]

Xiao-Peng He

Xiao-Peng He is a professor at Feringa Nobel Prize Scientists Research Center, ECUST. He obtained his BSc (2006) and PhD (2011) from ECUST. He conducted postdoctoral research with Kaixian Chen (SIMM, CAS) from 2011 to 2013 at ECUST. With >200 papers published in peer-reviewed journals, his research interests are chemical techniques for the glycomics and targeted delivery of diagnostic and therapeutic agents.

Simon E. Lewis

Simon Lewis is a Professor of organic chemistry at the University of Bath. His research concerns the use of azulene as both a colorimetric and fluorescent reporter motif in chemosensors and chemodosimeters. Azulene-containing probes have been developed in the Lewis lab for a variety of applications including bioimaging, detection of contaminants in drinking water, and detection of environmentally important analytes in a marine context.

Hanafy M. Ismail

Hanafy M. Ismail is a Lecturer at the Liverpool School of Tropical Medicine (LSTM) and a Member of the Royal Society of Chemistry (MRSC). He leads the Chemical Biology Group (HI-Lab), where his research focuses on elucidating the molecular mechanisms of insecticide resistance in mosquitoes. His group develops and applies cutting-edge chemical biology tools, integrated with genetic and pharmacokinetic approaches, to understand resistance and develop sustainable malaria control solutions.

Tony D. James

Tony D. James is a Professor at the University of Bath and Fellow of the Royal Society of Chemistry. He received the Daiwa-Adrian Prize for developing scientific networks with Japan in 2013, the inaugural CASE Prize for establishing scientific networks with China in 2015, the MSMLG Czarnik Award in 2018, the Frontiers in Chemistry Diversity Award in 2020, a Royal Society Wolfson Research Merit Award (2017–2022), is an Ewha Womans University Global Fellow and has a h-index of 101.

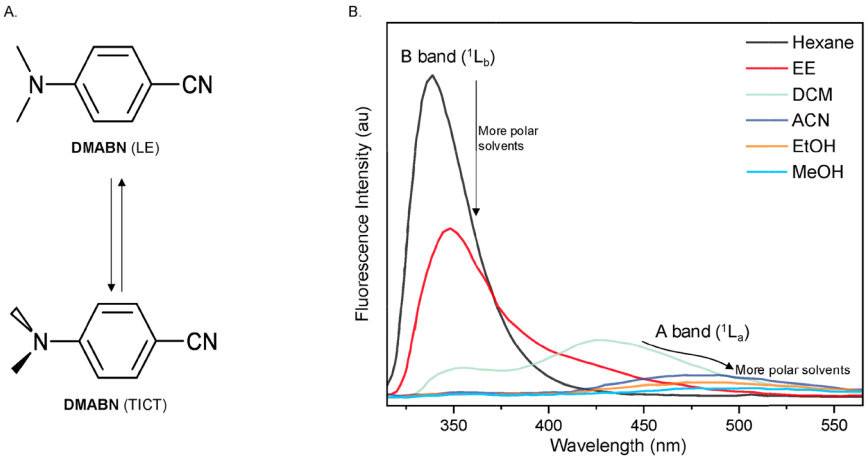

Fig. 1 (A) Excited-state equilibrium of **DMABN**. (B) Fluorescence spectrum of **DMABN** in different solvents (hexane = *n*-hexane, EE = diethyl ether, DCM = dichloromethane, ACN = acetonitrile, EtOH = ethanol, MeOH = methanol).

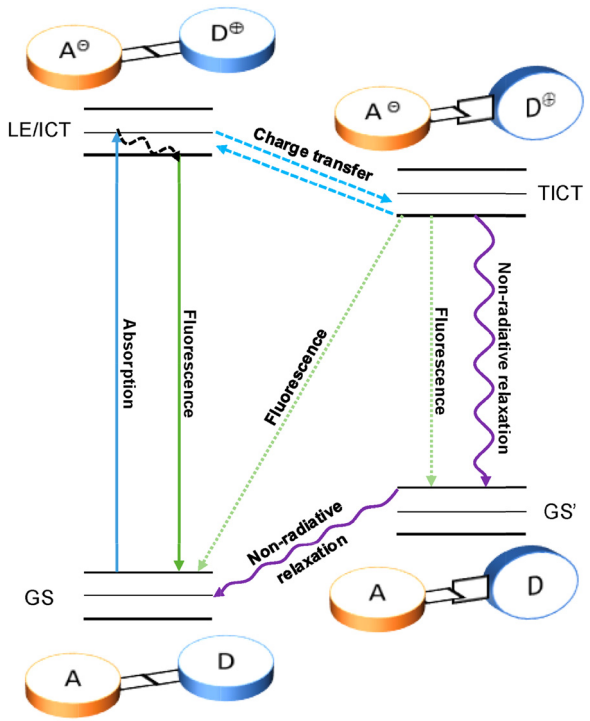

Fig. 2 Jablonski diagram of twisted Intramolecular charge transfer (TICT) dynamics.

1.3 Design of TICT-based fluorescent probes

In general, the most common approach for developing TICT-based fluorescent probes relies on two design strategies: fluorescence turn-on or fluorescence turn-off. Both these designs involve an electron donor, molecular rotors, linkers and an electron acceptor (Fig. 3). A turn-on probe will perform an intramolecular twisting motion in the excited state and switch on the TICT process, which results in the observation of low or no fluorescence signals. After exposure to a specific analyte, the molecular rotor will be blocked or removed to inhibit TICT and result in a strong fluorescence output. On the other hand, a turn-off probe adopts the opposite design approach. This probe will initially exhibit a temporary restriction of the molecular rotor. Then after the probe interacts with a target analyte or environmental condition, the rotor will be freed and the TICT process will be restored. This can lead to the changes of fluorescence signals from strong to weak. At the same time, this kind of design can also be used to exploit non-radiative relaxation for PTT treatment.

This review discusses recent advances in the development of fluorescent probes based on TICT. We focus on probes designed to detect important species in the environment or biological context. We discuss their main working mechanisms and limitations. In addition, we provide our own perspective on these probes. Finally, the current challenges and future opportunities for the development of TICT-based fluorescent probes are outlined.

2. TICT-based fluorescent probes for cations

2.1 Proton (H^+)

The proton (H^+) is one of the most important species in cells, and plays a key role in regulating cell homeostasis and metabolic pathways.[36,37] Normally, the pH value of mammalian cell organelles and compartments needs to be maintained in a range from 4.5 to 8.0.[38] pH imbalance can lead to cell dysfunction and may be associated with diseases such as Alzheimer's disease, renal failure and cancers.[39–43] Therefore, monitoring changes in pH can provide effective insights into the diagnosis of diseases and for monitoring the development of a disease state.

Yu *et al.* introduced a 1-piperidinyl group on to a 4-phenyloxy-1,8-naphthalimide skeleton to obtain a TICT-based fluorescent probe (**Napa-pp**). A (2-dimethylamino)ethyl sidechain was appended to the imide nitrogen to improve the water solubility of **Napa-pp**, which has a reported pK_a value of 5.32. The acidic environment of lysosomes, with a pH ranging from 5.0 to 6.0, can protonate the nitrogen atoms on the piperidinyl group and the (2-dimethylamino)ethyl group, thereby inhibiting

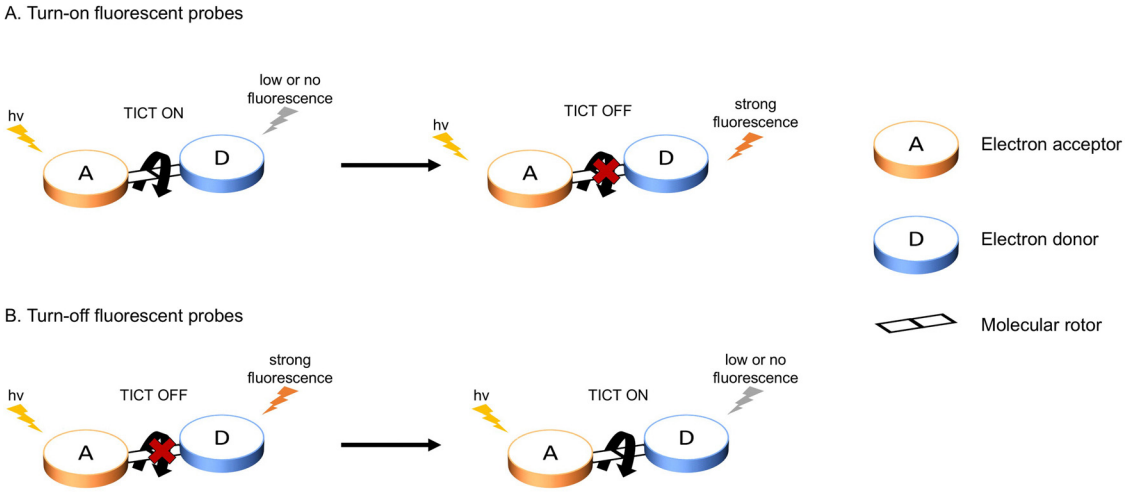

Fig. 3 Diagrammatic representation of the most common strategy underlying the design of turn-on (A) and turn-off (B) TICT-based fluorescent probes.

the TICT process and switching on the fluorescence of **Napa-pp**, enabling the visualization of lysosomes in living cells (Fig. 4).[44]

Doria *et al.* developed a pH-dependent red fluorescent probe (**NDI-5**) based on a water soluble naphthalenediimide. **NDI-5** was non fluorescent under neutral or basic conditions and remained blue in colour. However, acidic conditions can protonate **NDI-5** and switch on a strong red fluorescence emission due to the interruption of the TICT process. **NDI-5** was successfully used to monitor the inhibition of Vacuolar type H^+-ATPases (V-ATPases) by Bafilomycin A1 (BafA1) (Fig. 5). Significantly, V-ATPases were confirmed as the main mediators regulating pH in cancer cells and their upregulation has been observed in most human tumour cells.[45] Based on the fluorescence signals of **NDI-5**, the hypothesis of BafA1's endocytic sequestration within cancer cells and endosome/lysosome escape was confirmed. At the same time, these results also demonstrated that **NDI-5** is a permeable pH probe for cancer cells based on the turn on and off TICT processes.[46]

Zhu *et al.* designed a coumarin-based wide-range pH-responsive fluorescent probe (**L6**) including a benzimidazole group as a proton-responsive site (Fig. 6). When the pH value ranged from 4.5 to 8.5, **L6** produced a strong green emission at 497 nm under 371 nm excitation due to the ICT process. Under more acidic conditions (pH ranging from 1.0 to 3.0), a brilliant blue emission at 440 nm was observed when excited at 371 nm. However, under basic conditions (pH ranging from 10.5–13.5),

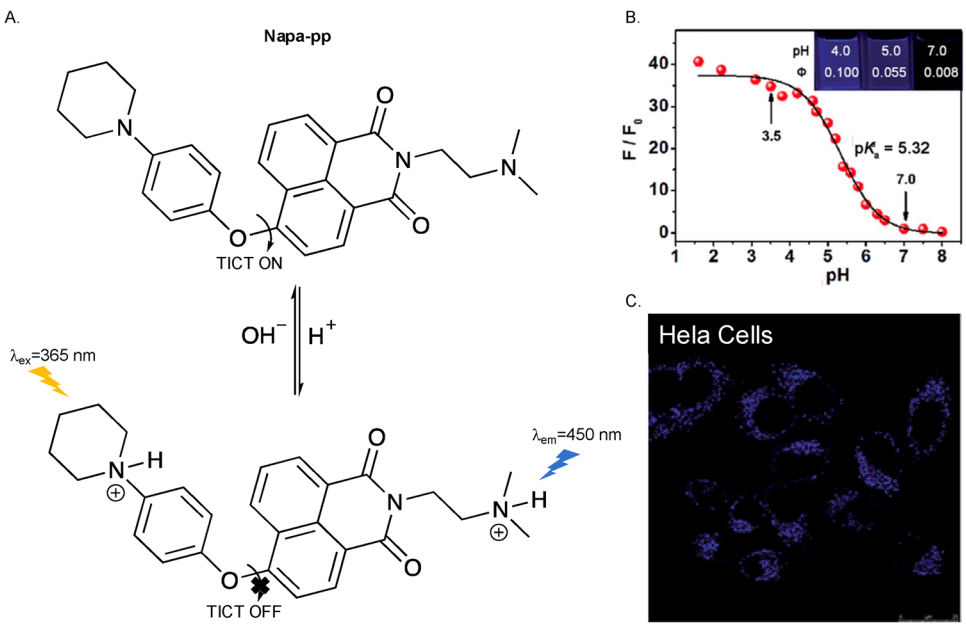

Fig. 4 (A) The proposed mechanism of **Napa-pp**. (B) The PL emission ratio changes of **Napa-pp** (4.5 μM) at 450 nm (F/F_0) with different pH values in DMSO–H_2O (1 : 250, v/v) buffer solution, λ_{ex} = 365 nm, P_0 is the PL intensity at pH = 7.0. (C) Confocal fluorescence images of living HeLa cells incubated with Napa-pp (4 μM) for 0.5 h. Image reproduced with permission from ref. 44. Copyright 2014, The Royal Society of Chemistry.

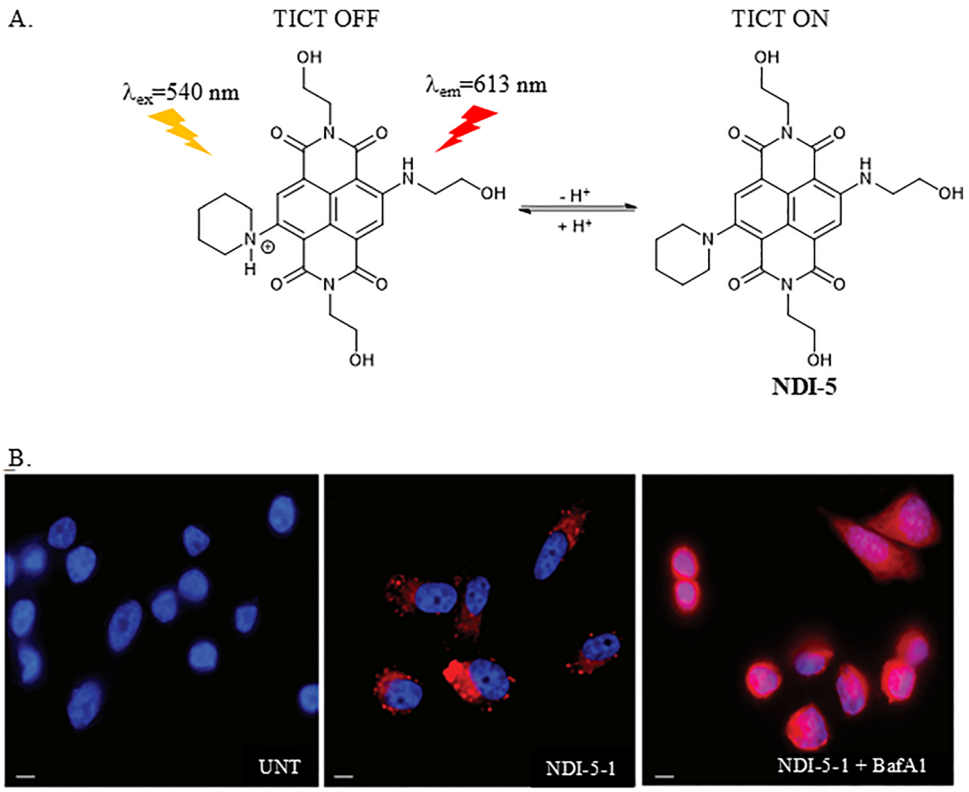

Fig. 5 (A) The proposed mechanism of **NDI-5**. **B**. Cell imaging studies of **NDI-5** in PC-3 cells. UNT: untreated cells. **NDI-5**: PC-3 cells incubated with 60 μmol L^{-1} **NDI-5** for 90 min. **NDI-5** + BafA1: PC-3 cells incubated with 60 μmol L^{-1} **NDI-5** for 90 min and treated with 50 nmol L^{-1} of BafA1 for 3 h. Scale bars: 10 μm. Image reproduced with permission from ref. 46. Copyright 2015, The Royal Society of Chemistry.

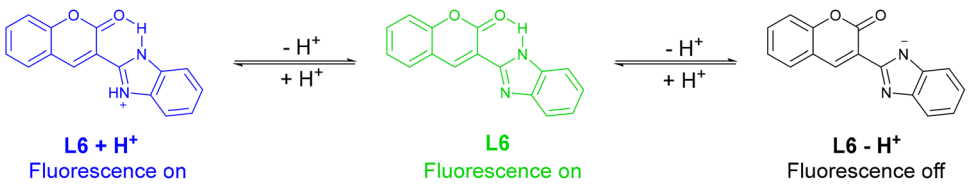

Fig. 6 The proposed mechanism of **L6**.

the fluorescence of **L6** was quenched and a red shift of the maximum absorption wavelength in the UV-VIS spectrum was observed because deprotonation promoted the TICT process. Besides, the reversibility of **L6** fluorescence was demonstrated by the alternating addition of tetra-*N*-butyl ammonium hydroxide (TBAOH) and $HClO_4$. Significantly, during the switching process, there was almost no loss in fluorescence efficiency. Due to the low solubility of **L6**, the probe response was evaluated in a DMSO/H_2O (1 : 9, v/v) HEPES buffered solution.[47]

2.2 Copper (Cu^{2+})

As an indispensable trace element, copper plays an essential role in aerobic organisms.[48] Its redox activity makes copper a catalytic and structural cofactor for enzymes involved in an array of biochemical processes.[48] Adequate copper levels sustain the growth, proliferation and development of both humans and human pathogens.[48] However, defects in copper homeostasis and copper ion overload can lead to a series of genetic diseases and neurodegenerative disorders, such as Menkes disease, Wilson's disease, Alzheimer's disease, Parkinson's disease and prion disease.[49–52] This makes it necessary to develop fluorescent probes for copper detection in the environment and for copper imaging in biological contexts.

Zong *et al.* designed a turn-on TICT fluorescent probe (**NDI-4**) based on a core substituted naphthalenediimide linked with to 1,4,7,10-tetrathia-13-azacyclopentadecane group as the Cu^{2+} responsive site (Fig. 7). Due to the TICT effect, **NDI-4** was nearly non fluorescent even though there was strong ICT effect between the alkyamino electron donor and the naphthalene diimide electron acceptor. After the nitrogen and four sulfur atoms on the 1,4,7,10-tetrathia-13-azacyclopentadecane group coordinated with Cu^{2+}, **NDI-4** emitted a strong red fluorescence at 638 nm because of the inhibition of the TICT process. **NDI-4** exhibited high sensitivity with a detection limit of 4 μM and excellent selectivity towards Cu^{2+}.[53]

García *et al.* developed a TICT turn-off fluorescent probe (**6b**) based on a 1,7-dipyridyl-bis(pyrazolo)pyridine (PBP) (Fig. 8).

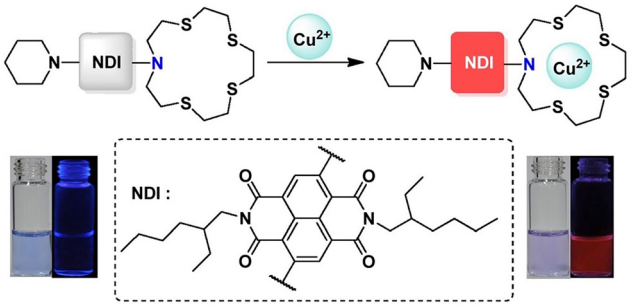

Fig. 7 The proposed mechanism of **NDI-4** towards Cu^{2+}. Image reproduced with permission from ref. 53. Copyright 2016, Elsevier.

This tridentate ligand contained a fused tricyclic structure with two alkyl and three aryl substituents, as well as three pyridyl nitrogen atoms as suitable motifs to ligate Cu^{2+}. The probe exhibited strong blue fluorescence and a large Stokes shift, which is one of the advantages of the TICT mechanism. When Cu^{2+} formed a complex with **6b**, the structure became more rigid and ligand-metal charge transfer became the dominant process due to the tridentate binding mode. This resulted in fluorescence quenching through inhibition of the TICT process. Additionally, the binding between **6b** and Cu^{2+} was shown to be reversible. Ethylenediamine has a high affinity for Cu^{2+} and it was demonstrated that **6b-Cu^{2+}** can release **6b** with recovery of fluorescence upon the addition of ethylenediamine.[54]

Rai *et al.* developed a ratiometric turn-on activity-based fluorescent probe (**APDA**) based on TICT/ICT. The probe consisted of a polycyclic aromatic core with a diaminomaleonitrile (**DAMN**) as the response site for Cu^{2+} (Fig. 9). **APDA** was observed as a reddish-brown solution by the naked eye under UV light at 365 nm. At the same time, due to the TICT mechanism, there are a strong emission at 563 nm and a weak emission at 418 nm in the fluorescence emission spectrum under excitation at 387 nm. The addition of Cu^{2+} resulted in hydrolysis of the imine bond and release of an aldehyde derivative with a strong blue emission at 418 nm when excited at 387 nm, due to interruption of the TICT process. Furthermore, **APDA** was used to image Cu^{2+} in live human breast cancer cells. Since TICT-based **APDA** exhibits dual emission, two channels were used to observe the fluorescence changes of **APDA** in the presence or absence of Cu^{2+}. There was an obvious fluorescence change in the blue channel while insignificant fluorescence was observed in the green channel. In addition to Cu^{2+}, **APDA** also exhibited a similar response to hypochlorite anion (ClO^-).[28]

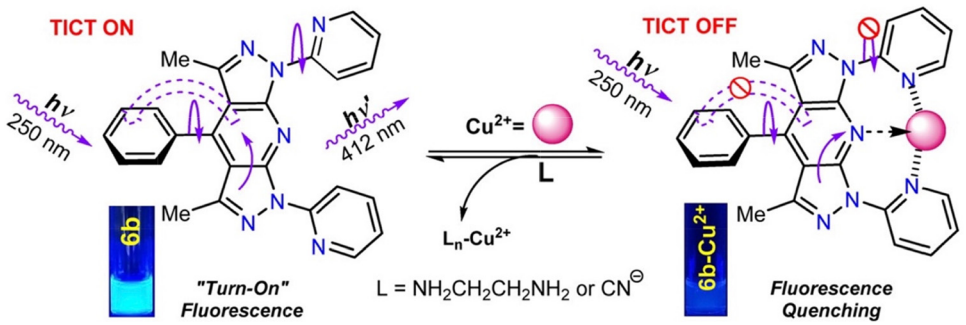

Fig. 8 The proposed reversible working mechanism of **6b** with Cu^{2+}. Image reproduced with permission from ref. 54. Copyright 2019, American Chemical Society.

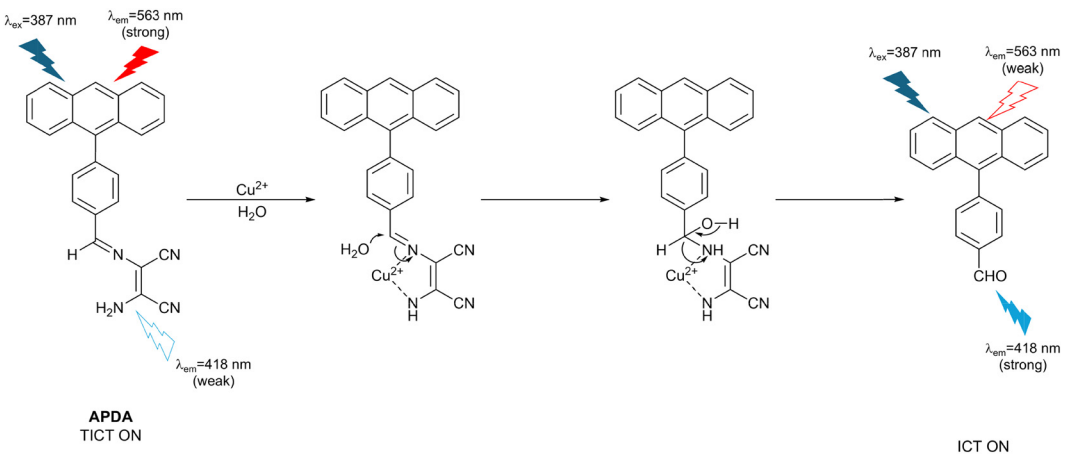

Fig. 9 The proposed mechanism of **APDA** with Cu^{2+}.

2.3 Iron (Fe^{2+} and Fe^{3+})

Iron is the most abundant transition metal in the human body and participates in various biological events based on its redox activity.[55–57] Normally, biological iron exists in the form of Fe^{2+} and Fe^{3+}.[58] However, iron overload can result in the excessive production of reactive oxygen species (ROS), which then causes severe cell damage and organ dysfunction.[59,60] At the same time, the disruption of iron homeostasis is associated with various diseases such as cancer, neurodegenerative disorders and hepatitis.[61–63] So, it is highly desirable to develop fluorescent probes to detect and image iron in biological systems.

Hirayama *et al.* developed an activity-based switch-on fluorescent probe (**RhoNox-1**) for Fe^{2+} detection and imaging (Fig. 10), based on a rhodamine fluorophore. The tertiary amine *N*-oxide group in **RhoNox-1** is not conjugated with the π-system of the fluorophore, as it lacks a lone pair. This led to a blue shift in the absorption spectrum of **RhoNox-1** compared to the parent fluorophore, rhodamine B. The presence of the *N*-oxide group also resulted in only weak emission from **RhoNox-1** due to TICT. Fe^{2+} can mediate the reductive deoxygenation of the *N*-oxide group, unmasking a tertiary amine group and thereby resulting in a strong and selective fluorescence response. **RhoNox-1** was also used to image basal and endogenous labile Fe^{2+} in living HepG2 cells. However, **RhoNox-1** exhibited pH dependence within a physiological pH range.[64]

Lamoria *et al.* designed a series of fluorescent and colorimetric turn-off probes (**3a–b** and **5a–b**) based on benzimidazolium or bis(benzimidazolium) motifs as electron acceptors with oxazolines as response sites and electron donors (Fig. 11). Due to the perpendicular arrangement of oxazoline and benzimidazolium, the TICT phenomenon occurred and led to large Stokes shifts of **3a–b** and **5a–b** with emissions at about 367 nm in water. Upon the addition of Fe^{3+}, **3a–b** and **5a–b** can form a complex, which resulted in the fluorescence quenching of **3a–b** and **5a–b**. These probes were used to detect Fe^{3+} fluorocolorimetrically in real water samples.[65]

2.4 Mercury (Hg^{2+})

Mercury ions (Hg^{2+}) and organomercury species are a significant public health concern, as they are extremely harmful to humans and other organisms.[66] Methylmercury produced by microbial biomethylation of Hg^{2+} is bioaccumulative in the environment and can target the central nervous system, causing brain damage and neurodegenerative diseases if ingested.[67–69] Hence, it is important to develop fluorescent probes for monitoring mercury in the environment to avoid disasters like the Minamata tragedy.[70,71]

Tharmaraj *et al.* designed a turn-off colorimetric and fluorescent probe (**1**) with a dansyl core linked with a sulfonamide–thiophenol motif as the binding site for Hg^{2+} (Fig. 12). Upon the addition of Hg^{2+}, N,S-chelation occurred. TD-DFT calculations indicated separated charge distributions between the HOMO and LUMO of the complex of Probe **1** and Hg^{2+}. Specifically, the HOMO was localised on the *N*,*N*′-dimethylaminonaphthyl group whereas the LUMO was primarily localised on the thiophenol ring and sulfonamide group. Thus, when excited, electron transfer from the *N*,*N*′-dimethylaminonaphthyl donor to the sulfonamide–thiophenol acceptor occurred. Given the TICT process was switched on, the fluorescence of **1** was quenched upon Hg^{2+}

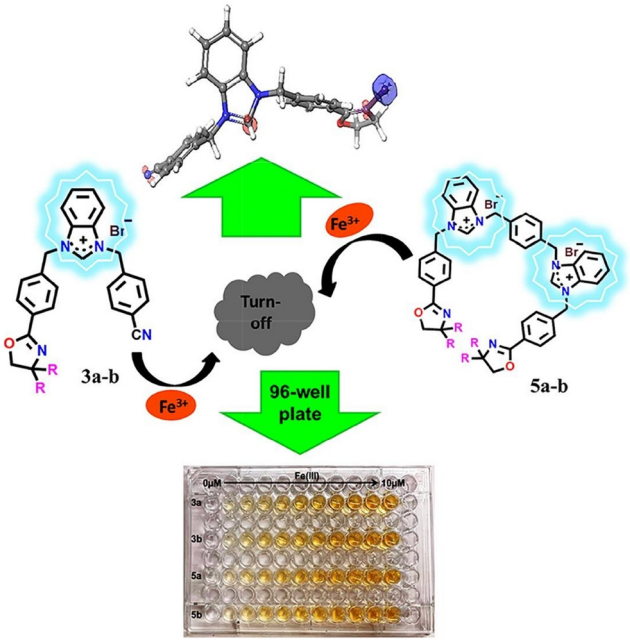

Fig. 11 The proposed mechanism of **3a–b** and **5a–b** with Fe^{3+} (R = H, CH_3). Image adapted with permission from ref. 65. Copyright 2024, Elsevier.

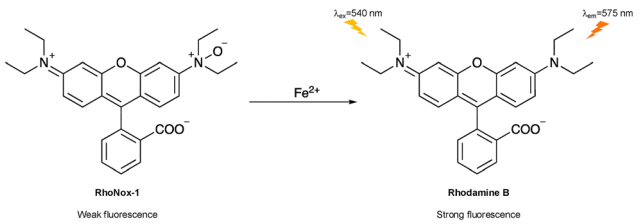

Fig. 10 The proposed mechanism of **RhoNox-1** with Fe^{2+}.

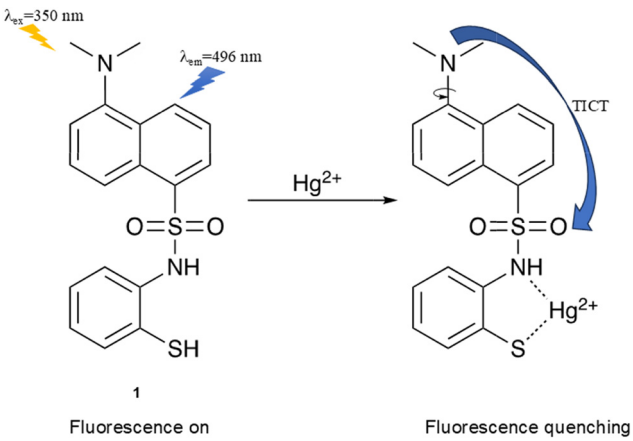

Fig. 12 The proposed mechanism of **1** with Hg^{2+}.

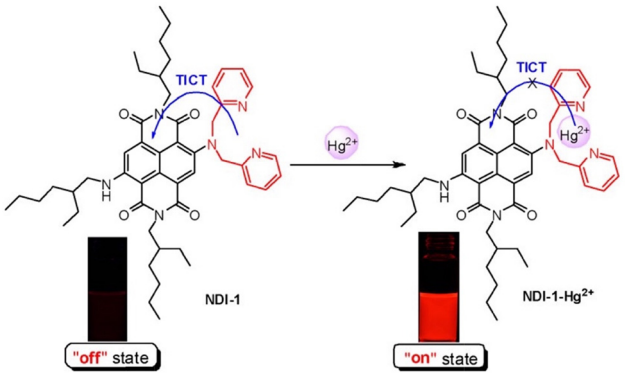

Fig. 13 The proposed working mechanism of **NDI-1** with Hg^{2+}. Image reproduced with permission from ref. 73. Copyright 2012, American Chemical Society.

complexation. The probe was used to detect Hg^{2+} in real water samples with excellent selectivity over other metal ions.[72]

Li *et al.* selected a naphthalenediimide as a reporter motif connected to a di-2-picolylamine as a receptor motif for Hg^{2+} to obtain a near-infrared (NIR) fluorescent probe (**NDI-1**) (Fig. 13). An alkylamine was appended to the NDI core as a strong electron donor to extend the push–pull system, to tune the emission to the NIR region. Due to the TICT mechanism, **NDI-1** was nearly non fluorescent. However, after Hg^{2+} complexed with the di-2-picolylamine group, the electron donating ability of the di-2-picolylamine group was attenuated. At the same time, the dihedral angle between the naphthalenedimide core and the di-2-picolylamine group increased, which inhibited the TICT process and resulted in strong red-to-NIR emission. The probe was successfully used to image Hg^{2+} in live HeLa cells.[73]

Zhang *et al.* developed a TICT-based fluorescent probe (**L-1**) with both colorimetric and fluorescence channels for Hg^{2+} detection (Fig. 14). The probe consisted of two naphthalene Schiff bases as reporter motifs and a combination of hydroxyl and imine groups as the coordinating groups. The TICT process resulted in an "off" state of fluorescence for **L-1**. However, when Hg^{2+} coordinated with the hydroxyl and imine groups of **L-1**, Zhang *et al.* propose that the relative orientation of the two naphthalene groups was altered. This led to reduced electron transfer and contributed to the formation of the coplanar conjugated system. As such the inhibition of the TICT process and promotion of the ICT process resulted in the appearance of a strong blue fluorescence and a colour change of the solution from yellow to nearly clear.[74]

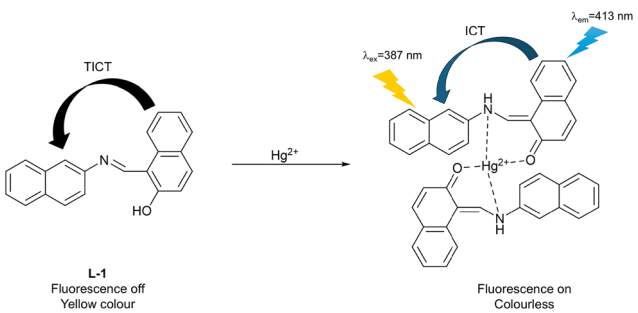

Fig. 14 The proposed working mechanism of **L-1** with Hg^{2+}.

Jha *et al.* developed a pyrano[3,2-*c*]julolidine-2-one-based ratiometric fluorescent probe (**PYJO4**) to coat test strips to detect Hg^{2+} in aqueous solution and image Hg^{2+} in living cancer cells (Fig. 15). The probe exhibited an emission at 530 nm due to the LE state and another stronger emission at 665 nm due to the TICT state. After Hg^{2+} bound with the dipicolylamine receptor, the conformation reportedly changed from the twisted state to a planar state and inhibition of the TICT process resulted in an enhanced fluorescence emission at 530 nm and a decreased fluorescence emission at 665 nm. Meanwhile, detection by **PYJO4** was reversible, through the addition of potassium iodide (KI) solution. Since I^- has a high affinity for Hg^{2+}, forming $[HgI_4]^{2-}$, the coordination of **PYJO4** with Hg^{2+} is reversed when KI was added. Over a pH range from 5 to 9, the probe response was pH-independent. Moreover, **PYJO4** coated test strips could be used to detect concentrations as low as 200 ppb Hg^{2+}, which implies great potential for monitoring Hg^{2+} in aqueous environmental samples.[75]

Zong *et al.* designed a switch-on fluorescent probe (**NDI-5-2**) based on a naphthalenediimide fluorophore with a bis(2-(3,5-dimethylpyrazol-1-yl)ethyl)amine binding site for Hg^{2+} (Fig. 16). The TICT process resulted in weak fluorescence emission of **NDI-5-2**. However, on the addition of Hg^{2+}, a complex between **NDI-5-2** and Hg^{2+} was formed, and the fluorescence quantum yield increased from 0.28% to 8.83%. In addition to a strong red emission at 651 nm, the probe also exhibited excellent sensitivity, with a limit of detection of 1.3 μmol L^{-1}. In addition, the

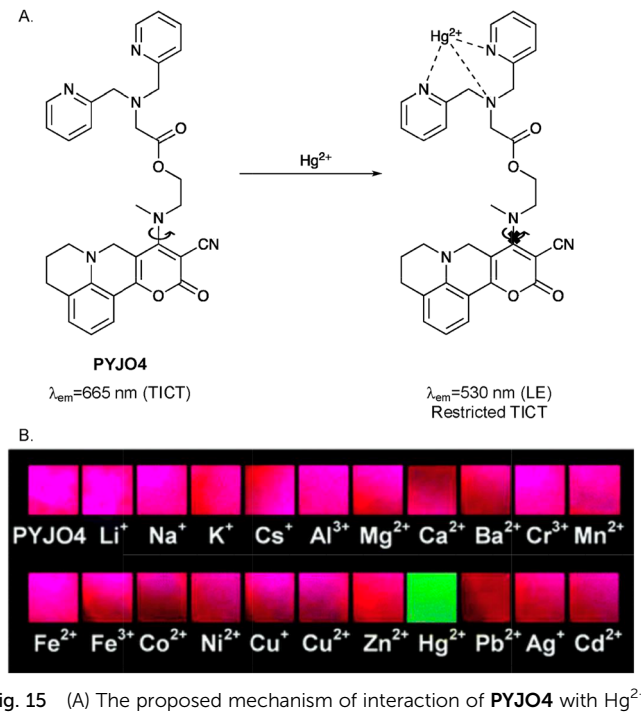

Fig. 15 (A) The proposed mechanism of interaction of **PYJO4** with Hg^{2+}. (B) **PYJO4** coated test strips with different metal ions under a UV lamp with the excitation wavelength of 365 nm. Image reproduced with permission from ref. 75. Copyright 2016, The Royal Society of Chemistry.

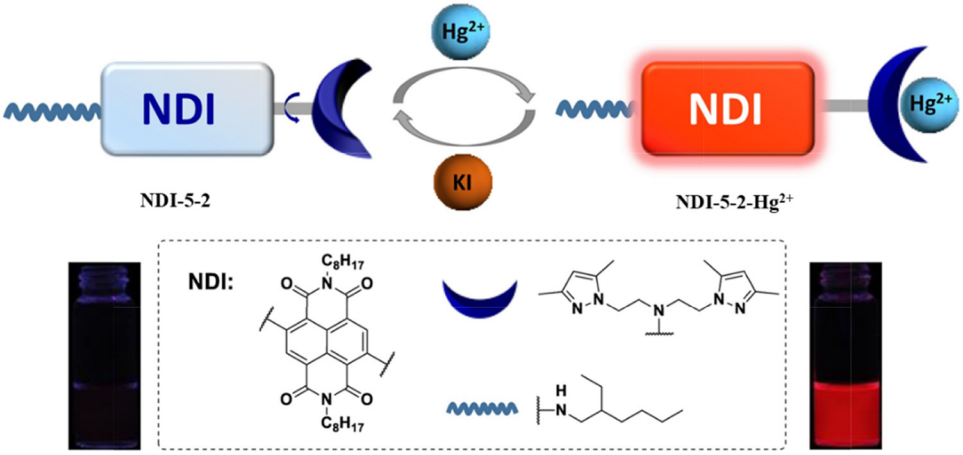

Fig. 16 The proposed mechanism of **NDI-5-2** with Hg^{2+}. Image reproduced with permission from ref. 76. Copyright 2017, Elsevier.

reversibility of **NDI-5-2** coated test strips was confirmed by adding KI. Since I^- has a high affinity for Hg^{2+}, forming $[HgI_4]^{2-}$, the coordination of **NDI-5-2** with Hg^{2+} is reversed when KI was added. In living MCF-7 cells, **NDI-5-2** exhibited good cell permeability for the imaging of Hg^{2+}.[76]

2.5 Zinc (Zn^{2+})

Zinc is an indispensable micronutrient for humans, is a cofactor of numerous enzymes and is involved in various biological processes.[77,78] However, excess free zinc in the human body is closely associated with a number of diseases such as Alzheimer's disease, brain injury, diabetes and epilepsy.[77–80] In addition, in the environment, zinc pollution can also lead to problems, such as decreased soil microbial activity and land degradation.[81] Hence, it is necessary to develop fluorescent probes to detect and monitor Zn^{2+} levels *in vivo* or in the environment.

Zheng *et al.* developed a fluorescent probe (**HL^1**) based on two Schiff bases for Zn^{2+} detection (Fig. 17). Upon the addition of Zn^{2+}, the two nitrogen atoms and the hydroxyl oxygen formed a tridentate complex. The pyridine ring and the phenyl ring of the **HL^1-Zn^{2+}** complex were nearly orthogonal, as shown by X-ray crystallography. The presence of the ethoxy group as an electron donor induced TICT, with this zinc complex exhibiting an emission maximum at 493 nm. However, due to the similar electronic configurations of Zn^{2+} and Cd^{2+}, **HL^1** can also respond to Cd^{2+} although in this case emission is from the LE state. Notably, the X-ray structure of the **HL^1-Cd^{2+}** complex shows the pyridine and phenyl rings to be near coplanar in the solid state. When excited at 350 nm in ethanol, the fluorescence emission of **HL^1** changes from 463 nm to 493 nm upon the addition of Zn^{2+}. With higher concentrations of Zn^{2+}, the fluorescence intensity at 493 nm increased linearly. The limit of detection for Zn^{2+} was 1.11 μM. By comparison, the addition of Cd^{2+}, **HL^1** gave fluorescence with an emission maximum at 463 nm (*i.e.* no red-shift due to TICT) and the limit of detection for Cd^{2+} was 9.2 μM.[82]

2.6 Magnesium (Mg^{2+})

Magnesium is the second most abundant ion in cells, which plays a vital role in metabolic pathways, genomic stability and DNA processing.[83,84] Bodily levels of magnesium have a close relationship with cardiovascular diseases, accelerated aging and tumours.[84] Therefore, it is desirable to explore the development of fluorescent probes for Mg^{2+} detection.

Liu *et al.* selected a biarylpyridine as the fluorophore and a crown ether group as the response site to obtain an ON–OFF–ON fluorescent probe 2 triggered by protons for Mg^{2+} detection (Fig. 18). When excited at 312 nm, the probe had a fluorescence response at 399 nm. If alkali or alkaline earth cations were

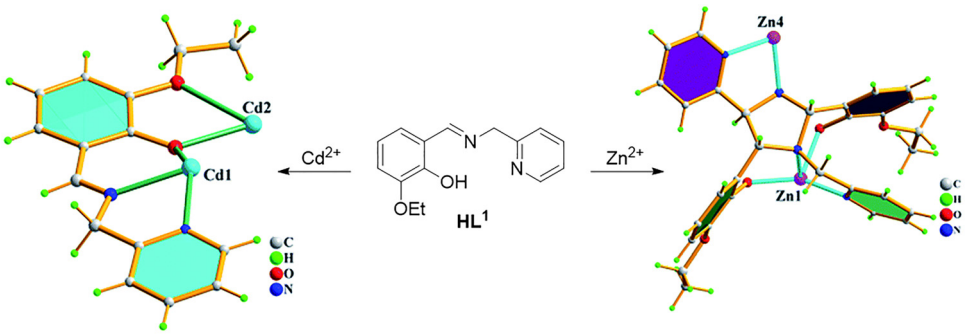

Fig. 17 The proposed mechanism of interaction of **HL^1** with Zn^{2+} and Cd^{2+}. Image adapted from ref. 82. Copyright 2015, The Royal Society of Chemistry.

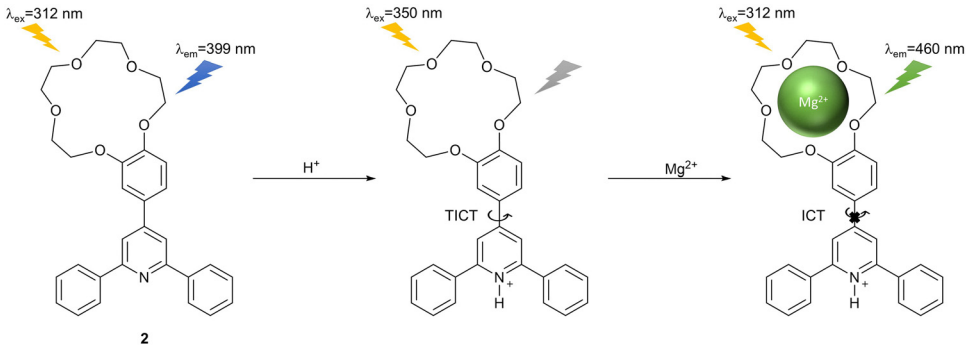

Fig. 18 The proposed working mechanism of **2** with H^+ and Mg^{2+}.

added directly, a blue shift of the probe's emission and decrease in fluorescence intensity was observed, coupled with reduced selectivity towards Mg^{2+}. However, upon the addition of Brønsted acid, the fluorescence emission of the probe at 399 nm was quenched due to activation of the TICT process. After subsequent coordination of Mg^{2+} with the crown ether group of the probe, the TICT process was inhibited, and the ICT process was activated. The complex exhibited a strong fluorescence emission at 460 nm and excellent selectivity towards Mg^{2+} over other alkali and alkaline earth cations.[85]

3. TICT-based fluorescent probes for anions

3.1 Acetate (AcO^-)

Acetate (AcO^-) has an essential role in various metabolic functions, such as energy production and macromolecule biosynthesis.[86] At the same time, AcO^- can promote the survival of cancer cells under hypoxic stress as an epigenetic metabolite.[87] However, the mechanism of how AcO^- participates in biological processes remains unclear.[86] Hence, it is necessary to develop fluorescent probes for monitoring AcO^- and exploring its (patho)physiological functions.

Lin *et al.* developed a reversible fluorescent probe (**LX**) based on a naphthalene and quinoline fluorophore for AcO^- detection (Fig. 19). The unbound state of the probe exhibited TICT and resulted in an "off" state of fluorescence. However, Lin *et al.* propose that after AcO^- interacted with the hydroxyl and imine groups of **LX** through hydrogen bonding, the imine C–C bond rotation was inhibited. So, the TICT process was switched to an ICT process with the observation of a strong fluorescence signal with an emission maximum at 520 nm when excited at 435 nm in DMSO solution. The addition of H^+ can disrupt the hydrogen bonds between AcO^- and **LX**, which recovered the TICT state and reduced the fluorescence, demonstrating reversibility. The probe exhibited excellent sensitivity towards AcO^- with a detection limit of 0.4 μM.[88]

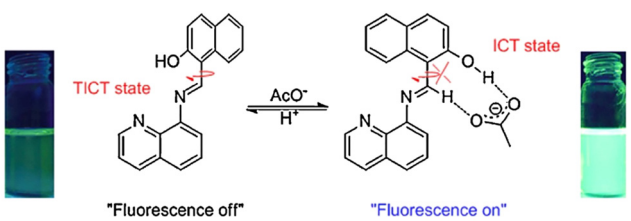

Fig. 19 The proposed mechanism of interaction of **LX** with AcO^-. Image reproduced with permission from ref. 88. Copyright 2014, Elsevier.

3.2 Cyanide (CN^-)

Cyanide salts exhibit acute toxicity in humans, by blocking the mitochondrial electron transport chain through inhibition of cytochrome *c* oxidase, interfering with aerobic respiration and leading rapidly to death.[89,90] However, cyanide has extensive applications in various industrial fields, such as plastics manufacturing, mining and electroplating.[90] The discharge of the related wastewater carries the risk of causing environmental pollution problems and drinking water contamination. Therefore, it is desirable to explore fluorescent probes for cyanide (CN^-) detection.

Chen *et al.* selected a 9-anthryl fluorophore and a dicyanovinyl group as the response site for CN^- to synthesize a series of activity-based turn-on fluorescent probes (**C1–C3**) (Fig. 20). Due to steric crowding, the dicyanovinyl group was twisted and the fluorescence of **C1–C3** was quenched due to the TICT process. However, the addition of CN^- resulted in the formation of adducts by conjugate addition to the dicyanovinyl motif. In these adducts, the TICT process was suppressed, which favoured emission from the LE state. For **C3**, the fluorescence was enhanced by about 242-fold upon the addition of CN^-. At the same time, **C3** exhibited excellent sensitivity towards CN^- with a detection limit of 1.14 μM, which is below the safe CN^- level for drinking water set by the WHO. Chen *et al.* also exchanged the 9-anthryl fluorophore for a porphyrin group, another kind of π-conjugated skeleton, to produce probe **C5**. Porphyrin **C5** exhibited weak fluorescence similar to **C1–C3**. Upon the addition of CN^-, the fluorescence emission was once again enhanced. The introduction of different electron donors and different π-conjugated skeletons was shown to modulate the emission wavelengths of the probe-cyanide adducts from blue to red.[91]

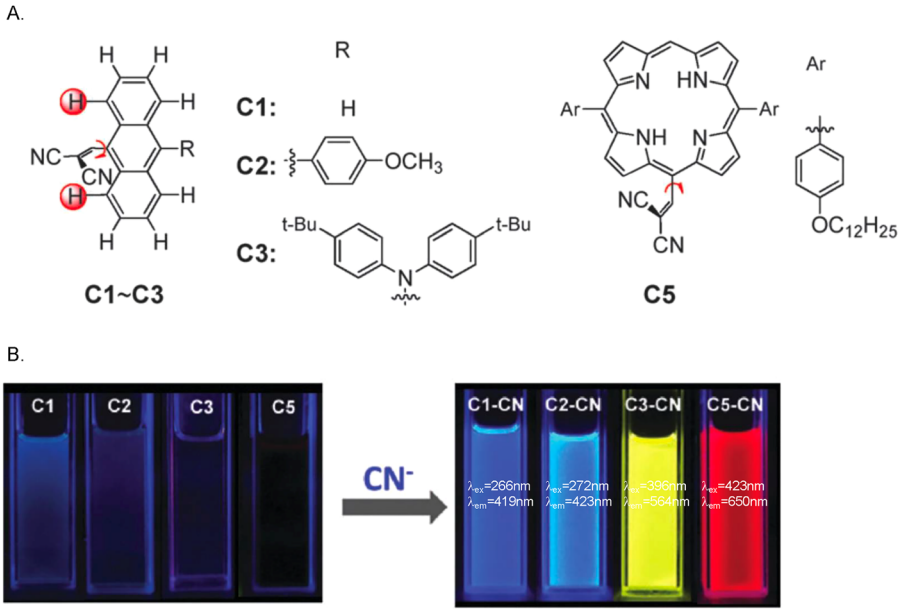

Fig. 20 (A) The chemical structures of **C1**, **C2**, **C3** and **C5**. (B) The fluorescence changes of 40 μM **C1**, **C2**, **C3** and **C5** in CH_2Cl_2 upon the addition of 3 equiv. of CN^- under a UV lamp. Image reproduced with permission from ref. 91. Copyright 2013, The Royal Society of Chemistry.

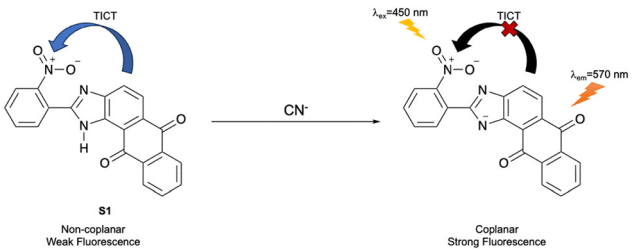

Fig. 21 The proposed working mechanism of **S1** with CN^-.

Balamurugan *et al.* developed a ratiometric turn-on fluorescent probe (**S1**) based on an imidazoanthraquinone for detecting CN^- (Fig. 21). The nitro group in the *o*-position and the N–H of the imidazole moiety hindered the adoption of a coplanar conformation around the biaryl bond. Thus, the TICT process was operative, with donation from the electron rich imidazoanthraquinone moiety to the electron poor nitrophenyl group, resulting in only weak fluorescence emission at 554 nm for **S1**. The addition of CN^- can deprotonate the imidazole N–H of **S1** to give the corresponding anion that can achieve coplanarity, and which has enhanced electron density for the imidazoanthraquinone moiety, resulting in inhibition of the TICT process and a red shift in the fluorescence, with strong emission at 570 nm being observed. **S1** exhibited excellent sensitivity and selectivity towards CN^- when used with real waste samples. Additionally, the probe also exhibited good cell permeability for imaging CN^- in living RAW264.7 cells.[92]

Pegu and Das developed two self-assembled nano fluorescent probes (**Benz-d-CF_3** and **Benz-m-CF_3**) for CN^- detection in conjunction with cetyltrimethylammonium bromide (CTAB) (Fig. 22). These probes consisted of quinazoline-fused benzimidazole skeletons with two different phenyl substituents to impart donor–acceptor characteristics. The C–N single bond of the phenyl substituents reportedly can twist and hence these probes exhibit TICT properties. In aqueous solutions containing CTAB, the two probes dispersed readily in water. Hydrogen bonding interaction and π–π interaction helped to self-assemble the nano aggregates. At the same time, the TICT process resulted in an almost complete quenching of the fluorescence of the probes.

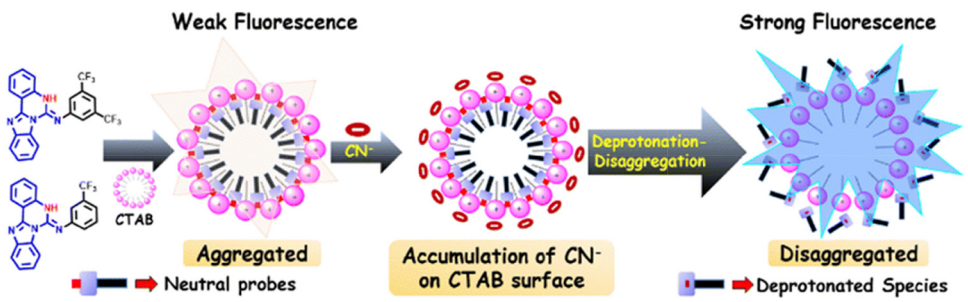

Fig. 22 The proposed mechanism of action of **Benz-d-CF_3** and **Benz-m-CF_3** with CN^-. Image reproduced with permission from ref. 93. Copyright 2024, The Royal Society of Chemistry.

Upon the addition of CN^-, disaggregation of the nano aggregates reportedly occurs. The authors state that co-planarity is therefore achieved leading to an enhancement of the ICT process and an enhanced fluorescence emission at 460 nm for **Benz-d-CF$_3$** and 485 nm for **Benz-m-CF$_3$** when excited at 365 nm. Besides, the detection of CN^- when using **Benz-d-CF$_3$** and **Benz-m-CF$_3$** was shown to be reversible upon addition of Cu^{2+}. When **Benz-m-CF$_3$** was used for the analysis of drinking water samples, excellent selectivity and sensitivity towards CN^- with a detect limit of 496.5 nM was observed.[93]

3.3 Hypochlorous acid (HClO)

Hypochlorous acid (HClO) is an important ROS in biological systems, and is generated based on the reaction between hydrogen peroxide (H_2O_2) and chloride ions catalysed by myeloperoxidase (MPO) in neutrophils.[94,95] HClO is essential in the immune defence system, however, excess levels of HClO can lead to cell apoptosis and oxidative stress.[96–98] This is closely associated with tissue damage and various diseases, such as Parkinson's disease, Alzheimer's disease, atherosclerosis, acute liver injury and cancers.[99–101] As such, the development of fluorescent probes for monitoring and imaging HClO in a biological context is desirable for understanding its role in related diseases and advancing relevant therapeutic and diagnostic strategies.

Lou *et al.* developed a reversible fluorescent probe (**NI-Se**) for HClO detection *in vivo*. The probe consisted of a 1,8-naphthalimide fluorophore and a selenide as the response site towards HClO (Fig. 23). The oxidation–reduction cycles between the selenium group with ROS and glutathione (GSH) facilitated reversible detection. The Se···N nonbonding interaction was enhanced in the excited state, which contributed to the intramolecular twisting. The on state of the TICT process quenched the fluorescence of **NI-Se**. However, upon the addition of HClO, the oxidation of the selenide to the corresponding selenoxide inhibited the Se···N nonbonding interactions as well as the TICT process, leading to the recovery of fluorescence emission. The detection process was shown to be reversible by addition of thiols or H_2S. In addition, **NI-Se** exhibited low cytotoxicity when used to image HClO in living RAW264.7 cells, and was used for the visualization of HClO and the repair by antioxidants in an LPS (lipopolysaccharide) mouse model.[102,103]

Mu *et al.* designed a mitochondrial-targeted fluorescent probe (**Mito-QL**) for detecting HClO with a large Stokes shift of 203 nm (Fig. 24). The probe was non-fluorescent due to the TICT effect between the dimethylaniline group and the quinolinium moiety. The addition of HClO resulted in the hydrolysis of the *N*,*N*-dimethylthiocarbamate moiety and revealed the fluorophore with strong red fluorescence emission at 590 nm when excited at 387 nm due to the ICT process. **Mito-QL** was demonstrated to have mitochondrial targeting ability and was able to image exogenous and endogenous HClO in the mitochondria of living cells. The positive charge on the nitrogen results in a mitochondrial targeting group between the fluorophore and response site to HClO, and avoided off target fluorescence interference. It was also shown that **Mito-QL** could be used to monitor HOCl during ferroptosis caused by ROS-induced lipid peroxidation.[104]

Shao *et al.* used a benzohemicyanine fluorophore with a thiomorpholine receptor to construct an activity-based fluorescent probe (**BCy-S**) for HClO detection (Fig. 25). The thiomorpholine

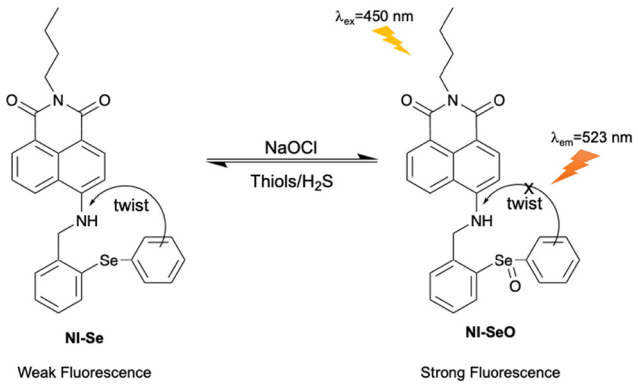

Fig. 23 The reversible working mechanism of **NI-Se**.

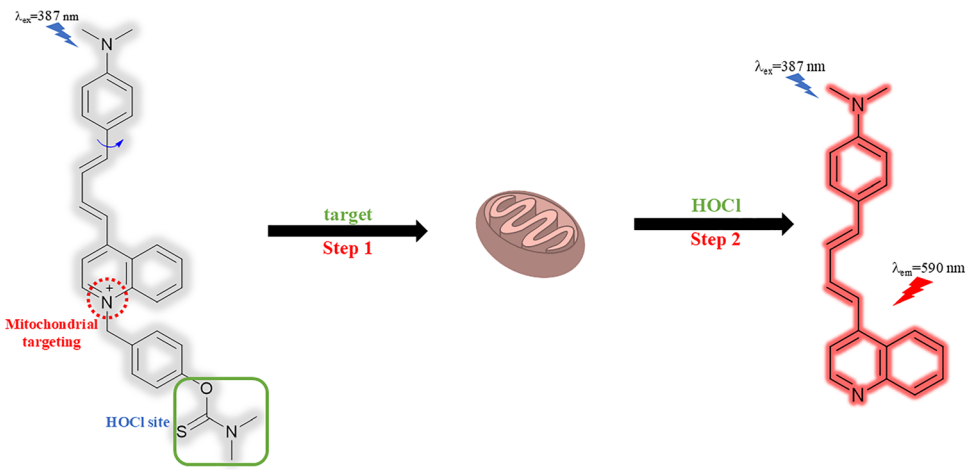

Fig. 24 The proposed mechanism of **Mito-QL** with HClO.

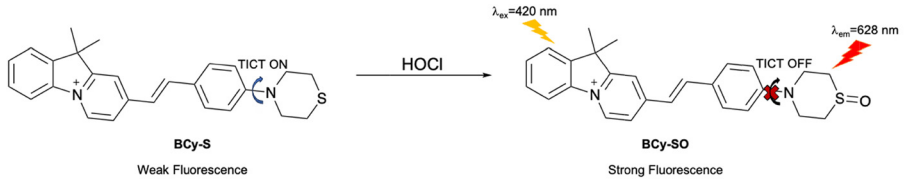

Fig. 25 The proposed mechanism of action of **BCy-S** with HClO.

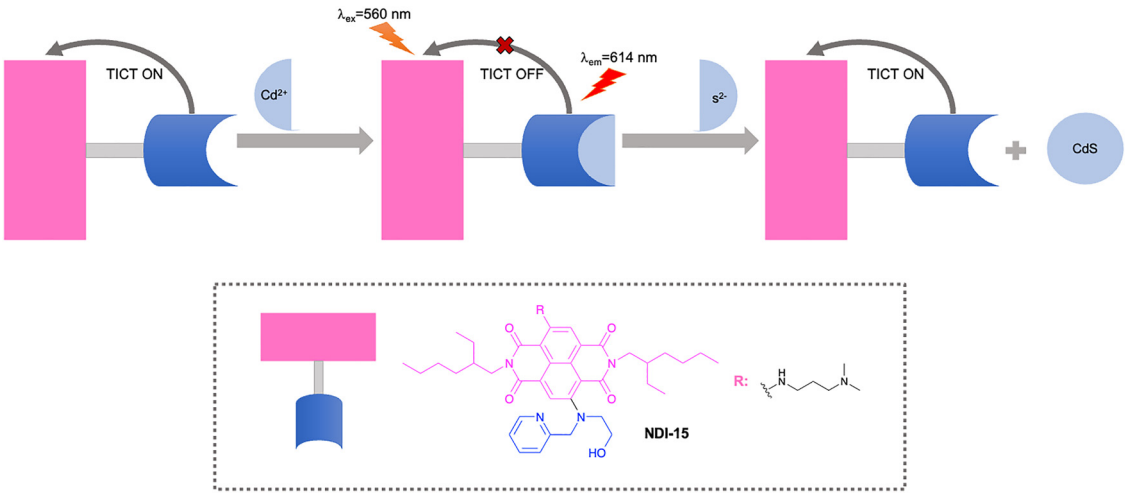

Fig. 26 The proposed mechanism of action of **NDI-15** based on a displacement strategy.

group of the probe exhibited TICT upon excitation, leading to the weak fluorescence of **BCy-S**. Upon the addition of HClO, oxidiation at sulfur resulted in the generation of the sulfoxide. This introduction of an electron-withdrawing motif to the amino auxochrome suppressed the TICT process, leading to a strong red fluorescence emission at 628 nm upon excitation at 420 nm. **BCy-S** exhibited pH independence, a large Stokes shift, high sensitivity (35.2 nM limit of detection) and excellent selectivity. In addition, **BCy-S** was used to visualize HClO in living HeLa cells and zebrafish, supporting the photostability and biocompatibility of the probe.[105]

3.4 Sulfide (S^{2-})

Depending on different pH values, sulfide may exist in three protonation states: S^{2-}, HS^- and H_2S. When the pH is below 7, H_2S predominates. When the pH varies from approximately 7 to approximately 12, HS^- is the major species; under more basic conditions, dianionic S^{2-} is the major species[106] Sulfide is a potentially toxic anion, which can irritate mucous membranes and with continuous exposure to high concentrations can lead to respiratory paralysis.[107–109] As such, it is important to develop fluorescent probes for sulfide detection.

Zong *et al.* developed a reversible fluorescent probe (**NDI-15**) with a naphthalenediimide fluorophore as electron acceptor and a 2-((pyridine-2-ylmethyl)amino)ethanol receptor as electron donor for detecting S^{2-} (Fig. 26). The perpendicular orientation of the fluorophore and the receptor in the excited state promoted the TICT process, which led to no fluorescence emission of NDI-15. Cd^{2+} can coordinate with the probe to form **NDI-15-Cd^{2+}**, which effectively inhibited the TICT effect and recovered the strong fluorescence emission. Upon the addition of S^{2-}, Cd^{2+} can be removed by S^{2-} from the 2-((pyridine-2-ylmethyl)amino)ethanol moiety of **NDI-15-Cd^{2+}** in order to release **NDI-15**, through the formation of the sparingly soluble CdS. This in turn results in a fluorescence decrease due to the recovery of the TICT process. Based on this displacement mechanism, **NDI-15** exhibited excellent sensitivity with a detection limit of 8.7 μM for the detection of S^{2-}.[110]

Ren *et al.* developed a turn-on activity-based fluorescent probe (**BH-HS**) consisting of a BODIPY fluorophore and a hemicyanine receptor for H_2S detection (Fig. 27). In the excited state, the TICT process from the dimethylaniline group to the hemicyanine moiety occurred, which quenched the fluorescence of **BH-HS**. The addition of (highly nucleophilic) H_2S resulted in nucleophilic addition to the iminium group of the hemicyanine, giving a product in which the TICT process was inhibited, resulting in a strong fluorescence response. **BH-HS** exhibited high selectivity towards H_2S and excellent sensitivity with a detection limit of 1.7 μM which is below the physiological H_2S concentration in the serum and the brain of mammals. **BH-HS** was also used to image the levels of exogenous and endogenous H_2S in living HeLa cells.[111]

Meng *et al.* designed an activity-based fluorescent probe (**TBF-SS**) consisting of a triphenylamine-benzofuran fluorophore and a nitrofluorobenzoate receptor (Fig. 28) for H_2S_n detection. (Note that such polysulfides also exist predominantly as anions at physiological pH). The fluorophore was linked with the

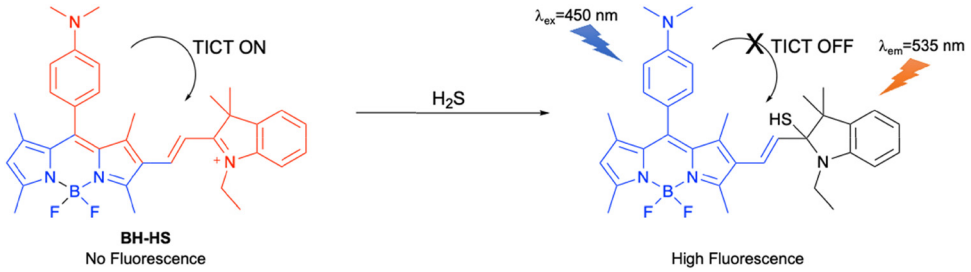

Fig. 27 The proposed mechanism of action of **BH-HS** with H_2S.

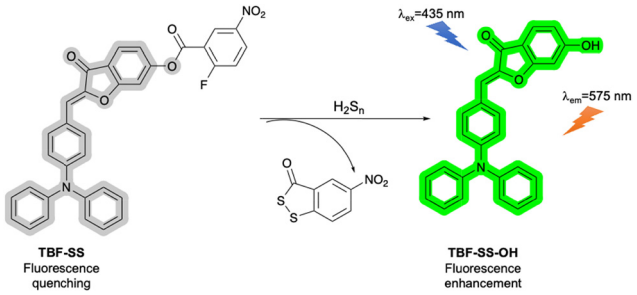

Fig. 28 The proposed mechanism of action of **TBF-SS** with H_2S_n.

receptor motif by an ester linkage. The non-coplanarity of the benzofuran unit and the nitrofluorobenzene group and the charge transfer from the triphenylamine group to the benzofuran unit resulted in the TICT effect, based on rotation around both ester C–O single bonds. This TICT process effectively quenched the fluorescence of **TBF-SS**. The addition of H_2S_n resulted in an S_NAr reaction with the nitrofluorobenzoate ring, leading to elimination of fluoride and formation of an aryl polysulfide. In the second reaction step, the other terminal sulfur atom attacks the ester carbonyl, leading to loss of an acylpolysulfide fragment, cleavage of the ester and formation of **TBF-SS-OH**. As the TICT process is no longer operative in **TBF-SS-OH**, a "turn-on" fluorescence response is observed. **TBF-SS** exhibited high selectivity towards H_2S_n, over other RSS such as H_2S. This selectivity is due to the mechanism of action of the probe, since the formation of the acylpolysulfide byproduct in step 2 is viable for H_2S_n where $n = 2$ (giving the byproduct shown in Fig. 28), $n = 3$ or $n = 4$, but not for $n = 1$. Hence, whilst H_2S can participate in the initial S_NAr step, the second step (required for the fluorescence response) does not occur. **TBF-SS** has excellent sensitivity with a detection limit of 10 nM and was used to monitor the H_2S_n levels in tea samples and to image exogenous H_2S_n in living MCF-7 cells.[112,113]

3.5 Bisulfite (HSO_3^-)

Bisulfite (HSO_3^-) has been widely used as an antioxidant and preservative in foods, beverages and pharmaceuticals.[114] On the other hand, bisulfite can lead to cell necrosis, cell division inhibition and cell death.[115] In addition, exposure to certain levels of bisulfite can cause asthma or allergic reactions.[116] Hence, it is necessary to develop fluorescent probes for bisulfite detection.

Zhu *et al.* developed a 1*H*-Benzo[*e*]indolium-based fluorescent probe (**BIFS**) for HSO_3^- detection (Fig. 29). In the excited state, an electron is transferred from the piperidinyl donor to the 1*H*-Benzo[*e*]indolium acceptor. At the same time, twisting of the piperidinyl moiety disrupts the co-planarity. The on state of the TICT process results in **BIFS** exhibiting weak fluorescence. However, the addition of HSO_3^- promoted its nucleophilic addition to the α,β-unsaturated iminium group and switched off the TICT process to achieve a strong fluorescence emission at 465 nm when excited at 322 nm. The detection limit of **BIFS** towards HSO_3^- was 3.0 nM, illustrating the excellent sensitivity of the probe. In addition, **BIFS** exhibited good cell permeability when used to image HSO_3^- in living A549 cells.[117]

Yu *et al.* developed a coumarin-based two photon fluorescent probe (**DMPCA**) for detecting HSO_3^- (Fig. 30), using a

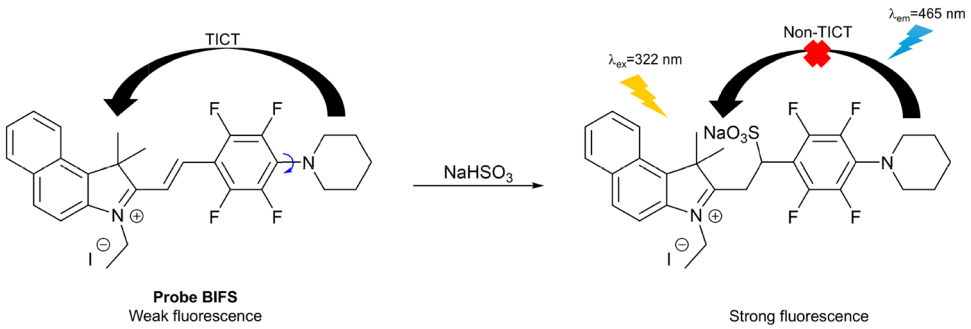

Fig. 29 The proposed mechanism of **BIFS** with HSO_3^-.

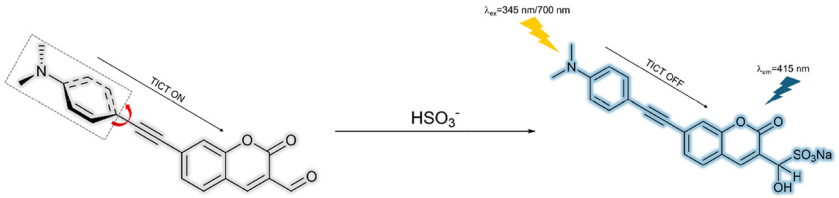

Fig. 30 The proposed mechanism of action of **DMPCA** with HSO_3^-.

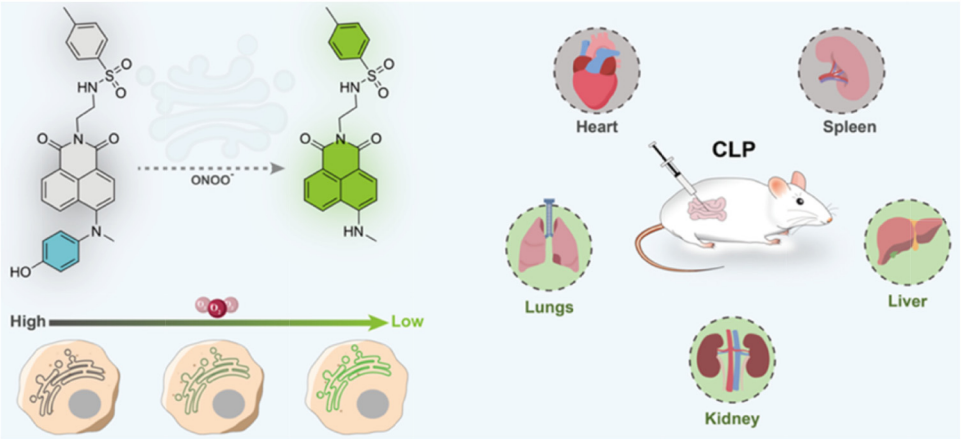

Fig. 31 The proposed mechanism of **ER-ONOO**$^-$ with $ONOO^-$ and the visualization of $ONOO^-$ in ER and CLP. Image reproduced with permission from ref. 125. Copyright 2023, American Chemical Society.

N,*N*-dimethylamino group as the electron donor to construct the TICT system. The introduction of the phenyl acetylene linker aimed to increase the two-photon absorption cross-section of the system, since previous studies on structurally similar probes had indicated that this parameter could be improved by extending the conjugation of the system.[118] HSO_3^- can react with the aldehyde, forming an adduct which turns off the TICT process and changes the fluorescence emission from weak to strong. **DMPCA** was used to image HSO_3^- in living HeLa cells under two-photon excitation, and the probe exhibited low cytotoxicity and good cell permeability.[119]

3.6 Peroxynitrite ($ONOO^-$)

Peroxynitrite ($ONOO^-$), is a ROS and reactive nitrogen species (RNS), and is a short-lived oxidant.[120,121] It is an endogenous toxicant but also a cytotoxic effector that can combat invading pathogens.[122] In addition, the production of peroxynitrite is closely associated with the pathogenic mechanisms of various diseases, such as neurodegenerative disorders, cardiovascular diseases and inflammatory diseases.[123,124] Hence, it is very important to develop fluorescent probes to monitor $ONOO^-$ in physiological systems, to further explore its biological functions and better understand the pathologies of related diseases.

Zhan *et al.* developed a two-photon turn-on fluorescent probe (**ER-ONOO**$^-$) targeting the endoplasmic reticulum (ER) for $ONOO^-$ detection (Fig. 31). The probe consisted of a 1,8-naphthalimide fluorophore, an *N*-methyl-*N*-(4-hydroxyphenyl)amino receptor and a *p*-toluenesulfonamide group used for ER targeting. When oxidative *N*-dearylation occurred upon the addition of $ONOO^-$, the TICT process was switched off and pronounced fluorescence emission at 557 nm could be observed upon excitation at 450 nm. **ER-ONOO**$^-$ exhibited a rapid response and excellent sensitivity with a detection limit of 5.2 nM towards $ONOO^-$. As expected, **ER-ONOO**$^-$ accumulated and detected $ONOO^-$ in the ER. In addition, **ER-ONOO**$^-$ exhibited good sensing performance when imaging exogenous $ONOO^-$ in living H1299 cells, monitoring the changes of $ONOO^-$ levels in a cellular hypoxia model and elucidating the functions of $ONOO^-$ in the sepsis of CLP (cecum ligation and puncture) mouse models.[125]

3.7 Potassium permanganate ($KMnO_4$)

Potassium permanganate ($KMnO_4$) has been widely used in organic and analytical chemistry, in water disinfection and in the treatment of skin infections, and exhibits potential risks for environmental pollution and human health.[126]

Wang *et al.* developed a TICT-based turn-on fluorescent probe (**OCPE**) for $KMnO_4$ detection (Fig. 32). The probe consisted of a coumarin fluorophore and an acryloyl group as a typical twisting group in which the carbon–carbon double bond worked as the response site for $KMnO_4$. The free rotation of the acryloyl group quenched the fluorescence of the coumarin fluorophore. Upon the addition of $KMnO_4$, the carbon–carbon double bond was oxidized, and the ester bond was cleaved. Due to the cleavage of the twisting group, the coumarin fluorophore

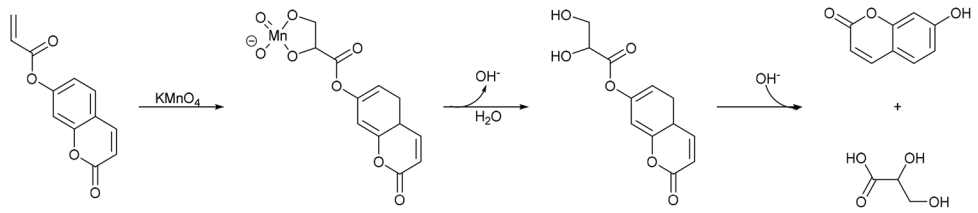

Fig. 32 The proposed mechanism of **OCPE** with $KMnO_4$.

was released and a strong fluorescence emission at 458 nm was achieved upon excitation at 342 nm. **OCPE** exhibited a rapid response (within 3 s), excellent sensitivity (LOD: 0.95 nM) and high selectivity towards $KMnO_4$. As such **OCPE**-impregnated paper test strips were fabricated to detect $KMnO_4$ in solution. In addition, **OCPE** exhibited good sensing performance when tracking solids and airborne microparticulates using a hydrogel as a carrier. **OCPE** was embedded in a polyacrylamide hydrogel with an interpenetrating network which worked as a carrier to construct the **OCPE**-hydrogel sensor. $KMnO_4$ solid could physically attach to the surface of this kind of sensor and then diffuse into the microliquid environment. Finally, $KMnO_4$ reacted with **OCPE** to switch on the bright blue fluorescence response. $KMnO_4$ solid in the range of 2.3 to 31.2 μm at amounts from 6.6 to 31.2 pg could be detected by the **OCPE**-hydrogel sensor. When it came to airborne $KMnO_4$ microparticles, the fluorescence imaging of particles which were 2.3 μm in diameter (6.6 pg) was achieved using the **OCPE**-hydrogel sensor.[126]

3.8 Dihydrogen phosphate ($H_2PO_4^-$)

Phosphate ions play a vital role in signal transduction and energy storage in biological systems and are also crucial to modern agriculture.[127] However, excess levels of phosphate can lead to the eutrophication of waterways.[128]

Shi *et al.* developed a colorimetric and fluorescent probe (**S_2**) consisting of a phenazine fluorophore and a response site based on imidazole and pyridine for $H_2PO_4^-$ detection (Fig. 33). Due to the TICT process between the pyridine and phenazine moieties, **S_2** achieved a fluorescence emission at 540 nm when excited at 416 nm. Zn^{2+} could coordinate with the nitrogen of the imidazole and pyridine groups so that the dihedral angle between the two aromatic rings decreased and the electron transfer was suppressed. Due to the recovery of the co-planarity of the conjugated system, a strong red fluorescence was observed at 600 nm when excited at 400 nm. Upon the addition of $H_2PO_4^-$, the complex (**S_2-Zn**) between **S_2** and Zn^{2+} was decomposed and the TICT process recovered. So, the fluorescence emission maximum returned to 540 nm when excited at 400 nm. In addition, **S_2-Zn** exhibited excellent selectivity towards $H_2PO_4^-$ when incorporated into paper test strips.[129a] Members from the same group had previously shown that the system also works with Cd^{2+}.[129b]

4. TICT-based fluorescent probes for small neutral molecules

4.1 Hydroxyl radical (•OH)

The hydroxyl radical (•OH) is a typical reactive oxygen species (ROS), which plays an important role in physiological and pathological processes. It is involved in the immune response to pathogens, being used to kill invading microorganisms.[130–132] However, the overproduction of hydroxyl radical may cause cell death and DNA mutations.[133] Meanwhile, hydroxyl radical is closely related to autoimmune diseases, inflammatory diseases and cancer.[131,134–136] Hence, the development of fluorescent probes for •OH detection is desirable to enable the diagnosis and evaluation of the pathologies of inflammation and cancer.

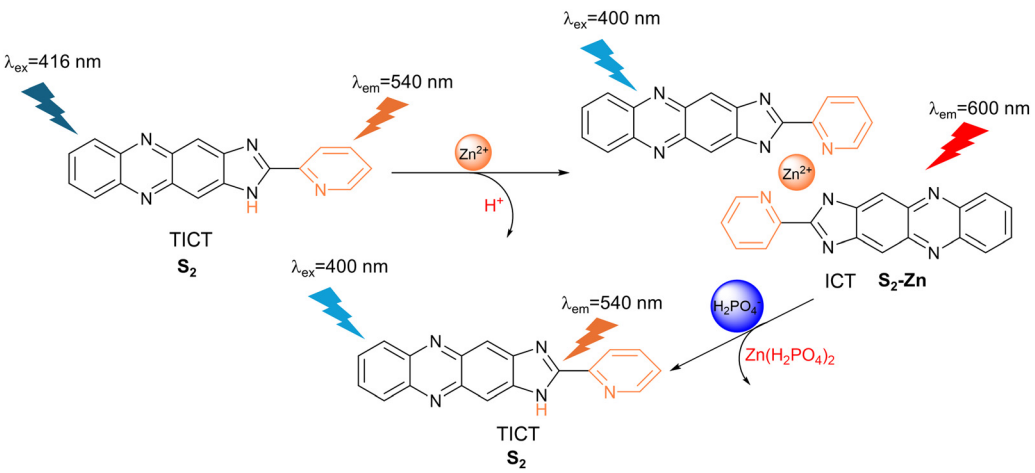

Fig. 33 The proposed mechanism of action of **S_2** with Zn^{2+} and **S_2-Zn** with $H_2PO_4^-$.

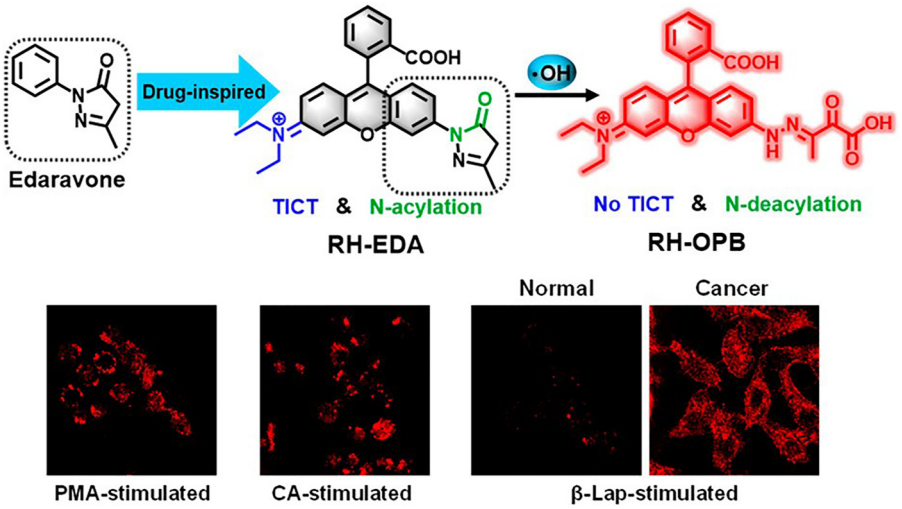

Fig. 34 The proposed mechanism of action of **RH-EDA** with •OH and fluorescence images of **RH-EDA** in living cells. PMA = phorbol myristate acetate; CA = cinnamaldehyde; β-Lap = β-lapachone. Image reproduced with permission from ref. 137. Copyright 2021, American Chemical Society.

Chen *et al.* developed a turn-on fluorescent probe (**RH-EDA**) based on edaravone and rhodamine for •OH detection (Fig. 34). In the excited state, due to the non-symmetric structure of **RH-EDA** and its intramolecular charge transfer, a strong push–pull effect can be produced, resulting in structural twisting between the diethylamino donor and the rhodamine acceptor and the formation of the TICT state. The TICT process and *N*-acyl substructure resulted in minimal fluorescence of **RH-EDA**. The addition of •OH opened the ring of the pyrazolone motif and led to the deacylation of the rhodamine nitrogen. The inhibition of the push–pull effect and the TICT process led to an increase of fluorescence at 579 nm upon excitation at 550 nm. **RH-EDA** was used to image endogenous •OH in living cells and zebrafish with high selectivity and sensitivity. Upon stimulation with β-lapachone, which is an anticancer drug used to trigger •OH generation in living cells, **RH-EDA** discriminated cancer cells from normal cells by detecting different levels of •OH.[137]

4.2 Cysteine and homocysteine (Cys/Hcy)

The proteinogenic amino acid cysteine has an essential role in intracellular glutathione regulation, however, it can also be neurotoxic due to the generation of hydroxyl radicals during cysteine autoxidation.[138] Meanwhile, cysteine has a close relationship with the pathologies of cardiovascular diseases, Alzheimer's disease, stroke, neural tube defects, venous thromboembolism, inflammatory bowel disease and osteoporosis.[139] The mechanisms of Cys/Hcy in these diseases remain unclear, so it is important to develop fluorescent probes to image and track Cys/Hcy *in vivo* for the further exploration of their function in various diseases.

Wei *et al.* constructed a two-photon TICT-based fluorescent probe (**NQ**) consisting of a quinoline fluorophore and an *N*,*N*-dimethyl group as a typical TICT twisting group for the detection of cysteine and homocysteine (Fig. 35). The perpendicular structure in the excited state and the charge-separation between the 4-ethynyl-*N*,*N*-dimethylaniline group and the quinoline-2-carbaldehyde group promoted the TICT process and resulted in fluorescence quenching. The addition of Cys or Hcy could recover the co-planarity, inhibit the TICT effect and achieve a strong fluorescence emission. **NQ** exhibited pH independence, excellent sensitivity and high selectivity towards Cys and Hcy over other analytes. **NQ** also exhibited low cytotoxicity and good sensing performance when used to monitor changes in Cys levels in living cells using two-photon excitation.[140]

4.3 Formaldehyde (HCHO)

Formaldehyde (HCHO) is a common chemical pollutant, especially found in building materials.[141] Excessive exposure to high concentrations of HCHO can lead to severe physiological responses such as lachrymation, sneezing, coughing, nausea and death.[142] At the same time, HCHO is also a reactive carbonyl species (RCS) and participates in various biological

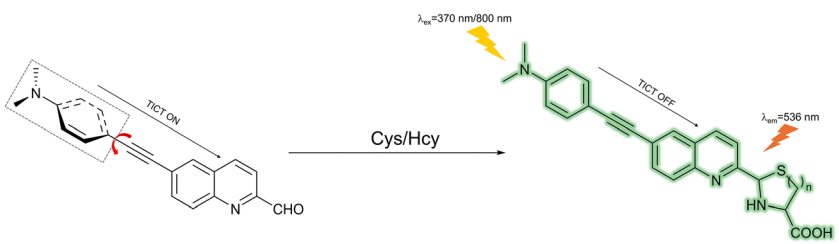

Fig. 35 The proposed mechanism of action of **NQ** with Cys/Hcy.

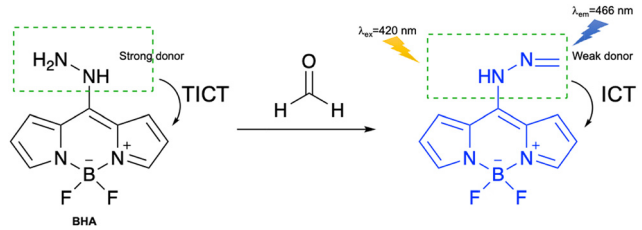

Fig. 36 The proposed mechanism of action of **BHA** with HCHO.

processes.[143–147] Hence, it is necessary to explore the development of fluorescent probes for the detection of HCHO in biological systems and the environment.

Chen *et al.* developed an activity-based fluorescent probe (**BHA**) based on BODIPY-substituted hydrazine for HCHO detection (Fig. 36). The TICT process between the 8-hydrazino group and the BODIPY fluorophore led to **BHA** being non-fluorescent. The addition of HCHO results in reaction and formation of a hydrazone, resulting in the TICT process changing to an ICT process and a fluorescence response being observed. **BHA** exhibited high selectivity towards HCHO and excellent sensitivity with a detection limit of 0.18 μM. The probe was also successfully used to image endogenous HCHO in living HeLa cells.[142]

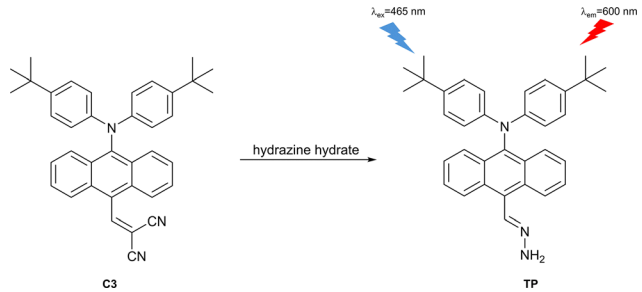

Fig. 37 The proposed mechanism of action of **C3** with NH_2NH_2.

4.4 Hydrazine (NH_2NH_2)

Hydrazine has been found in plants and the environment, and is widely used in industry, with applications including as a fuel for rocket propulsion, photographic chemicals, weapons, catalysts, corrosion inhibitors and emulsifiers.[148–150] In addition, hydrazine also serves as a synthetic intermediate to produce various drugs, such as nifuroxazide, carbidopa, hydralazine and iproniazid.[151,152] Furthermore, hydrazine is also a neurotoxin, which can lead to DNA damage and exhibits a close relationship with various diseases due to carcinogenic and mutagenic effects, such as lung damage, respiratory tract infection and liver damage.[149] Various jurisdictions set limits on the concentration of hydrazine in drinking water at a low micromolar level.[153] Hence, it is very important to develop fluorescent probes for detecting hydrazine in the environment and for monitoring hydrazine in biological systems.

Chen *et al.* developed a turn-on fluorescent probe (**C3**) with a dicyanovinyl receptor for hydrazine detection (Fig. 37 and 20 where **C3** was used for the detection of cyanide anion). In the excited state, the diphenylamine group functioned as electron donor and the dicyanovinyl group served as the electron acceptor. At the same time, the anthryl group was non-coplanar with the *N*-phenyl groups. This enabled the TICT process and hence rendered the probe only weakly fluorescent. The addition of hydrazine results in the formation of **TP** by conjugate addition to the dicyanovinyl group and subsequent loss of malononitrile. This eliminates the TICT process to achieve a strong fluorescence emission. **C3** exhibited high selectivity towards hydrazine and excellent sensitivity with a detection limit of 7 ppb.[154]

Zhou *et al.* self-assembled a turn-on nanoribbon-based fluorescent probe (**NDI-AB 1**) for detecting hydrazine hydrate (Fig. 38). A phenolic azobenzene group as an electron donor was appended to the imide nitrogen of the naphthalenediimide to construct the probe. Due to the non-planar structure and the TICT effect, **NDI-AB 1** exhibited only weak fluorescence. When dissolved in water, **NDI-AB 1** self-assembled into nanoribbons and the fluorescence was further quenched due to π–π interactions. Upon addition of

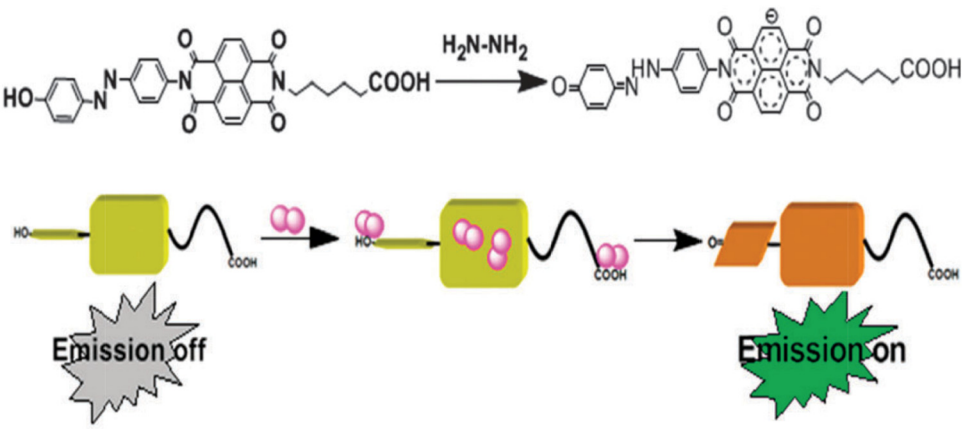

Fig. 38 The proposed mechanism of action of **NDI-AB 1** with NH_2NH_2. Image reproduced with permission from ref. 155. Copyright 2015, The Royal Society of Chemistry.

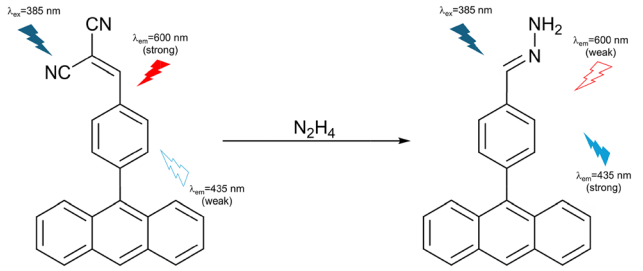

Fig. 39 The proposed mechanism of **DPA** with NH_2NH_2.

hydrazine hydrate, the hydroxy group reportedly underwent tautomerism to a quinoidal structure to inhibit the TICT process. At the same time, hydrogen bonds between hydrazine and the imide carbonyls or the quinone increased the interaction of **NDI-AB 1** with hydrazine hydrate. This led to the formation of an electron donor-acceptor (EDA) complex between the electron-deficient NDI core and the electron-rich hydrazine; the presence of the NDI radical anion in this EDA complex was confirmed by EPR spectroscopy. Because of the hydrogen bonds and the electron density of the radical anion, π–π stacking was disrupted, which led to a nano structural change from ribbons to vesicles. Finally, the radical anion as aggregates resulted in strong fluorescence emission at 405 nm when excited at 302 nm.[155]

Gupta *et al.* developed a ratiometric activity-based fluorescent probe (**DPA**) consisting of an anthracene fluorophore and a dicyanovinyl receptor for hydrazine detection (Fig. 39). The TICT process from the anthracene group to the cyano group generated red fluorescence emission at 600 nm when excited at 385 nm. The dicyanovinyl group as a receptor motif reacted with hydrazine to produce a hydrazone (by the same mechanism as for **C3**, see Fig. 37 above) and switch on the ICT process to achieve a blue fluorescence emission at 435 nm instead of a TICT-induced emission when excited at 385 nm. **DPA** exhibited high selectivity and excellent sensitivity with a detection limit of 7.85 nM. Additionally, **DPA**-loaded test paper strips were used to successfully detect hydrazine vapor.[156] It is interesting to compare the hydrazine probes **C3** and **DPA**, since they share the same dicyanovinyl receptor motif and anthracene fluorophore. However, whereas **DPA** is emissive both in the presence and absence of hydrazine (*i.e.* a ratiometric probe, where the TICT process results in a bathochromic shift of the emission), it seems that the addition of a diarylamine electron-donor motif to the **C3** structure renders the TICT process only minimally emissive, making **C3** a "turn on" probe instead.

4.5 Hydrogen peroxide (H_2O_2)

Hydrogen peroxide (H_2O_2), as a typical ROS, is the metabolite of incomplete oxygen reduction.[157] The superoxide anion ($O_2^{\bullet-}$) can be generated by the one-electron reduction of oxygen induced by electron leakage from mitochondria or the oxygenation of organic molecules by cytochrome P450 enzymes. Then, it may be converted to H_2O_2 by the action of superoxide dismutase.[158] In general, cellular H_2O_2 is generated spontaneously or enzymatically, it can diffuse across cellular membranes and it is involved in regulation of various physiological processes.[157] High levels of cellular H_2O_2 are closely related to DNA damage, cardiovascular diseases and neurological disorders.[159–161] Hence, it is desirable to develop fluorescent probes to monitor and track cellular H_2O_2 to better understand the pathologies of the diseases in which it is implicated.

Kumar *et al.* developed a dimethylaminocinnamaldehyde imine arylboronate fluorescent probe (**3**) for H_2O_2 detection (Fig. 40). Electron transfer from the dimethylamino donor to the imino acceptor led to a TICT-induced orange fluorescence emission at 566 nm. Upon the addition of H_2O_2 at pH 7.0, the arylboronate group (an electron-withdrawing group) was oxidised to a phenol moiety (an electron-donating group), which in turn increases the pK_{aH} of the dimethylamino group resulting in protonation. The inhibition of the TICT process resulted in a blue shift of fluorescence emission from 566 nm to 484 nm. To confirm this mechanism, the fluorescence behaviour of **3** at different pH values was studied. At pH 6.0, only the delocalized excited emission at 484 nm was observed while there is no TICT emission band at 566 nm. This supports the authors' proposal that protonation of the dimethylamino group can effectively inhibit the TICT process. In addition to exhibiting high selectivity towards H_2O_2 in aqueous solutions, the probe was also used to image the H_2O_2 level changes in living PC3 prostate cancer cell lines.[162]

Wu *et al.* developed a coumarin-based fluorescent probe (**Cou-CHO**) for H_2O_2 detection in conjunction with trichloroacetonitrile (Fig. 41). The TICT process resulted in weak fluorescence of the probe. However, upon the addition of H_2O_2, a reaction between H_2O_2 and the trichloroacetonitrile occurred (the Payne reaction) to produce trichloroperoxyacetamidic acid. This was followed by a Dakin oxidation, in which the nucleophilic trichloroperoxyacetamidate anion attacks the aldehyde of **Cou-CHO**. A 1,2-migration then affords a formate ester, which undergoes hydrolysis to generate **Cou-OH**. Overall, the aldehyde electron acceptor motif was transformed into a hydroxyl electron donor motif. As such, the TICT process was inhibited which led to a strong fluorescence emission. **Cou-CHO** exhibited high

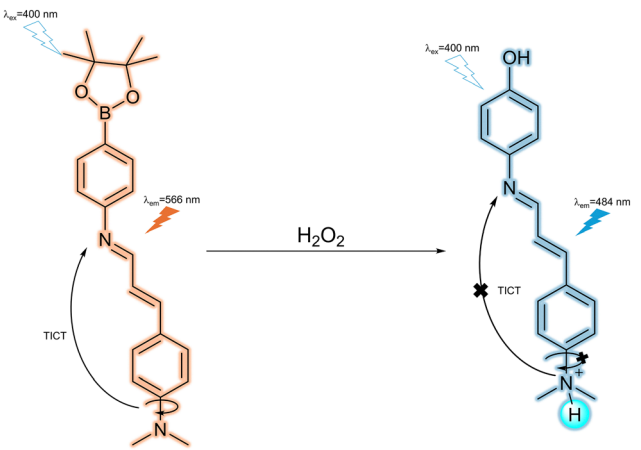

Fig. 40 The proposed working mechanism of **3** with H_2O_2.

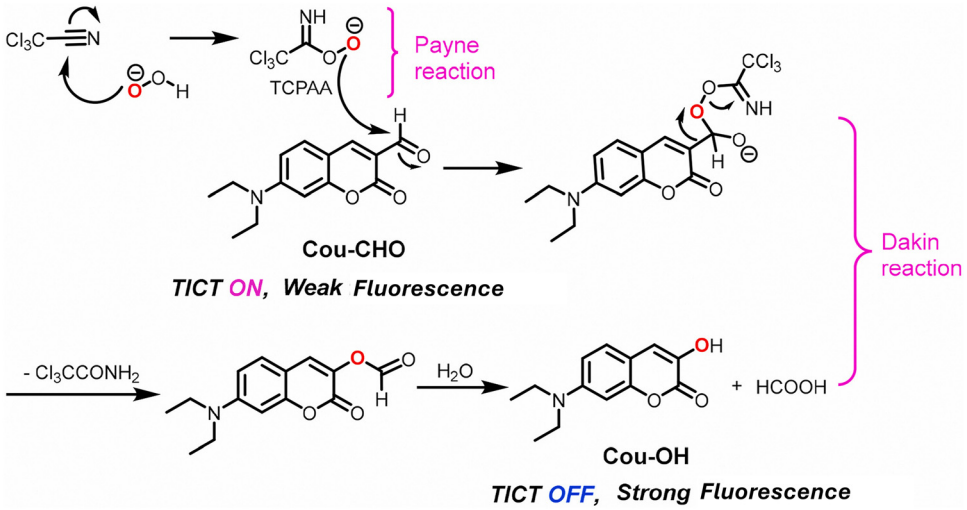

Fig. 41 The proposed mechanism of action of **Cou-CHO** with H_2O_2. Image reproduced with permission from ref. 163. Copyright 2021, Elsevier.

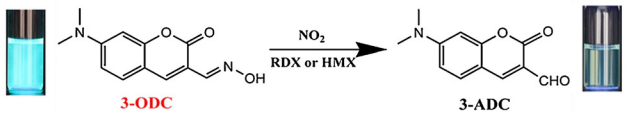

Fig. 42 The proposed mechanism of **3-ODC** with NO_2 and nitramines. Image reproduced with permission from ref. 167. Copyright 2018, Elsevier.

selectivity towards H_2O_2 over other ROS and excellent sensitivity with a detection limit of 31 nM. In addition, the probe displayed pH-independence in the range from 5.0 to 7.2. Moreover, the fluorescence intensities of **Cou-CHO** were relatively stable at pH values from 6.5 to 7.8, which supported the use of **Cou-CHO** in living systems. As such **Cou-CHO** was used for imaging exogenous and endogenous H_2O_2 in living HepG2 cells.[163]

4.6 Nitrogen dioxide (NO_2)

The detection of landmines and hidden explosives in public areas is very important from a security perspective.[164] The most common chemical explosives contain nitro groups and nitramines, which can produce oxides of nitrogen (NO_x) after exposure to photoirradiation or heating.[165] At the same time, nitrogen dioxide (NO_2) is the main component of NO_x. NO_2 is a common atmospheric pollutant, which is produced by forest fires, volcanic action, fossil fuel combustion and incineration. Overexposure to NO_2 can result in respiratory irritation.[166] Therefore, the development of fluorescent probes for NO_2 onsite detection would be helpful to deal with environmental, military and potential health threats.

Chen *et al.* selected a coumarin fluorophore and an oxime receptor to construct a turn-off TICT-based fluorescent probe (**3-ODC**) for NO_2 and nitramine detection (Fig. 42). The oxime-containing structure of **3-ODC** did not undergo TICT, resulting in strong fluorescence emission from this species at 481 nm when excited at 411 nm. The addition of NO_2 resulted in formal hydrolysis of the oxime motif to an aldehyde, giving **3-ADC**. Then, because of the twisting of the dimethylamino group, the TICT process was activated in **3-ADC**, resulting in quenching of the fluorescence. **3-ODC** exhibited high selectivity towards NO_2 and nitramines in aqueous solutions.[167]

4.7 Carbohydrate triols

Carbohydrates are the most abundant biomolecules on earth, with glucose being the product of photosynthesis.[168] They are of fundamental importance in physiological systems in roles such as energy storage and transfer, as well as being central to the pathology of diabetes, hypoglycaemia and hereditary fructose intolerance.[169–171] Hence, it is desirable to develop fluorescent probes for detecting carbohydrates in biological contexts for the exploration of relevant disease.

Oesch *et al.* developed a TICT-based fluorescent probe (**CBBA**) for detecting carbohydrate triols (Fig. 43). The probe consisted of a cyano-modified biphenyl core and a boronic acid group as the response site for carbohydrate triols. Since in the

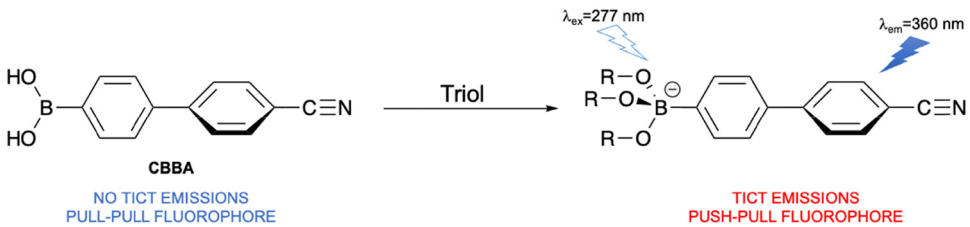

Fig. 43 The proposed mechanism of **CBBA** with carbohydrate triols.

ground-state the biphenyl dihedral angle was between 35° and 37° based on DFT calculations, **CBBA** exhibited little or no push–pull characteristics. After carbohydrate triols reacted with the boronic acid of **CBBA** and formed a sp^3-hybridized boronate ester, the boron-containing functional group was converted from an electron withdrawing group to a donating group, generating a system with push–pull electronic characteristics. Consequently, a red shift in the fluorescence spectrum was observed due to the TICT process being activated. With higher concentrations of carbohydrate triols, the fluorescence intensity increased. This probe provided a new strategy to distinguish carbohydrate triols from carbohydrate diols.[172]

Saito *et al.* developed two TICT-based turn-on fluorescent probes (**4** and **5**) for D-fructose detection (Fig. 44). The probes consisted of a *p*-(dimethylamino)phenyl-modified β-diketonato difluoroborate core and a boronic acid receptor. The TICT process resulted in only weak fluorescence for **4** and **5**. After D-fructose reacted with the boronic acid to form a boronate ester, the TICT process was inhibited, and the probes exhibited strong fluorescence emission. Of the two probes, **4** was more sensitive than **5** towards D-fructose, due to the substituent pattern (*para*-boronic acid motif) leading to direct conjugation of the donor and acceptor functional groups.[173]

4.8 Tricresyl phosphate (TCP)

Tricresyl phosphate (TCP) is an organophosphate flame retardant which has been widely used various industry sectors, such as furniture upholstery, textiles and chemical products.[174–176] However, TCP is highly toxic and inhibits the activities of key enzymes, which leads to neuropathy and reproductive toxicity.[177,178] During the production and application of TCP, it can be released and accumulate in the environment.[179] Due to the potential risks to human health, it is desirable to develop fluorescent probes for TCP detection.

Tian *et al.* used 9-(2,2-dicyanovinyl)julolidine (**DCVJ**) as a TICT-based fluorescent probe for TCP detection (Fig. 45).

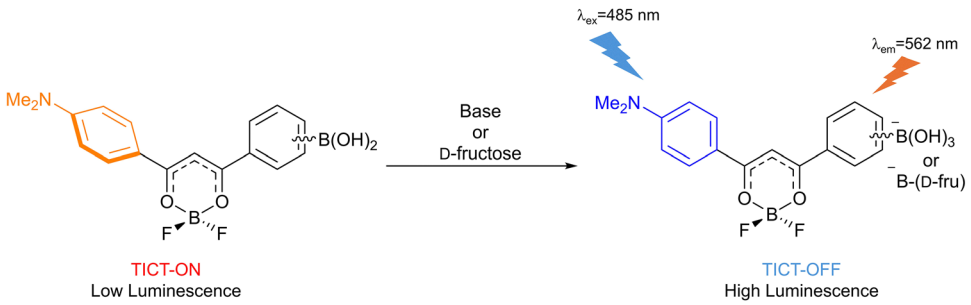

Fig. 44 The proposed working mechanism of **4** (*para*-$B(OH)_2$) and **5** (*meta*-$B(OH)_2$) with D-fructose.

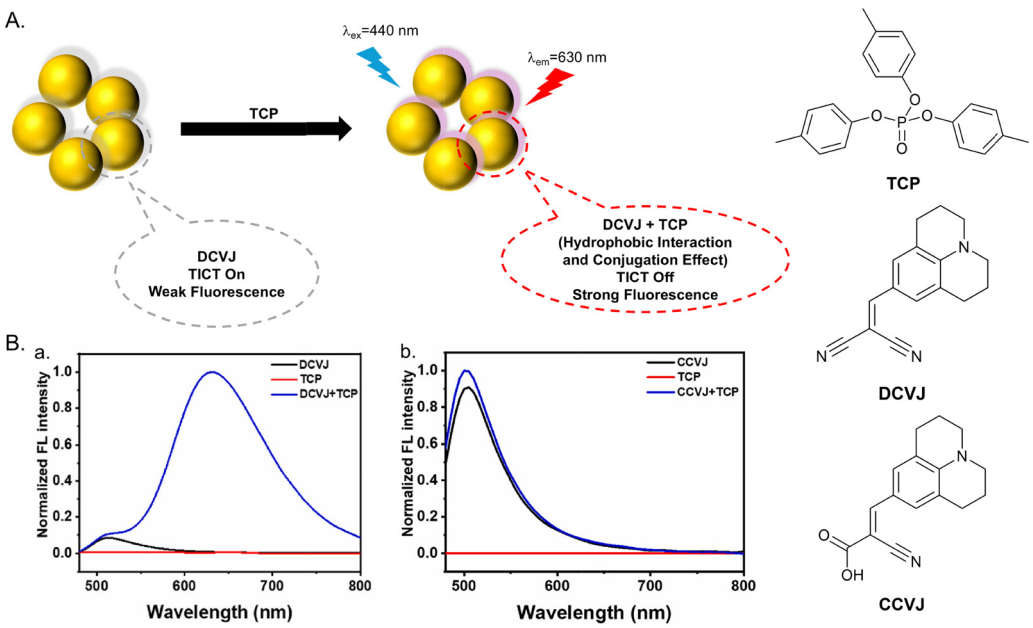

Fig. 45 (A) The proposed mechanism of **DCVJ** with TCP. (B). (a) Fluorescence spectra of DCVJ (20 μM, λ_{ex} = 440 nm, H_2O : MeOH = 13 : 2), TCP (6.67 μg mL^{-1}, λ_{ex} = 440 nm, H_2O : MeOH = 13 : 2) and DCVJ/TCP (c_{DCVJ} = 20 μM, c_{TCP} = 6.67 μg mL^{-1}, λ_{ex} = 440 nm, H_2O : MeOH = 13 : 2); (b) fluorescence spectra of CCVJ (20 μM), TCP (18 μM) and CCVJ/TCP. Image reproduced with permission from ref. 180. Copyright 2024, Elsevier.

DCVJ consisted of a julolidine core and a dicyanoalkene receptor. The construction of the D–π–A system facilitated the TICT process resulting in weak fluorescence. Both **DCVJ** and TCP are hydrophobic molecules, so it is possible for **DCVJ** to interact with TCP due to hydrophobic interactions. To confirm this hypothesis, **CCVJ** was designed, containing a cyano group with a carboxyl group to generate a hydrophilic molecule as a control molecule. After mixing with non-fluorescent TCP, **CCVJ** was unable to detect TCP, while **DCVJ** exhibited a strong fluorescence response at 630 nm. It was suggested that the hydrophilic carboxyl group reduced the hydrophobic interaction between the fluorophore and TCP, which resulted in the lack of response to TCP. The enhanced interaction between **DCVJ** and TCP blocked the rotation of the rotor of **DCVJ** resulting in inhibition of the TICT process and strong fluorescence at 630 nm upon excitation at 440 nm. **DCVJ** exhibited rapid response, pH independence, high selectivity and excellent sensitivity with a detection limit of 4.82 ng mL^{-1}.[180]

4.9 Volatile organic compounds (VOCs)

Volatile organic compounds (VOCs) are produced by daily human activities and many different industry sectors, such as household products, transportation, cooking, manufacturing, construction and fuel storage.[181–183] It is estimated that about 50–300 types of VOCs can be detected in the indoor air of schools, offices, homes, shops and other commercial buildings.[184] Many institutions have set guidelines to restrict human exposure to VOCs in workplaces, such as the National Institute of Occupational Safety and Health, the Environmental Protection Agency and the European Agency for Safety and Health.[185] Many VOCs are toxic and harmful to physiological systems, such as the respiratory, cardiovascular and immune systems.[185] Hence, it is necessary to develop fluorescent probes for the detection of VOCs in the environment to limit potential risks to human health.

Zhang *et al.* developed a fluorescent probe (**DPINO**) based on a dimethylaniline naphthol Schiff base for detecting VOCs (Fig. 46). **DPINO** was aggregated in a disordered fashion on a cellulose film, and the intermolecular voids facilitated intramolecular twisting. The nonradiative decay caused by the TICT process led to weak fluorescence emission of the probe. Upon interaction with VOCs, the intermolecular voids were filled, which resulted in the restriction of intramolecular motion and generation of a rigid conformation. Due to the inhibition of the TICT process, a strong fluorescence emission at 566 nm was observed upon excitation at 370 nm. MMA is an insensitive luminogen and does not respond to VOCs. Furthermore, it has a similar excitation wavelength to **DPINO**, so it can be used as a reference for a better visual contrast. With the inert reference frame of **MMA**, **DPINO** was used as a smart label on textiles with "VOC" lettering. Under a UV lamp, only the MMA frame exhibited fluorescence. Upon the exposure to VOCs, obvious fluorescence of the "VOC" lettering was observed, which indicates the switching on of the **DPINO** fluorescence.[186]

5. TICT-based fluorescent probes for biomacromolecules

5.1 Serum albumin (SA)

Serum albumin (SA) is the most abundant protein in plasma, and is also one of the most important proteins in human

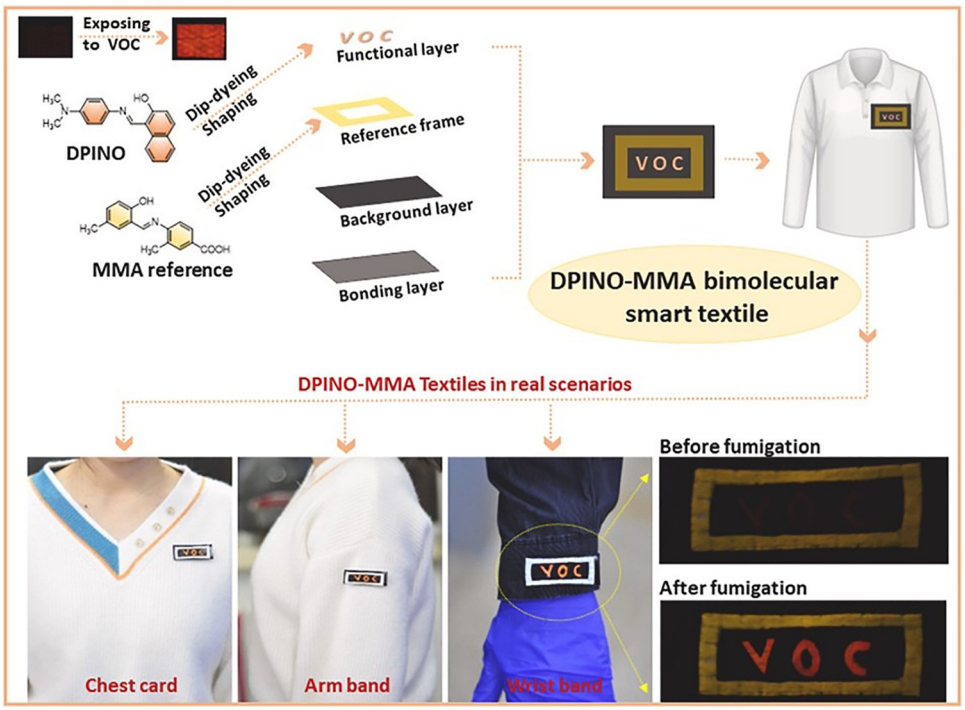

Fig. 46 The proposed mechanism of **DPINO** as a wearable smart label for detecting VOCs. Image reproduced with permission from ref. 186. Copyright 2023, Elsevier.

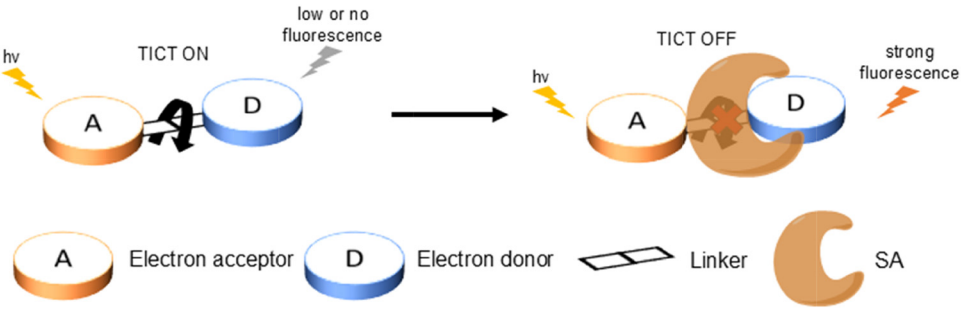

Fig. 47 Design strategy of TICT-based fluorescent probes for SA detection.

physiology.[187] Its main functions are to maintain plasma osmotic pressure and plasma volume and to transport fatty acids, drugs, hormones and metabolites.[188] The level of SA can not only have a large impact on the pathologies of cardiovascular diseases and rheumatologic autoimmune diseases, but can also act as a biomarker for COVID-19, and in nephrology and oncology.[189] Therefore, it is desirable to develop fluorescent probes for the *in vivo* monitoring and quantification of SA.

Human serum albumin (HSA) consists of three globular domains which have similar structures. Each domain has two subdomains which are called as subdomain IA, IB, IIA, IIB, IIIA and IIIB.[190] It has been suggested that subdomain IIA and IIIA are two high affinity binding sites for small heterocyclic and aromatic compounds, subdomain IB and IIIB are two binding sites for long-chain fatty acids, and albumin's *N*-terminus and a site centered around residue Cys-34 are two binding sites for metals.[191,192] These six subdomains are the dominant areas for ligand binding of HSA, and are also used for probe targeting. The sequence homology between bovine serum albumin (BSA) and HSA is close to 76%.[193,194] Due to the high structural similarity between HSA and BSA, the ability to distinguish these two types of SA becomes a difficult challenge for the design of SA detection probes.

In general, fluorescent probes for SA detection based on TICT are composed of an electron donor, an electron acceptor and a linker (Fig. 47). The linker generally comprises an alkenyl group. At the same time, in addition to participating in the construction of a push–pull system, the electron donor and the electron acceptor sometimes includes typical rotors, such as the *N*,*N*′-dimethylamino group or *N*,*N*′-diethylamino group. This kind of design can contribute to the TICT process and the "off" state of the fluorescence signal. Based on non-covalent binding, SA can block the intramolecular rotation of the probe. Due to the inhibition of the TICT process, a strong fluorescence response will be observed. Recently, TICT-based fluorescent probes for SA detection have been developed, which are shown in Table 1. Most of them are highly sensitive towards SA and exhibit excellent sensing performances for SA detection in real blood or urine samples.

5.2 Mitochondrial DNA (mtDNA)

Mitochondrial DNA (mtDNA) is composed of a closed circular double-stranded molecule of 16 569 DNA base pairs, containing 37 genes which encode 13 proteins, 22 tRNAs and 2 rRNAs.[213] mtDNA is involved in the regulation of various biological processes and the production of important biomolecules, such as NADH dehydrogenase and ATPase.[214–217] In addition, mtDNA is more sensitive to cellular damage than nuclear DNA due to the lack of protective histones, limited DNA repair mechanisms, proximity to the ETC (electron transport chain), higher replication rate and genotoxins.[218,219] Hence, it would be helpful to develop fluorescent probes to detect mtDNA in order to evaluate cellular health.

Wang *et al.* developed a dicyanoisophorone-based fluorescent probe **YON** for the visualisation of mtDNA (Fig. 48). The introduction of two electron-withdrawing dicyanoisophorone groups contributed to the construction of a linear A–π–D–π–A system to enhance the TICT effect and to impart appropriate amphiphilicity for the specific binding with mtDNA. Upon the addition of mtDNA, **YON** inserted into the minor groove of mtDNA, which then blocked the rotation of the C–C single bond of the conjugated alkenyl bond linker. As such, the TICT process was inhibited, and strong fluorescence emission at 640 nm was observed when excited at 435 nm. **YON** exhibited excellent specific binding affinity and sensitivity when used to monitor the mtDNA level changes in live HepG2 cells and realized the real-time evaluation of cellular health status during apoptosis.[220]

5.3 Ribonucleic acid (RNA)

Ribonucleic acid (RNA) is a product of cellular metabolism and has multiple functions in biological systems, such as gene regulation, protein synthesis and reaction catalysis.[221–223] RNA includes tRNA, mRNA and rRNA, among which rRNA is the most abundant RNA produced in the nucleolus.[224] The structural variations of RNA *in vivo* are closely related to the occurrence of various genetic diseases.[225,226] Hence, the development of fluorescent probes for detecting, monitoring and imaging RNA *in vivo* are useful for the diagnosis and treatment of genetic diseases.

Cao *et al.* developed a TICT-based fluorescent probe **8** for the detection and imaging of rRNA (Fig. 49). The probe consists of a naphthalimide fluorophore with a dimethyl amine group at C4. Here, the dimethyl amine group served as not only an electron donor but also a rotor. So, in the excited state, the dimethyl amine group was twisted about 90° with respect to the fluorophore core. L1-stalk, as a dynamic domain of the 23S rRNA, was

Table 1 TICT-based fluorescent probes for SA detection

Research group	Structures of probes	Binding site	LOD	Selectivity between HSA and BSA	Application
Reja *et al.*[195]	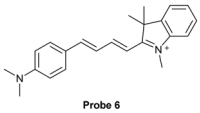 Probe 6	IIA Site I	11 nM	High selectivity towards HSA over BSA	Detection of HSA levels in human blood serum samples of hypertensive patients
Li *et al.*[196]	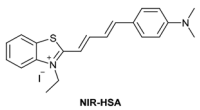 NIR-HSA	IIA Site I	26.16 nM	Responding to both HSA and BSA	Quantitative detection of HSA in urine samples of healthy volunteers
Shen *et al.*[197]	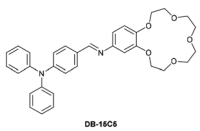 DB-16C5	α-helices from IIA and IIIA	1.7 nM (PBS buffer) 29.5 nM (artificial human urine)	High selectivity towards HSA over BSA	Quantitative detection of HSA in artificial human urine samples
Liu *et al.*[198]	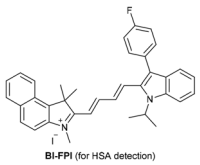 BI-FPI (for HSA detection) 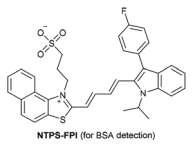 NTPS-FPI (for BSA detection)	BI-FPI: IIA Site I NTPS-FPI: II and IIIA	BI-FPI: 0.01 μM NTPS-FPI: 0.03 μM	BI-FPI: High selectivity towards HSA (the intensity in BSA 3-fold less) NTPS-FPI: High selectivity towards BSA (the intensity in HSA 2.5-fold less)	Quantitative detection of HSA and BSA in PBS buffer
Samanta *et al.*[199]	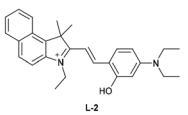 L-2	Non-site-specific binding	6.5 nM	Responding to both HSA and BSA	Detection of HSA levels in body fluid samples and artificial human urine samples
Li *et al.*[200]	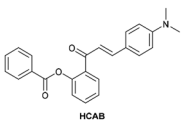 HCAB	IIA and IB	1.91 mg L^{-1}	High selectivity towards HSA over BSA	Detection of HSA levels in human blood serum samples from healthy individuals and patients with liver disease
Zheng *et al.*[201]	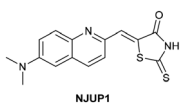 NJUP1	IIA Site I	18.1 nM	High selectivity towards HSA over BSA	Detection of HSA levels in human blood serum samples from healthy individuals and hypertension patients
Du *et al.*[202]	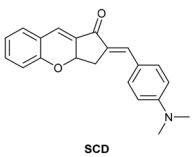 SCD	SCD not binding with site I and II SCD/Hg^{2+} complex: IIIA Site II	1.6 μg L^{-1}	Responding to both HSA and BSA	Detection of HSA levels in artificial human urine samples
Lee *et al.*[203]	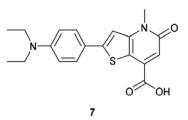 7	IIIA and the interface between IIA and IIB	8 nM	High selectivity towards HSA over BSA	Detection of HSA levels in artificial human urine samples
Luo *et al.*[204]	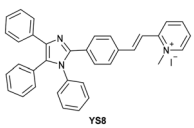 YS8	IB	0.06 μM	High selectivity towards HSA over BSA	Imaging HSA in 4T1 live cells
Ke *et al.*[205]	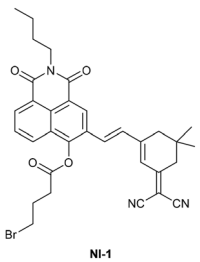 NI-1	IIIA Site II	0.21 nM	High selectivity towards HSA over BSA	Detection of HSA levels in human urine samples

Table 1 (*continued*)

Research group	Structures of probes	Binding site	LOD	Selectivity between HSA and BSA	Application
Su *et al.*[206]	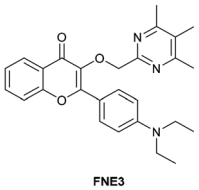 FNE3	IB	4.14 nM	High selectivity towards HSA over BSA	Detection of HSA levels in human urine samples and imaging diflunisal in live HeLa cells
Fan *et al.*[207]	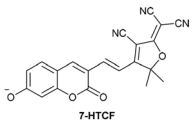 7-HTCF	IB	1.32 mg L^{-1}	High selectivity towards HSA over BSA	Detection of HSA levels in human blood serum samples
Wang *et al.*[208]	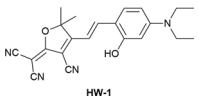 HW-1	IB	5.4 nM	Responding to both HSA and BSA	Monitoring HSA level changes in ischemia-reperfusion and nephrotoxic drug-induced AKI, and detection of HSA in human urine samples from healthy donors and patients with chronic nephritis
Zhang *et al.*[209]	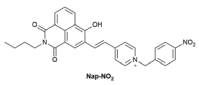	IB	0.264 μg mL^{-1}	High selectivity towards HSA over BSA	Quantitative detection of HSA in PBS buffer
Zhang *et al.*[210]	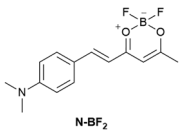 $N\text{-}BF_2$	IIIA Site II	1.21 mg mL^{-1}	Responding to both HSA and BSA	Regulation of reversible lipid droplet staining in live cells by the complex of N-BF2 and HSA
Bandyopadhyay *et al.*[211]	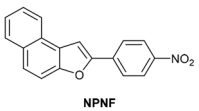 NPNF	IB	1.43 μM	High selectivity towards HSA over BSA	Detection of HSA levels in human urine samples
Dai *et al.*[212]	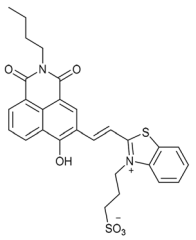 NITH	IIIA Site II	4.61 μg L^{-1}	High selectivity towards HSA over BSA	Detection of HSA levels in human urine samples of healthy donors, and imaging endogenous HSA in ER and exogenous HSA accumulating on lysosomes

selected as an rRNA model to further explore the binding mechanism between probe **8** and rRNA based on molecular docking simulations. Upon the addition of rRNA, the probe was bound in the hydrophobic core of rRNA through hydrogen bonding interactions. Due to the rigidification of the dimethylamine group and the inhibition of the TICT process, the probe exhibited a strong fluorescence response at 532 nm when excited at 450 nm. Because of the specific binding with rRNA, the probe exhibited excellent selectivity towards rRNA over other nucleic acids and biomolecules. At the same time, the probe exhibited good sensing performance and cell permeability when used to image rRNA in the nucleolus and cytoplasm of live HeLa cells.[224]

Wang *et al.* developed a near infrared fluorescent probe **QOT-NA** based on TICT with a large Stokes shift for RNA detection (Fig. 50). The probe was constructed using a furyltriphenylethylene conjugated through an alkenyl linkage with an *N*-ethylquinolinium. The TICT process led to weak fluorescence of **QOT-NA**. However, upon the addition of RNA, the V-sharped structure of the probe helped it insert into the groove of RNA due to the electrostatic attraction between the positively charged probe and the negatively charged RNA. Inhibition of the TICT process resulted in the recovery of strong fluorescence at 660 nm when excited at 540 nm in Tris–HCl buffer. However, **QOT-NA** can not only respond to RNA but also produces fluorescence response with the addition of DNA. In addition, it was also found that GSH and Sn^{4+} could affect the specific binding between the probe and RNA to some extent. **QOT-NA** exhibited excellent sensing performance and photostability when applied to imaging endogenous RNA in liver cancer cells.[227]

Jiang *et al.* developed a reversible fluorescent probe **Nu-AN** based on a 3-pyrroline modified naphthalimide for RNA detection (Fig. 51). The unrestricted twisting of the 3-pyrroline group switched on the TICT process. At the same time, the π–π stacking between the naphthalimide core and the hydrogen bonding

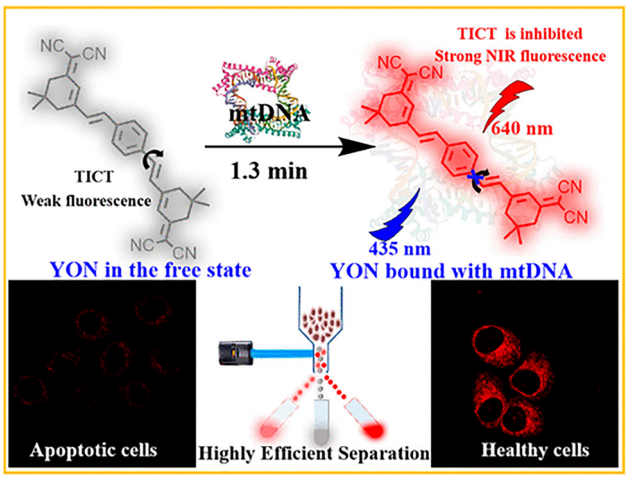

Fig. 48 The proposed working mechanism of **YON** with mtDNA. Image reproduced with permission from ref. 220. Copyright 2022, American Chemical Society.

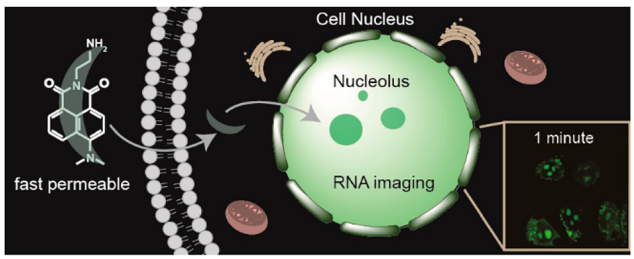

Fig. 49 The proposed working mechanism of probe **8** with rRNA. Image reproduced with permission from ref. 224. Copyright 2019, American Chemical Society.

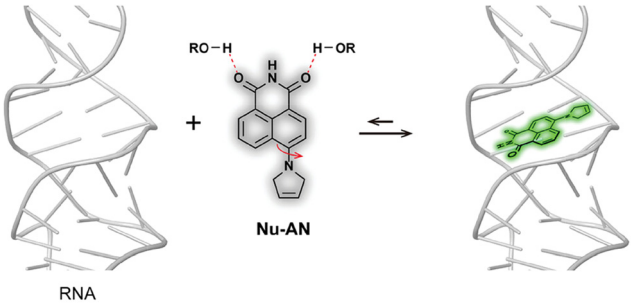

Fig. 51 The proposed mechanism of **Nu-AN** with RNA. Image reproduced with permission from ref. 228. Copyright 2024, Wiley.

between the probe and solvents also promoted fluorescence quenching. However, upon the addition of RNA, **Nu-AN** reversibly inserted into the hydrophobic pocket of RNA. Due to the steric effect in the hydrophobic pocket, the TICT process was inhibited and the hydrogen bonding interactions were reduced, resulting in a strong fluorescence response at 530 nm when excited at 465 nm. In addition, **Nu-AN** exhibited excellent selectivity towards RNA over DNA. **Nu-AN** was shown to label the nucleolus and visualize nucleolar morphology. Meanwhile, the probe was also used to observe morphological changes in nucleoli induced by ActD and Flavopiridol which are two RNA synthesis inhibitors. In addition, the reversible binding of **Nu-AN** with RNA did not interfere with nucleolus morphology, and also did not affect the photostability of the probe.[228]

5.4 Ribonuclease (RNase)

Ribonuclease (RNase) composed of endonucleases is one type of nuclease. RNase are found in various organs in the human body, and play a vital role in biological processes, such as gene replication, DNA repair, cell growth and gene recombination.[229–231]

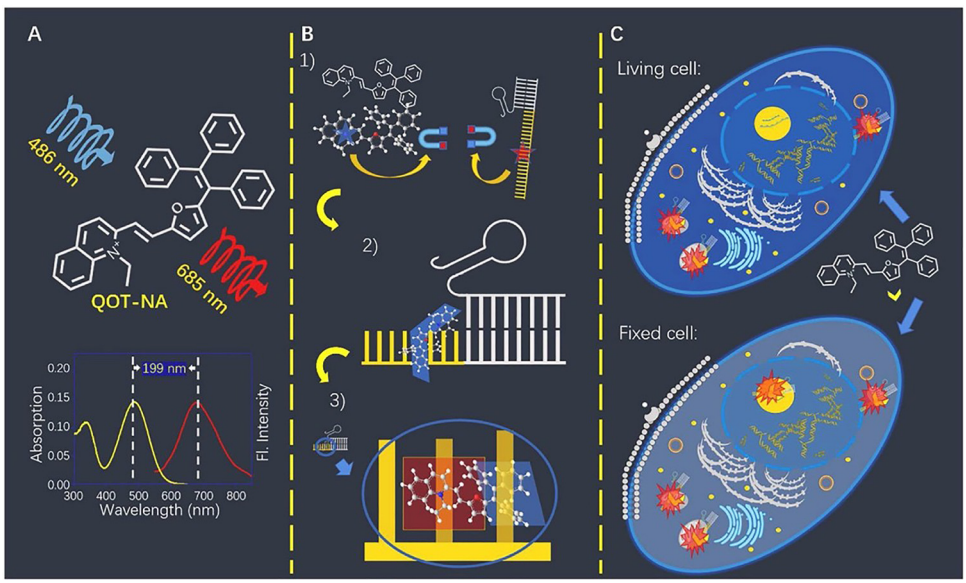

Fig. 50 The proposed working mechanism of **QOT-NA** with RNA. Absorption and emission spectra shown in (A) were acquired in pure water. Image reproduced with permission from ref. 227. Copyright 2022, Elsevier.

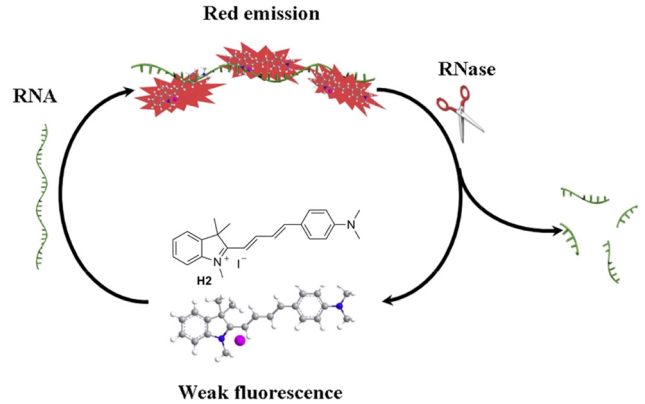

Fig. 52 The proposed working mechanism of **H2** for detecting RNase using an "off-on-off" strategy. Image reproduced with permission from ref. 235. Copyright 2018, Elsevier.

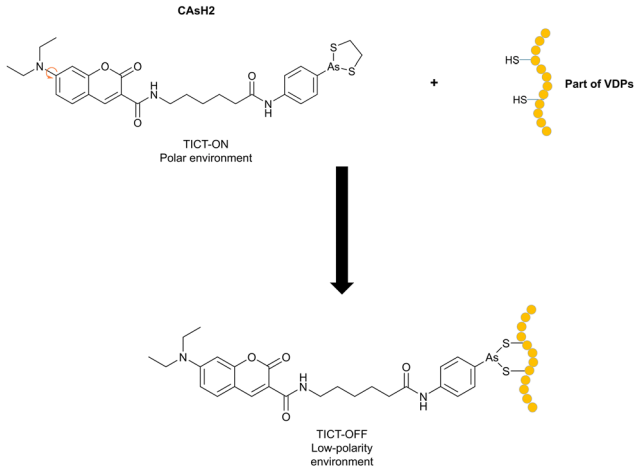

Fig. 53 The proposed mechanism of **CAsH2** with VDPs.

Clinical studies have suggested that the activities of RNase are closely related to the pathologies of various cancers, such as ovarian, pancreatic, thyroid and bladder cancer.[232,233] In addition, RNase A has also been shown to have tumour-suppressive activity.[234] Hence, it is desirable to develop fluorescent probes to monitor and track RNase *in vivo* to further understand its functions in disease pathologies.

Du *et al.* developed an off-on-off fluorescent probe **H2** for label free detection of RNase (Fig. 52). Due to the TICT process, the probe exhibited low fluorescence background. The addition of RNA promoted the formation of a **H2-RNA** complex based on the electrostatic interaction between the ammonium cation of **H2** and the phosphate anion of RNA, which switched on the strong fluorescence response at 695 nm when excited at 580 nm due to inhibition of the TICT process. Upon the addition of RNase, due to the cleavage of the phosphodiester bonds between uracil and cytosine, the hydrolysis of RNA quenched the fluorescence of the **H2-RNA** complex by releasing **H2**. The probe exhibited high selectivity towards RNase over other proteins and enzymes including DNase based on this off-on-off strategy.[235a] The same probe had previously been reported for the detection of HSA (Table 1, entry 1), as well as for the detection of casein.[235b]

5.5 Vicinal dithiol-containing proteins (VDPs)

Vicinal dithiol-containing proteins (VDPs) are native proteins with proximate cysteine–sulfhydryls used for reversible dithiol/disulfide conversions.[236] The balance between protein vicinal dithiols and disulfides ensures VDPs play an important role in the maintenance of redox homeostasis in physiological systems.[237,238] Due to their involvement in protein synthesis and related functions, VDPs have a close relationship with the development of various diseases, such as cancers, neurological diseases and human immunodeficiency virus type 1 (HIV-1).[239–242] Therefore, it is important to develop fluorescent probes for monitoring VDPs in biological contexts.

Wang *et al.* developed a ratiometric fluorescent probe **CAsH2** consisting of a 7-diethylaminocoumarin as a fluorophore unit linked to a 1,3,2-dithiarsolane as the response site for VDP detection (Fig. 53). **CAsH2** has a main ICT emission peak at 495 nm with a TICT emission peak at 550 nm due to twisting of the 5-membered dithiarsolane ring when excited at 415 nm. Upon the addition of VDPs, the protein vicinal dithiols can bind with the trivalent arsenic of the probe so that the environment of the probe changes from polar water media to the hydrophobic protein domain with lower polarity. This results in an enhancement of the ICT-induced fluorescence emission at 495 nm and the inhibition of the TICT-induced fluorescence emission at 550 nm achieving ratiometric detection of VDPs with high sensitivity (LOD: 2.6 nM) when excited at 415 nm. At the same time, **CAsH2** exhibited high selectivity, photostability and cell permeability when imaging VDPs in live cells.[243]

5.6 β-Galactosidase (β-gal)

β-Galactosidase is a glycoside hydrolase in biology and physiology.[244] The levels of β-galactosidase are closely related to the pathology of primary ovarian cancer and cell senescence.[245–249] Hence, β-galactosidase can be used as a potential biomarker for ovarian cancer.[250] As such, the development of fluorescent probes for the visualisation of β-galactosidase is of great significance for the diagnosis and treatment of ovarian cancer.

Niu *et al.* constructed a fluorescent probe **TC-gal** for β-galactosidase visualization by using a fluorophore with large conjugated structure based on tetraphenylethylene and coumarin and a D-galactose as the response site (Fig. 54). Due to the twisting at the tetraphenylethylene part, the TICT process resulted in a fluorescence off state. Then upon the addition of β-galactosidase, the galactose group of the probe was hydrolysed and the hydroxyl group was revealed. The off state of the TICT process and the on state of the ICT process led to a strong fluorescence response. **TC-gal** exhibited high selectivity towards β-galactosidase and excellent sensitivity. In addition, the probe was successfully used to image and monitor changes of endogenous β-galactosidase in live SHIN3 and senescent A549 cells.[251]

5.7 Amyloid

Alzheimer's disease is a neurodegenerative disease that has a great impact on the elderly population around the world.[252]

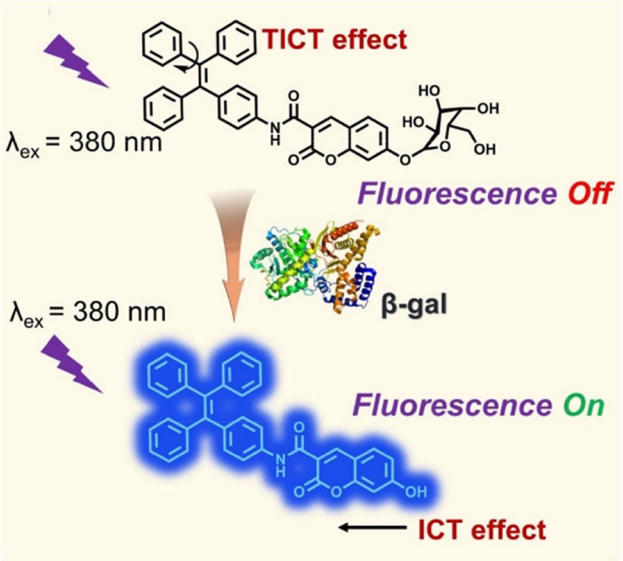

Fig. 54 The proposed working mechanism of **TC-gal** with β-galactosidase. Image reproduced with permission from ref. 251. Copyright 2021, Elsevier.

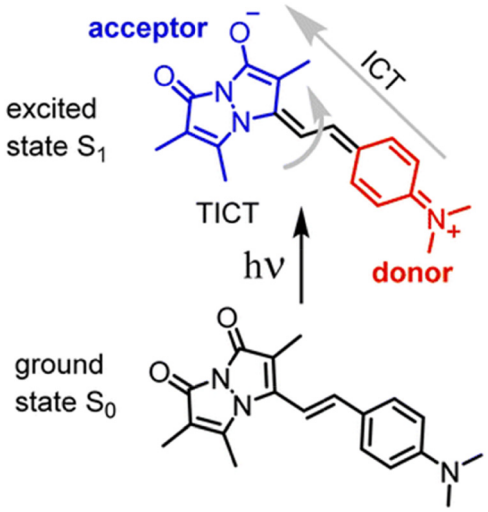

Fig. 56 The TICT mechanism of **5k**. Image reproduced with permission from ref. 260. Copyright 2024, The Royal Society of Chemistry.

The accumulation of amyloid has been closely associated with the onset and development of Alzheimer's disease,[253] in particular extracellular amyloid-β (Aβ), which accumulates and forms plaques 10 to 30 years before the onset of Alzheimer's disease.[254–256] Therefore, it is important to develop useful fluorescent probes to visualize amyloid *in vivo* for a better understanding of the pathology of Alzheimer's disease and to aid the discovery of potential therapeutics.

Yue *et al.* developed a novel near infrared fluorescent probe **DANIR 4b** for the visualisation of amyloid-β plaques (Fig. 55). The *N*,*N*′-dimethylamino group served as an electron donor and the dicyanomethylene group as an electron acceptor. At the same time, the biaryl ring system comprising a 2-phenylpyridine motif introduced a π-electron bridge with scope for twisting. The TICT process resulted in quenching of the probe. However, upon the addition of amyloid-β plaques, strong interaction with the probe blocked such rotation around the biaryl bond of the probe. The suppression of the TICT process resulted in strong fluorescence from **DANIR 4b** at 642 nm when excited at 530 nm. The probe exhibited high affinity for Aβ plaques and excellent sensing performance for amyloid-β plaques in brain sections from Tg mice and patients with Alzheimer's disease.[257]

Venkatesh *et al.* developed a turn-on fluorescent probe **5k** based on a bimane derivative with a *N*,*N*′-dimethylamino group for detecting αS fibrils (α-synuclein protein fibrillar aggregates) (Fig. 56).[258,259] αS is an intrinsically disordered protein composed of 140 amino acids and is mainly produced in the central nervous system. Its self-assembled amyloid aggregates can eventually form amyloid-rich inclusions, which are a hallmark of neurodegenerative diseases.[259] The blocking of the TICT process by αS fibrils resulted in switching on of the probe's fluorescence. **5k** exhibited high selectivity towards αS fibrils and excellent sensitivity when used to detect amplified fibrils generated from seeds extracted from brain samples of 3 patients with Alzheimer's disease and 3 patients with Parkinson's disease.[260]

Anwar *et al.* developed a turn-on rofecoxib-based fluorescent probe **RC-1** for imaging Aβ plaques (Fig. 57). The probe consists

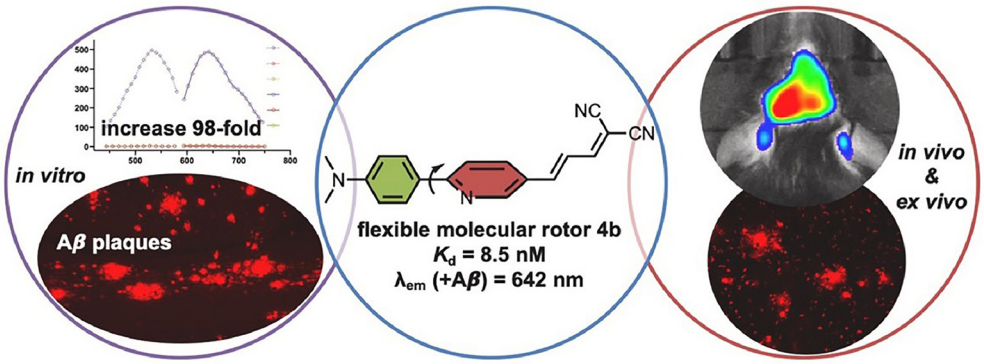

Fig. 55 The proposed mechanism of **DANIR 4b** with extracellular amyloid-β plaques. Image reproduced with permission from ref. 257. Copyright 2022, Elsevier.

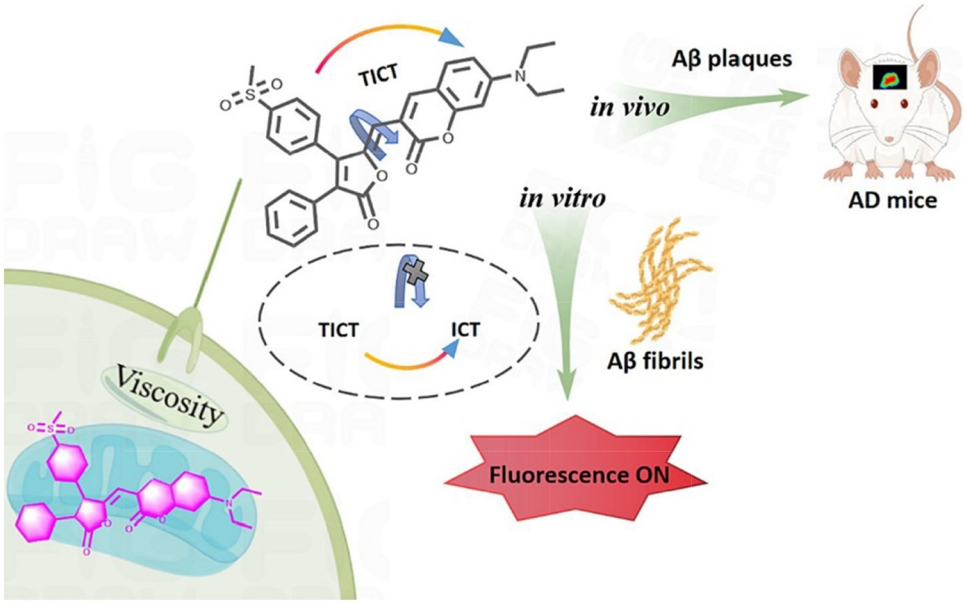

Fig. 57 The proposed working mechanism of **RC-1** with Aβ plaques. Image reproduced with permission from ref. 261. Copyright 2024, Elsevier.

of a coumarin-modified rofecoxib fluorophore and a diethylamino group as the response site as well as an electron donor. **RC-1** could insert into the hydrophobic cavity of Aβ plaques and interact with the amino acid residues His13 and 14 through hydrogen bonding and π–π interactions. The inhibition of the molecular twisting led to an inhibition of the TICT process resulting in a strong fluorescence response collected from 580 nm to 700 nm when excited at 488 nm. The probe exhibited high selectivity, excellent sensitivity with a limit of detection of 123.5 nM and mitochondria-targeting ability in live cells. In addition, **RC-1** was used to inhibit Aβ aggregation and promote the disassembly of Aβ plaques as well as to specifically image Aβ plaques by penetrating the blood-brain barrier of mice with Alzheimer's disease.[261]

Needham *et al.* developed a Thioflavin T (ThT) based fluorescent probe **THX** for visualising the formation of amyloid fibrils (Fig. 58). The design strategy involved introduction of a methoxy group to increase the electron density of the benzothiazolium core, and a pyrrolidine whose rotation could be restricted. This design improved the electron density, lipophilicity and binding affinity of the probe. Rapid rotation of the bond between the dimethylaniline and the benzothiazole switched on the TICT process resulting in quenched fluorescence. Upon the addition of wild-type αS aggregates, the intramolecular twisting was blocked and a strong fluorescence response at 587 nm was observed when excited at 488 nm. **THX** was used to visualise wild-type αS aggregates and to monitor the process of amyloid formation through protein aggregation, which provides great potential to monitor β-sheet species at the early stage of amyloid aggregation formation at the bulk and single-aggregate levels.[262]

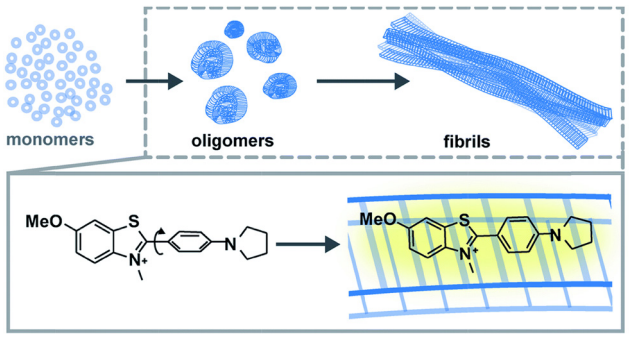

Fig. 58 Amyloid fibril formation and the proposed working mechanism of **ThX**. Image reproduced with permission from ref. 262. Copyright 2020, The Royal Society of Chemistry.

Tao *et al.* also developed a ThT-based fluorescent probe **AH-2** for imaging Aβ plaques (Fig. 59). Based on computer-aided modelling, the structure of **AH-2** was confirmed and exhibited low fluorescence background due to the TICT process and a strong intramolecular push–pull effect. The probe exhibited excellent sensitivity and high binding affinity when used to image Aβ plaques in mouse brain tissue and naturally aging live mice. In addition, **AH-2** was also used to demonstrate the efficacy of anti-AD agents using fluorescence visualisation.[263]

Wang *et al.* constructed a framework for developing hemicyanine-based fluorescent probes to visualise Aβ aggregation (Fig. 60). Using computational modelling, 15 hemicyanine derivatives (**A–C**) were designed to achieve enhanced TICT. With the growth of Aβ protein aggregatess, the size of the available binding pocket decreases accordingly. As such, probes having a large molecular size would be suitable for the large cavity of the binding site to image the protein aggregation at an early stage. Conversely, small molecular size probes can detect and image the protein aggregation at final stage. At the same time, the interaction with Aβ aggregates blocked the intramolecular twisting and switched off the TICT process resulting in strong fluorescence. Among all the probes, **A3** (λ_{ex} = 458 nm,

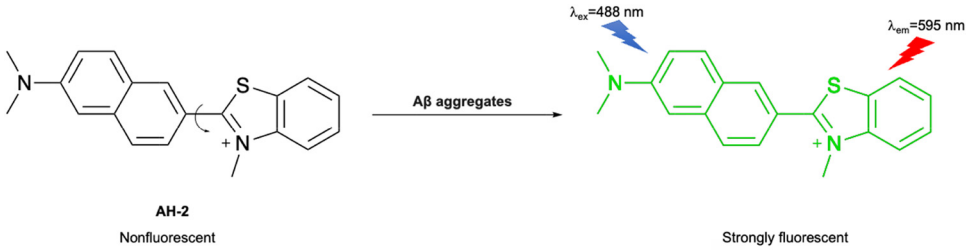

Fig. 59 The proposed working mechanism of **AH-2** with Aβ plaques.

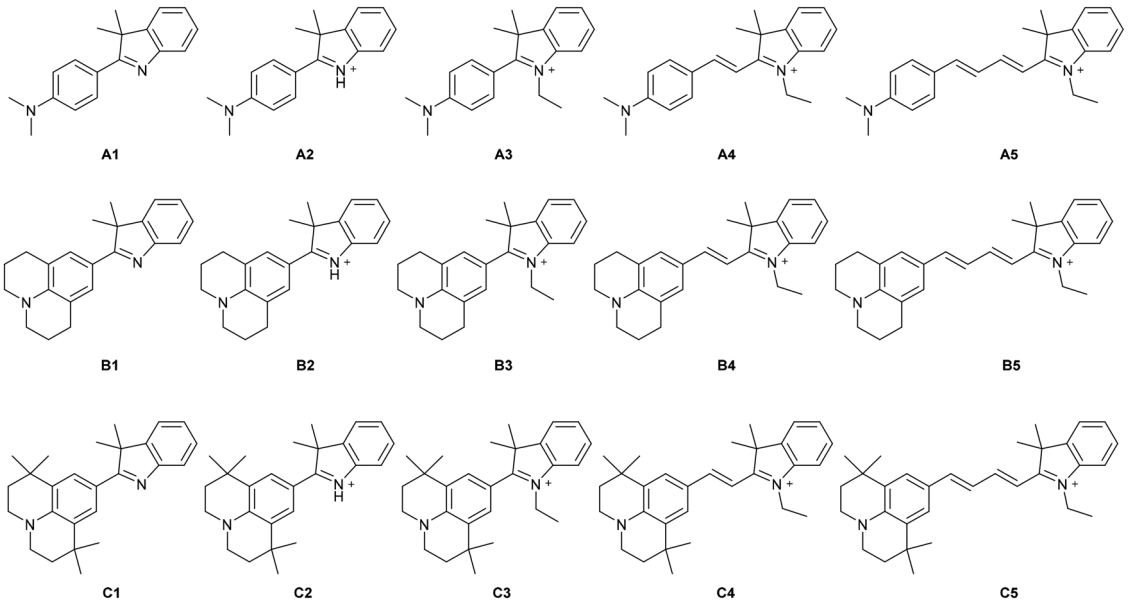

Fig. 60 The chemical structures of hemicyanine-based fluorescent probes.

λ_{em} = 500 nm, measured in DCM) could be used to monitor the final maturation of fibrils, **B3** (λ_{ex} = 482 nm, λ_{em} = 525 nm, measured in DCM) for intermediate fibril formation while **A4** (λ_{ex} = 561 nm, λ_{em} = 595 nm, measured in DCM) and **C3** (λ_{ex} = 478 nm, λ_{em} = 520 nm, measured in DCM) could be used for the early stage of aggregate formation.[264]

Miao *et al.* used a *N*,*N*-dimethylaminophenyl electron donor, a thiophene bridge and a benzo[*cd*]indol-1-ium electron acceptor to construct a TICT-based turn-on fluorescent probe **DMP2** for the visualisation of Aβ plaques (Fig. 61). After inserting into the hydrophobic pocket of Aβ plaques, **DMP2** combined with aggregated amyloid fibrils, then the *N*,*N*-dimethylaminophenyl group exhibited reduced conformational freedom and the TICT process was turned off, which resulted in the activation of NIR-II fluorescence. As such **DMP2** exhibited excellent sensitivity, selectivity, cytocompatibility and cell permeability when used to image Aβ plaques in a live mouse model.[265]

5.8 Protamine

Protamine is an alkaline protein that is rich in arginine and is positively charged.[266,267] It has pharmacological effects and is used in vascular and cardiac surgery.[268] However, excessive intake of protamine can cause a series of side effects, such as idiosyncratic fatal cardiac arrest.[269] Hence, it is important to

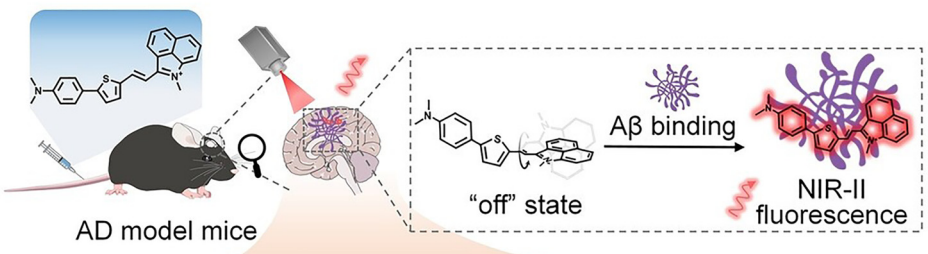

Fig. 61 The proposed mechanism of **DMP2** with Aβ plaques. Image reproduced with permission from ref. 265. Copyright 2022, Wiley.

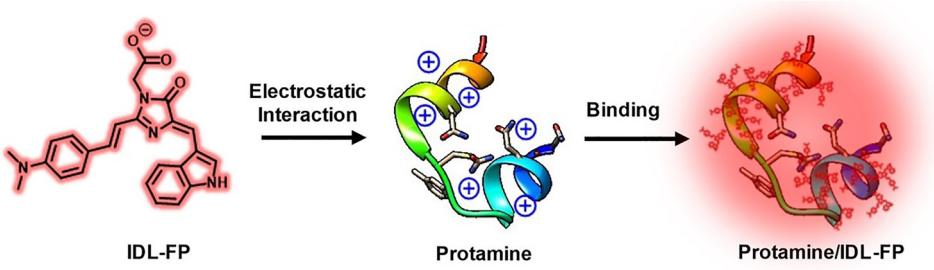

Fig. 62 The proposed working mechanism of **IDL-FP** with protamine. Image reproduced with permission from ref. 270. Copyright 2024, Wiley.

develop fluorescent probes for protamine detection and *in vivo* monitoring.

Gao *et al.* developed a TICT-based fluorescent probe **IDL-FP** for protamine detection (Fig. 62). The probe employs an alkene to conjugate a indolyl-imidazolinone scaffold as electron acceptor and a 4-dimethylaminophenyl motif as electron donor. At the same time, the anionic carboxylate group served as the response site for protamine. Due to the negative charge of **IDL-FP**, protamine could combine with the probe based on electrostatic interactions. Binding in the protein cavity suppressed the molecular twisting of **IDL-FP** and inhibited the TICT process, resulting in an enhanced fluorescence response at 630 nm when excited at 490 nm. The probe exhibited rapid response, pH independence, high selectivity and excellent sensitivity, with a limit of detection of 8.87 ng mL^{-1}. **IDL-FP** was used to detect protamine in spiked human serum samples.[270]

5.9 Cytochrome P450 (CYPs)

Cytochrome P450 (CYPs), mainly found in the liver and small intestine, are enzymes involved in the redox reactions of drug metabolism.[271] CYPs exhibit low substrate specificity and many diverse subtypes are known, of which CYP1, CYP2 and CYP3 are the three main subtypes responsible for drug metabolism.[272] As one of the most important CYP subtypes, CYP3A4 accounts for about 30% of all the CYPs in the human liver and small intestine and participates in about 50% of drug metabolism.[273] At the same time, the activity of CYP3A4 is one of the most important markers for differentiation and maturation of intestinal epithelial cells and hepatocytes, whose monitoring has great potential in drug discovery applications for regenerative medicine.[274–277] Hence, it is desirable to develop fluorescent probes for visualizing CYP3A4 for further application in the field of drug discovery.

Hanaoka *et al.* developed a rhodamine-based fluorescent probe **2-Me PeER** for the visualisation of CYP3A4 (Fig. 63). The introduction of a methyl group at the *ortho* position of the dialkylamino group led to the steric repulsion between the methyl group and the alkyl group on the nitrogen atom, which disrupted the co-planarity of **2-Me PeER**. This enhancement of the TICT process quenched the fluorescence of the probe. At the same time, a long alkyl chain was introduced to improve the lipophilicity of the probe, in order to achieve high binding affinity for CYP3A4. Upon the addition of CYP3A4, **2-Me PeER** was *N*-dealkylated resulting in strong fluorescence at 550 nm

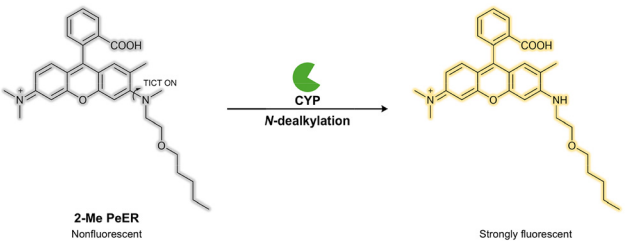

Fig. 63 The proposed working mechanism of **2-Me PeER** with CYPs.

when excited at 520 nm. **2-Me PeER** exhibited excellent sensing performances when monitoring the activity of CYP3A4 with excellent selectivity and sensitivity *in vitro* and in live HepaRG cells. In addition, the probe was used to visualize mature hepatocyte-like cells with high CYP expression, which highlights its great potential in the application as a cell sorter.[278]

5.10 β-Lactoglobulin (β-LG)

β-Lactoglobulin (β-LG) is a type of globular protein which is composed of a polypeptide backbone with α-helix motifs containing 162 acidic/basic and hydrophilic/hydrophobic amino acids.[279] As one of the proteins in whey, β-LG is also an allergen in dairy products.[280,281] The allergic reactions induced by β-LG result in skin redness, hives, skin itching and gastrointestinal discomfort.[282,283] For newborn babies, milk allergy can in some cases affect their normal growth.[284] Therefore, it is crucial to develop fluorescent probes that can detect β-LG easily and with high selectivity and sensitivity to effectively avoid β-LG associated allergy hazards.

Gadly *et al.* developed a TICT-based fluorescent probe **GEM-DNS** consisting of a gemcitabine derivative modified by a dansyl group for β-LG detection (Fig. 64). The TICT process resulted in quenched fluorescence of **GEM-DNS**. However, upon the addition of β-LG, the probe inserted into the hydrophobic pocket of β-LG. This tight interaction based on electrostatic interactions blocked the rotation of **GEM-DNS** and suppressed the hydrogen bonding interactions between the probe and water, which resulted in a strong fluorescence response from **GEM-DNS**. **GEM-DNS** exhibited pH and temperature dependence. In addition, the probe was used to detect β-LG in real milk and whey samples with excellent selectivity towards β-LG and high sensitivity.[283]

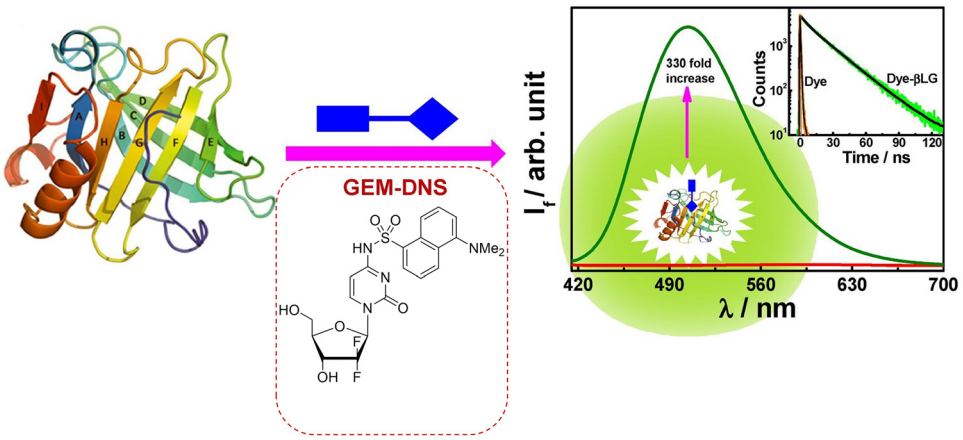

Fig. 64 The proposed mechanism of **GEM-DNS** with β-LG. Image adapted with permission from ref. 283. Copyright 2023, Elsevier.

6. TICT-based fluorescent probes for visualizing cellular microenvironments or interrogating biomolecular interactions

Intracellular viscosity is one of the most important parameters to evaluate the cellular microenvironment, and plays a vital role in signal transduction, biomolecular interactions and metabolite diffusion.[285–287] Due to the diversity in composition of organelles, the intracellular microenvironment is extremely heterogeneous, resulting in regional differences in viscosity.[288,289] Recent studies have shown that abnormal intracellular viscosity is closely related to various diseases, such as inflammation, diabetes, fatty liver disease, atherosclerosis, hypertension, Alzheimer's disease, Parkinson's disease and malignant tumours.[290–296] Hence, the development of fluorescent probes for visualizing intracellular viscosity will help to further understand the pathologies of related diseases, and provide potential for the diagnosis and future treatment of these diseases.

In general, the strategy of developing a TICT-based fluorescent probe for viscosity visualisation is to use a conjugated linker to combine an electron-donating group and an electron-withdrawing group to construct a D–π–A system (Fig. 65). The π-conjugated linker undergoes rotation to promote the TICT process. Under high viscosity conditions, the twisting of the linker is disfavoured, inhibiting the TICT process and switching on the fluorescence emission. Recent research focused on TICT-based fluorescent probes for viscosity detection are included in Table 2.

In addition, due to the special working mechanism (Fig. 66), TICT-based fluorescent probes can be used to distinguish and mark different organelles based on polarity. When a TICT-based fluorescent probe is excited from the ground state to the LE state, highly polar environments facilitate the intramolecular rotation and the TICT process to achieve a fluorescence emission with longer wavelength or a nonradiative relaxation from TICT to GS′.[320] On the other hand, less polar environments inhibit the TICT process and let the radiative transition of the molecule occur from the LE state to the ground state to achieve a fluorescence emission with shorter wavelength.[321] Recent research focused on TICT-based polarity-responsive fluorescent probes for the visualisation of organelles are summarised in Table 3.

Duangkamol *et al.* developed a novel TICT-based coumarin fluorescent probe **LD-PYR** for the visualisation of lipid droplets in cancer cells (Fig. 67). The probe consists of a coumarin-based electron acceptor and a pyrene-based electron donor. **LD-PYR** exhibits excellent sensitive to polarity and viscosity, and could achieve fluorescence emission intensity changes at about 560 nm when excited at 420 nm. Lipid droplets are normally present at higher levels in cancer cells than in healthy cells.[326–328] At the same time, the components in lipid droplets are more hydrophobic and viscous than the cytosol. As such, due to

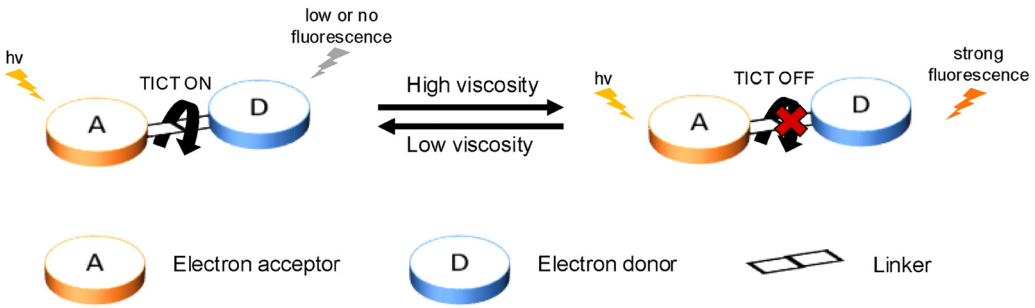

Fig. 65 The normal design strategy of TICT-based fluorescent probes for viscosity visualisation.

Table 2 TICT-based fluorescent probes for viscosity detection

Research group	Structure of probe	Application
Dai *et al.*[297]	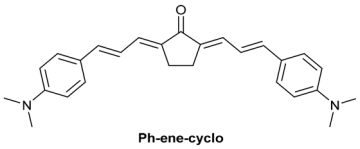 Ph-ene-cyclo	One- and two-photon fluorescence imaging for viscosity in nystatin-induced HeLa cells
Zhang *et al.*[298]	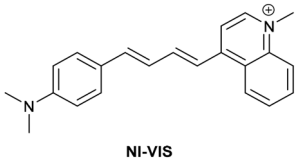 NI-VIS	Detection of ionophore-induced cellular viscosity changes in mitochondria, monitoring the viscosity during mitophagy, imaging viscosity in cirrhotic liver tissue and monitoring viscosity in zebrafish
Tang *et al.*[299]	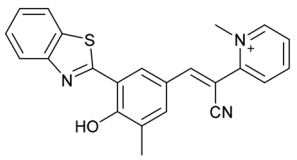 HBTD-V	Detection of viscosity changes in live MCF-7 cells and staining of the mitochondria, as well as visualisation of inflammation-induced viscosity change of cytosol in the liver of live mice
Chen *et al.*[300]	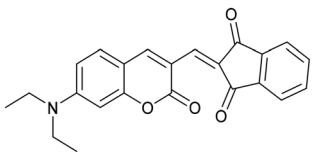 ACI	Monitoring the viscosity changes in monensin-induced or nystatin-induced live HeLa cells
Sun *et al.*[301]	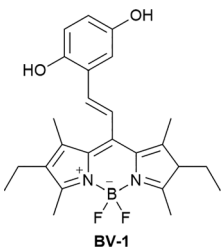 BV-1	Detection of intracellular viscosity change upon treatment with ionophores in live A549 cells
Liang *et al.*[302]	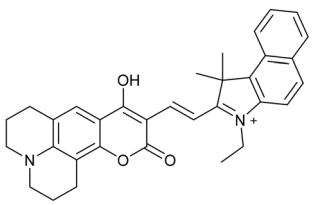 Mito-VCI	Monitoring mitochondrial viscosity with FLIM imaging in live HeLa cells, visualisation of viscosity changes in the tissues from LPS-induced inflammation in mice, and imaging viscosity changes due to inflammation in zebrafish
Zhang *et al.*[303]	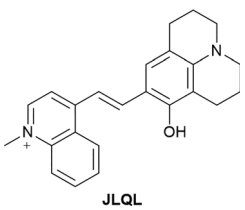 JLQL	Monitoring the mitochondrial viscosity changes in live A549 cells treated with monensin or nystatin, and visualization of viscosity variation during mitochondrial autophagy
Wang *et al.*[304]	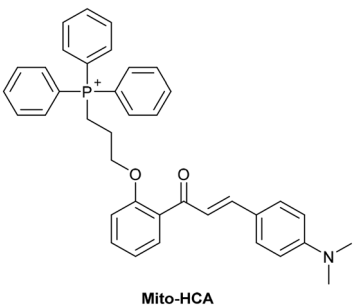 Mito-HCA	Imaging mitochondrial viscosity changes under osmotic shock, starvation stress and ionophore incubation

Table 2 (*continued*)

Research group	Structure of probe	Application
Zhang *et al.*[305]	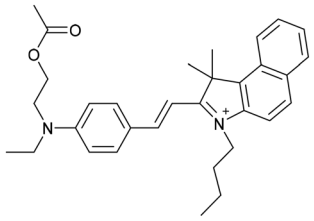 YD-Mito	Visualisation of viscosity changes in live A549 cells incubated with nystatin
Fu *et al.*[306]	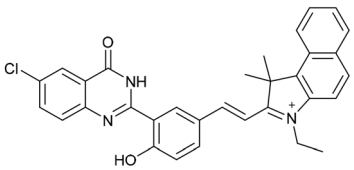 HPQ-BI-V	Imaging viscosity changes in live HepG2 cells incubated with nystatin or rotenone and in LPS-induced cellular acute inflammation model, and visualisation of viscosity changes in zebrafish and mice during acute inflammation
Tang *et al.*[307]	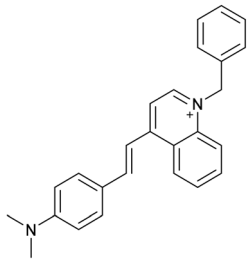 Mito-ND	Monitoring the intracellular mitochondrial viscosity changes in live HeLa cells treated with nystatin or monensin, and visualisation of viscosity changes in live zebrafish, mouse tumour slices, live mice and mouse liver/kidney injury
Song *et al.*[308]	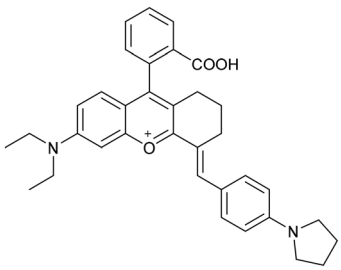 BP-III	Real-time observation with viscosity changes in live cells induced by nystatin, and imaging in living mouse fatty liver disease model based on viscosity difference
Cheng *et al.*[309]	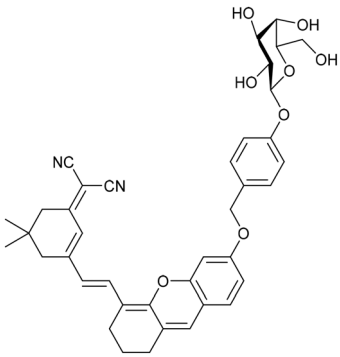 YF-V	Monitoring viscosity changes in live glucose-induced HL-7702 cells, and imaging organ damage in diabetic mice based on fluorescence lifetime
Hao *et al.*[310]	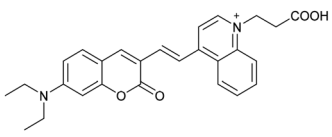 HCT	One- or two-photon monitoring of viscosity changes in live nystatin-induced or monensin-induced HeLa cells, and imaging of viscosity changes in mice liver tissue slice and live mice stimulated by LPS, nystatin and monensin

Table 2 (*continued*)

Research group	Structure of probe	Application
Zong *et al.*[311]	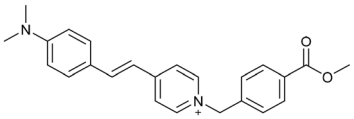 NP	Detection mitochondrial viscosity in live nystatin-induced or monensin-induced MCF-7 cells, in mouse skeletal muscle and liver tissue, and monitoring mitochondrial viscosity during apoptosis, and distinguishing human breast cancer cells from normal cells based on the mitochondrial viscosity difference
Ma *et al.*[312]	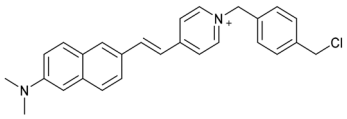 NS-V	High-fidelity imaging of mitochondrial viscosity changes in abnormal living HeLa cells, and monitoring viscosity changes in living mice with gastritis by oral administration
Liu *et al.*[313]	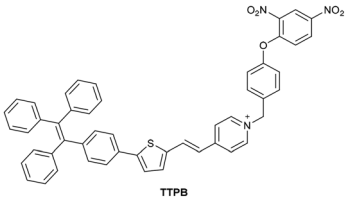 TTPB	Detection of mitochondrial viscosity in live MCF-7 cells treated with nystatin, monensin and LPS, and monitoring the viscosity changes during autophagy
Zhang *et al.*[314]	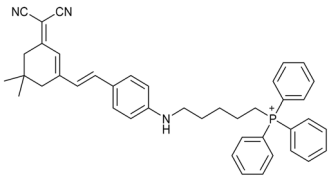 ZVGQ	Detection of mitochondrial viscosity changes in live nystatin-induced or rotenone-induced U87MG cells, and *in vivo* imaging in orthotopic glioblastoma models
Zhang *et al.*[315]	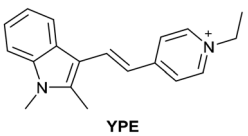 YPE	Monitoring drug-induced changes in mitochondrial viscosity in live HeLa cells, and distinguishing cancer cells from normal cells based on viscosity differences
Chao *et al.*[316]	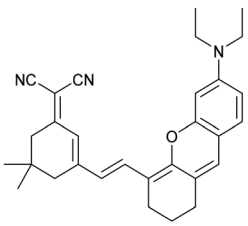 IX-V	Imaging viscosity changes in live drug-induced HeLa cells, distinguishing cancer cells from normal cells based on viscosity differences, and visualisation of tumours in live mice models as well as photoacoustic imaging
Yang *et al.*[317]	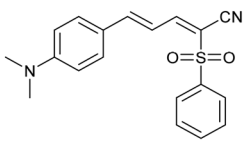 PPF-1	Monitoring viscosity changes in live drug-induced HeLa cells, and ability to target lipid droplets
Zhang *et al.*[318]	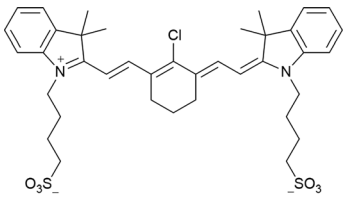 IG-Lyso	Monitoring lysosomal viscosity changes during autophagy and ferroptosis, distinguishing cancer cells from normal cells based on viscosity differences, and imaging tumours in live mice models
Hu *et al.*[319]	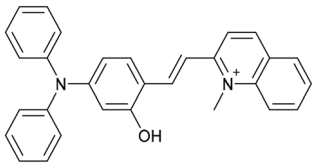 L-TPQ	Monitoring lysosomal viscosity changes in live drug-induced HepG2 cells and tracking mitophagy, and imaging lysosomal viscosity in the liver tissues of a NAFLD mouse

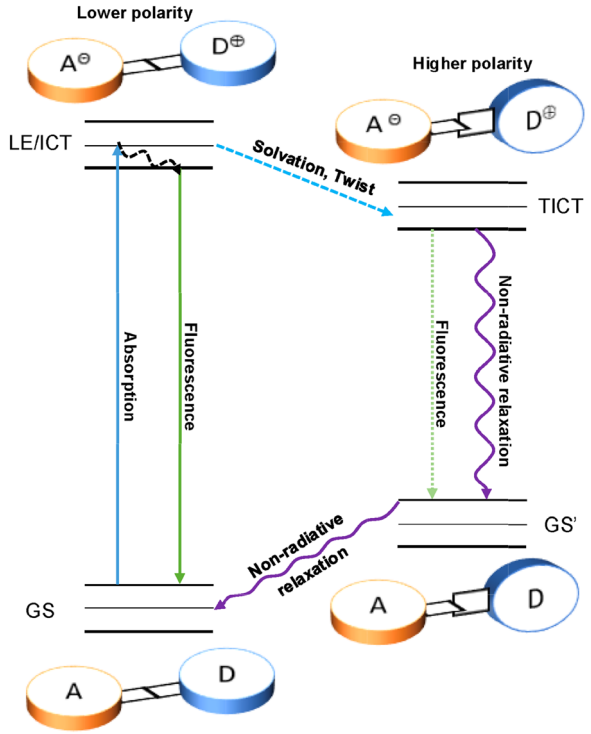

Fig. 66 The proposed polarity-responsive mechanism of TICT-based fluorescent probes.

microenvironmental differences, **LD-PYR** was used to image lipid droplets and distinguish cancer cells from normal cells.[329]

Zhou *et al.* designed a rhodamine-based fluorescent probe **Rh-NH** for lysosome imaging (Fig. 68). Substitution of the *N*,*N*-dialkyl group in rhodamine with a pyrrole enhanced the intramolecular TICT process. The spirolactone form of **Rh-NH** under physiological conditions achieved excellent cell permeability. The acidic, low-polarity and highly-viscous conditions found in lysosomes inhibited intramolecular rotation and switched on the fluorescence of **Rh-NH** to achieve a strong fluorescence response. **Rh-NH** was used to monitor the movement and dynamic constitution of lysosomes in real time based on STED imaging.[330]

Hanaoka *et al.* developed a series of N-Ph rhodamine based fluorescent probes to label proteins for no-wash-out imaging and real-time pulse-chase experiments which facilitated the real-time imaging of protein expression (Fig. 69). Due to the rotation of the xanthene–N bond, the TICT of the probe was on and quenched the fluorescence emission. When the rotation of the xanthene–N bond was suppressed, the fluorescence emission of the probe was recovered. The key strategy to design N-Ph probes focused on the twisting of the xanthene–N bond. As such, the probes consisted of a N-Ph rhodamine dye linked with a ligand near the xanthene–N bond for targeting proteins. After the probe bound with the target protein, twisting of the xanthene–N bond was suppressed to inhibit the TICT process, resulting in recovery of strong fluorescence emission of the N-Ph rhodamine. Based on this strategy, **Halo rhodamine-4** and **SNAP rhodamine-3** were designed to image live HEK293T cells whose surface expressed Halo Tag or SNAP Tag transiently, which are two commonly-used tags used for covalent labelling inside living cells. **Halo rhodamine-4** bound with Halo Tag protein covalently, and the resultant rigidification of the xanthene–N bond helped the probe to achieve strong fluorescence response. The working mechanism of **SNAP rhodamine-3** with SNAP-tag protein was based on the same strategy to that of **Halo rhodamine-4**. In addition, **Halo rhodamine-4** was used in pulse-chase experiments to image protein expression in real time and image Halo Tag-HA-expressing neocortex neurons in fixed mouse brain slices.[331]

7. Fluorescent probes based on combined sensing mechanisms

The combination of TICT with other fluorescence mechanisms such as photoinduced electron transfer (PeT) or TICT with aggregation-induced emission (AIE) can merge the favourable properties of both processes, thereby overcoming many limitations of TICT dyes.

7.1 PeT/TICT

The photoinduced electron transfer (PeT) mechanism is a particularly important design strategy for the development of "off–on" or "on–off" fluorescent probes. In the presence of a target analyte, the recognition/activating group binds to the target analyte, either restricting PeT and turning on the fluorescence ("off–on") or activating PeT and turning off the fluorescence ("on–off").[332] Therefore, the combination of PeT and TICT can provide fluorescent probes with high selectivity and sensitivity.

The synergy between PeT and TICT can be described as a "cascade control" strategy, where the two processes act sequentially to regulate fluorescence emission. In this cascade, PeT serves as the primary switch, providing a high-contrast "on/off" fluorescence ratio, and TICT acts as a secondary mechanism that makes the probe environmentally sensitive (*e.g.* to viscosity of the surrounding environment). As an efficient fluorescence quenching mechanism, the PeT process provides an extremely high "on/off ratio", ensuring that the probe exhibits extremely low background fluorescence prior to target recognition. In contrast, the TICT mechanism is often endowed with environmental responsiveness (*e.g.*, to viscosity or polarity) or serves as the primary luminescence channel once PeT is switched off. Their modes of integration can be summarized as follows: target analytes first achieve primary "on/off" control of the fluorescence signal by inhibiting or activating the PeT process; subsequently, the TICT process, which is determined by intramolecular rotational freedom, performs secondary modulation of the fluorescence signal (such as enhancement, shift, or lifetime variation), thereby converting recognition events into richer and more sensitive outputs of environmental information. Alternatively, the probe undergoes PeT and TICT processes in its initial state, resulting in extremely weak fluorescence signals. Then when the target analyte is present, the PeT process is diminished, leading to a partial recovery of the fluorescence signal. Moreover, in a

Table 3 TICT-based fluorescent probes for polarity detection

Research group	Structure of probes	Application
Meng *et al.*[322]	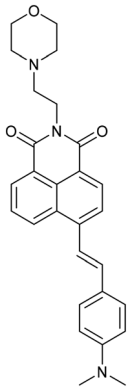 LD-Lys	Simultaneous two-colour visualization of lipid droplets with bright yellow emission and lysosomes with weak red emission, tracking the dynamic changes of lipid droplets and lysosomes, and the visualisation of the morphology, distribution and size of lipid droplets and lysosomes in live mouse tissue
Zhang *et al.*[321]	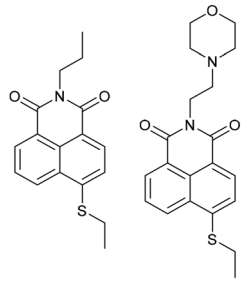 S-NAT S-NAT-M	Distinguishing endoplasmic reticulum and lipid droplets using green and blue emission of S-NAT, distinguishing lipid droplets and lysosomes by green and blue emission of S-NAT-M, and monitoring the changes of lipid droplets in high-fat conditions and upon high-temperature treatment
Cao *et al.*[323]	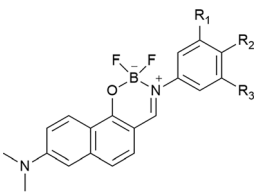 **BBA-H**: R_1=R_2=R_3=H **BBA-OMe**: R_1=R_3=H, R_2=OMe **BBA-NMe$_2$**: R_1=R_3=H, R_2=NMe$_2$ **BBA-CF$_3$**: R_1=R_3=CF$_3$, R_2=H **BBA-CN**: R_1=R_3=H,R_2=CN **BBA-NO$_2$**: R_1=R_3=H, R_2=NO$_2$	Super-resolution SIM imaging of cytosolic and nuclear lipid droplets using BBA-CF$_3$, and tracking cytosolic lipid droplet fusion process.
Feng *et al.*[324]	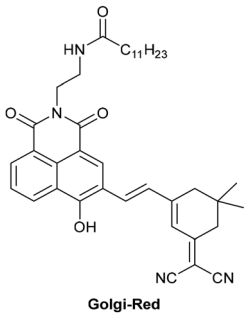 Golgi-Red	Monitoring polar changes in the Golgi apparatus in live HeLa cells
Zhao *et al.*[325]	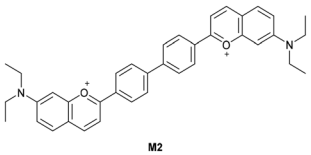 M2	Imaging and labelling various types of cancer cells based on fluorescence and FLIM, and monitoring the plasma membrane polarity changes in sorafenib-treated cancer cells during cell ferroptosis

high-viscosity environment, the rotation of the probe is inhibited, which further disrupts the TICT process and thus enables the complete recovery of the fluorescence signal. This design enables the probe not only to detect the presence of the target but also to simultaneously reveal the characteristics of its microenvironment.

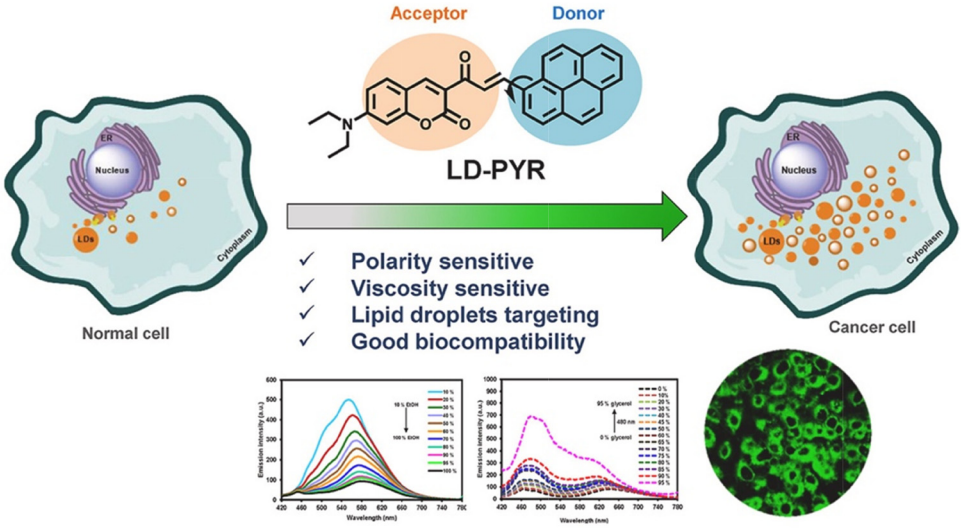

Fig. 67 The proposed working mechanism of **LD-PYR** imaging lipid droplets in cancer cells. Image reproduced with permission from ref. 329. Copyright 2023, Elsevier.

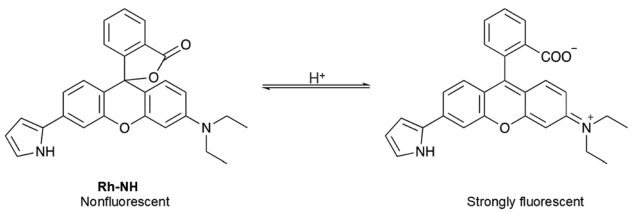

Fig. 68 The proposed mechanism of Rh-NH for the visualisation of lysosomes.

Zhao *et al.* developed a novel near-infrared fluorescent probe, **DBF-A** (Fig. 70), for the detection of intracellular cysteine (Cys).[333] The PeT process in the **DBF-A** molecule leads to its fluorescence quenching. When the acryloyl group in the **DBF-A** molecule undergoes a conjugate addition reaction with the thiol group of Cys, the fluorescent **DBF-OH** molecule is formed, and the PeT process is removed, thereby enhancing the fluorescence signal. **DBF-A** can easily penetrate cell membranes and specifically recognize intracellular Cys, making it an ideal tool for detecting intracellular Cys. Additionally, the phenolic part of the **DBF-OH** molecule can undergo a TICT process, which is inhibited by increased viscosity, thus enhancing the fluorescence intensity of **DBF-OH**. Cell experiments found that the probe exhibits good response in the nucleolus with higher viscosity, indicating its excellent nuclear membrane penetration ability and viscosity responsiveness. This probe holds promise for the detection of intracellular Cys in the nucleolus.

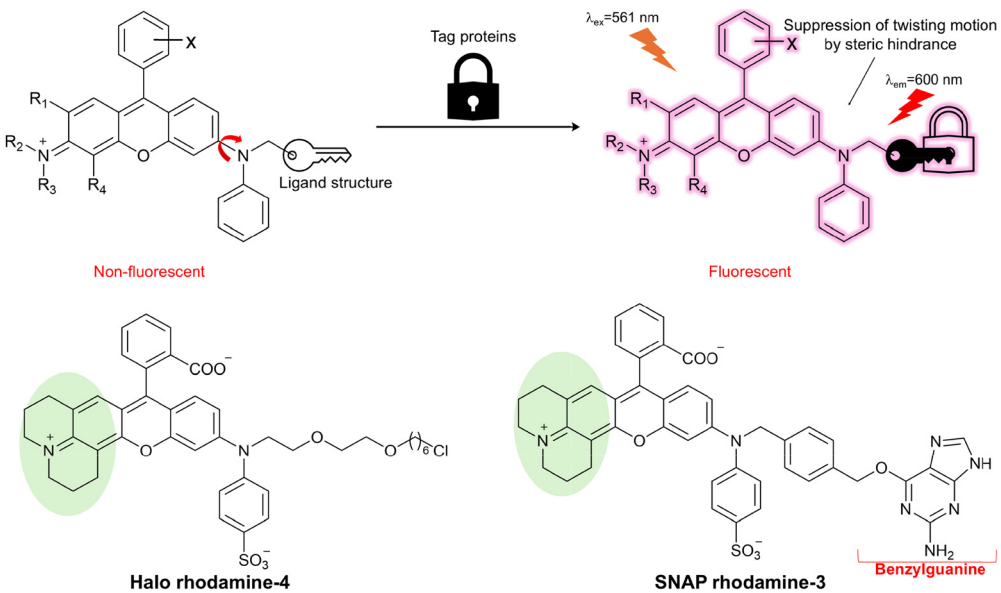

Fig. 69 The strategy for protein labelling and the chemical structures of **Halo rhodamine-4** and **SNAP rhodamine-3**.

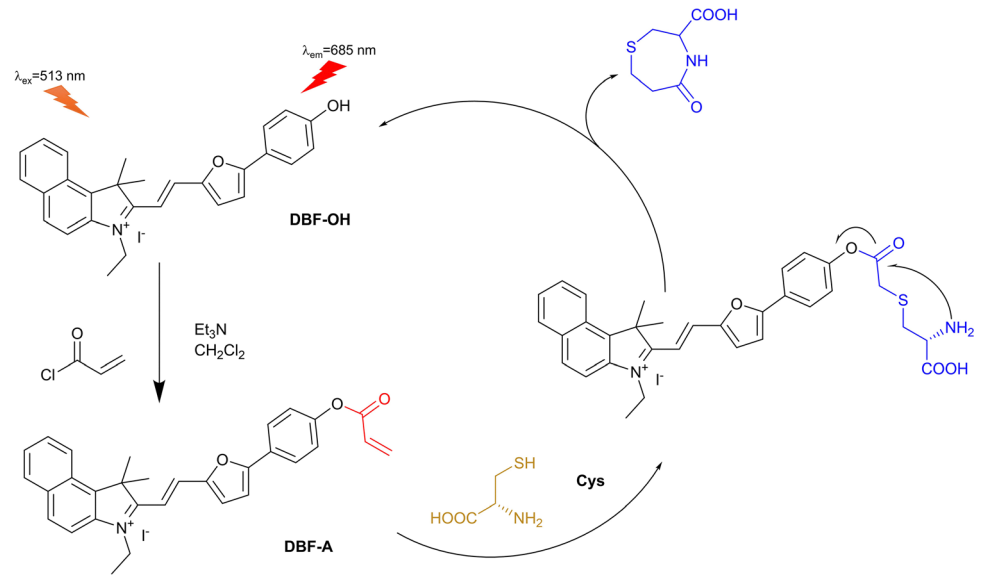

Fig. 70 The reaction between Cys and **DBF-A**, and the proposed sensing mechanism of **DBF-A**.

Li *et al.* developed a BODIPY-based two-photon fluorescent probe, **Lyso-B** (Fig. 71), for real-time monitoring of lysosomal viscosity.[334] When the probe is located outside the cell or in non-lysosomal environments, the unprotonated morpholine unit acts as an electron-rich group, which can quench the fluorescence of the BODIPY fluorophore through the PeT process. This means that the probe emits little to no fluorescence in these environments, reducing background fluorescence interference. Once the probe enters the lysosome, due to the acidic environment inside the lysosome (pH 3.8–5.5), the morpholine unit becomes protonated, transforming from an electron-rich group to an electron-withdrawing group. This transformation prevents the PeT process, thus activating the probe, allowing it to emit fluorescence within the lysosome. Furthermore, the fluorescence intensity and lifetime of the probe are influenced by the viscosity of the surrounding environment. As viscosity increases, the TICT effect weakens, leading to enhanced fluorescence intensity. Therefore, by measuring changes in fluorescence intensity and lifetime, real-time monitoring of lysosomal viscosity can be achieved. To improve the biocompatibility and water solubility of the probe while reducing cytotoxicity, two highly hydrophilic polyethylene glycol (PEG) chains were introduced into **Lyso-B**. Additionally, the connection between the morpholine ring and the BODIPY fluorophore *via* a phenylethynyl group significantly extends the conjugation, increasing the two-photon absorption (2PA) cross-section, making the probe an efficient two-photon excitation fluorescent probe. In summary, **Lyso-B** achieves high-sensitivity, high spatiotemporal resolution and real-time monitoring of lysosomal viscosity by combining TICT effects, PeT processes, and two-photon imaging technology.

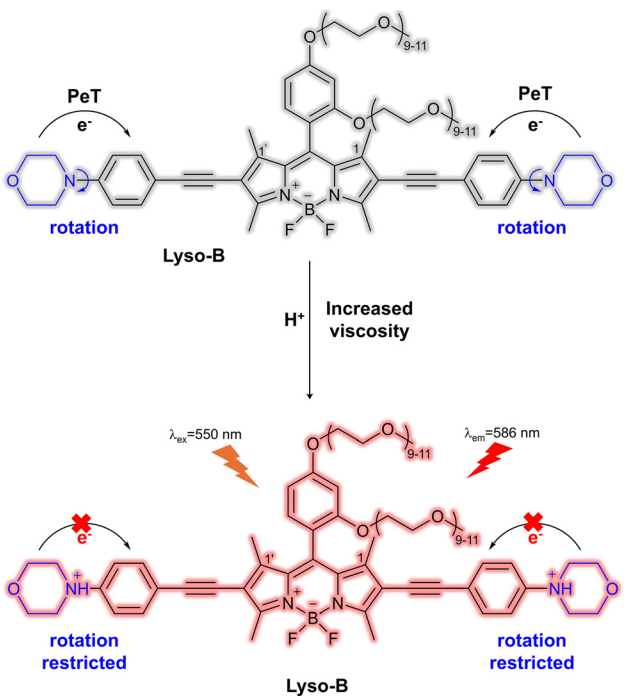

Fig. 71 The structure and working principle of lysosomal viscosity probe **Lyso-B**.

Yuan *et al.* developed a dual-sensing fluorescent probe **Vis-HClO** (Fig. 72) for high-fidelity visualization of inflammation associated with abdominal aortic aneurysm (AAA) by detecting HClO and viscosity.[335] In the absence of HClO and in a low-viscosity environment, probe **Vis-HClO** is in a fluorescence quenched state. This is due to the simultaneous presence of PeT and TICT processes, resulting in very weak fluorescence signals. When HClO is present, the *N*-methyl thiocarbamate recognition group is specifically triggered by HClO, transforming from a (benzenoid) phenol derivative into a quinoidal QCy7 dye. This transformation reduces the PeT process, partially restoring the fluorescence signal. Furthermore, in a high-viscosity environment, the rotation of the bonds to the pendent

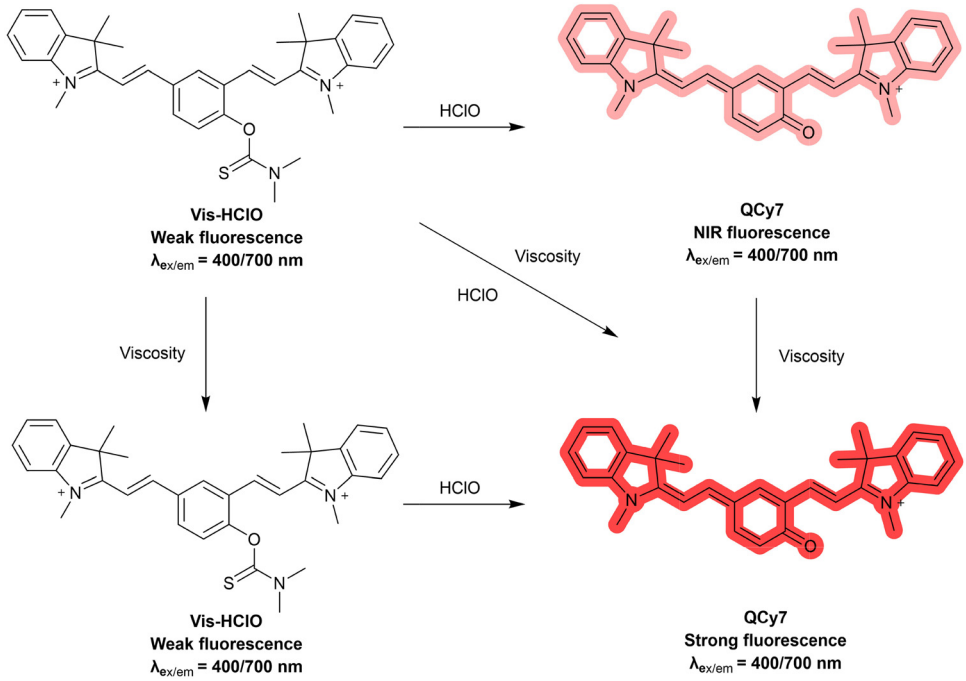

Fig. 72 The structure and response mechanism of **Vis-HClO** for HClO and viscosity.

indoline unit is inhibited, further disrupting the TICT process and releasing strong near-infrared fluorescence. **Vis-HClO** was successfully used to detect HClO in RAW 264.7 macrophages. More importantly, probe **Vis-HClO** can effectively detect HClO levels in a mouse model of abdominal aortic aneurysm through *in situ* imaging.

Han *et al.* developed a nitroreductase (NTR)-responsive probe **C2-NO$_2$** (Fig. 73) based on thio-pentamethine cyanine (TCy5) dye.[336] In the absence of specific stimuli, the nitro group (–NO$_2$) acts as an electron-withdrawing group, which can quench fluorescence through the PeT process. Additionally, the nitro substituent can also enhance the TICT effect, further quenching the fluorescence signal. **C2-NO$_2$** exhibits a low fluorescence quantum yield (Φ_f) and singlet oxygen generation efficiency (Φ_Δ^{rel}) in its initial state. Then when probe **C2-NO$_2$** is introduced to a hypoxic environment or interacts with nitroreductase (NTR), the nitro group (–NO$_2$) is reduced to an amino group (–NH$_2$), forming **C2-NH$_2$**. This structural change disrupts the PeT and TICT processes, leading to a strong fluorescence signal and singlet oxygen generation. Probe **C2-NO$_2$** exhibits clear fluorescence signals in HepG2 cells and 4T1 tumor-bearing mice, while also demonstrating good photodynamic therapeutic effects.

7.2 AIE/TICT

Aggregation-induced emission (AIE) is a scientific concept proposed by Tang *et al.* in 2001.[337] The phenomenon is characterized by fluorescent molecules with AIE properties exhibiting weak or almost no fluorescence when in solution or a dispersed state, whereas their fluorescence significantly increases in the solid state or aggregated form. AIE typically leads to fluorescent probes with high signal-to-noise ratios, high brightness, and excellent photostability. By combining AIE with the TICT mechanism, it is possible to overcome the shortcomings of individual TICT probes, achieving higher fluorescence quantum yields, better photostability, higher selectivity and sensitivity, as well as

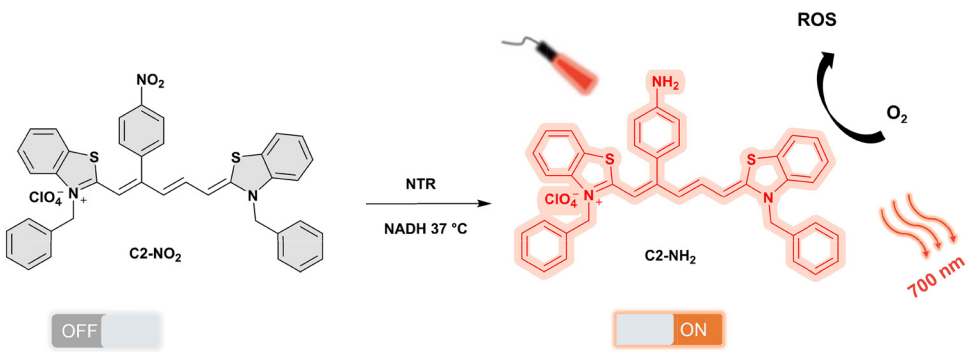

Fig. 73 Schematic illustration of the conversion of **C2-NO$_2$** to **C2-NH$_2$** in the presence of NTR.

lower background signals. This composite mechanism provides new ideas for developing high-performance fluorescent probes and photothermal materials.

The combination of AIE and TICT represents a perfect manifestation of the core concept of ''restricting molecular motion'' at different levels, where the two complement each other and even exhibit a dynamic balance of ''one waxing as the other wanes''. The essence of enhanced emission of AIEgens in the aggregated state lies in the restriction of intramolecular rotation (RIR) and vibration (RIV), which thus shuts down non-radiative decay channels. In contrast, the TICT process is strongly dependent on the intramolecular rotation of donor–acceptor units within chromophores. Therefore, the AIE effect effectively suppresses, through physical aggregation, the molecular motions that lead to TICT non-radiative decay from the outside, forcing the molecule to switch from the dark TICT state to the bright local excited (LE) state or charge transfer (CT) state, thereby achieving a significant enhancement in fluorescence quantum yield. On the other hand, strong TICT characteristics themselves help inhibit π–π stacking during aggregation, preventing fluorescence quenching caused by ACQ, and thus synergizing with the AIE effect to realize efficient solid-state emission. Researchers can skilfully utilize solvent polarity, viscosity, and aggregation degree to regulate the balance between AIE and TICT, thereby developing multifunctional probes that are highly sensitive to environmental factors.

In the TICT process, the dark TICT state formed after photoexcitation primarily returns to the ground state through non-radiative relaxation, accompanied by a red-shifted emission. Due to the active molecular rotations in this state, it is more prone to various non-radiative quenching processes. Therefore, enhanced TICT characteristics contribute to improved photothermal conversion efficiency. AIEgens are typically non-emissive in solution but become highly fluorescent in the aggregated state, which is attributed to the restriction of intramolecular motions. However, when a good solvent is added to the aggregates, the emission of AIEgens is gradually quenched due to the activation of molecular motions (*i.e.*, the reverse AIE process). This implies that by modulating intramolecular motions, the fluorescence decay of originally emissive AIEgens can be reduced, thereby enhancing photothermal conversion efficiency. Liu *et al.* combined the advantages of dark TICT and reversed AIE to develop the probe **NIRb14** (Fig. 74), aiming to stabilize the dark TICT state and restrict fluorescence decay, thereby significantly enhancing the performance of photothermal therapy (PTT) and photoacoustic imaging (PA).[21] By incorporating molecular rotors (TPA) and long alkyl chains (2-decyltetradecyl) into the planar D–A–D core, they facilitated molecular motion of the **NIRb14** probe and stabilized the dark-state TICT. The maximum emission wavelength (λ_{em}) of probe **NIRb14** in different polar solvents undergoes a red shift with the increase in solvent polarity, for instance, from toluene to dimethylformamide (DMF), the λ_{em} of **NIRb14** increases from 1030 nm to 1115 nm, accompanied by a decrease in fluorescence intensity, indicating that **NIRb14** possesses significant TICT characteristics. Enhanced TICT characteristics disrupted intermolecular interactions within the aggregated state of the **NIRb14** probe, leading to outstanding photothermal conversion capabilities. Additionally, by preparing **NIRb14** nanoparticles using poly(β-amino ester) (PAE), which responds to the acidic environment of tumors, the **NIRb14** nanoparticles can serve as nanoprobes for PA imaging-guided PTT, providing high-contrast images that helps accurately locate tumors while utilizing the PTT effect for efficient tumor treatment.

Li *et al.* developed an organic fluorescent dye **2TT-*o*C26B** (Fig. 75), whose design integrates the effects of TICT and AIE.[338] Specifically, the **2TT-*o*C26B** molecule employs a strong electron-withdrawing unit, benzobisthiadiazole (BBTD), as the acceptor, triphenylamine (TPA) as both the donor and molecular rotor, and an alkylated thiophene as the connecting unit, ensuring significant twisting of the conjugated main chain. The combination of the of twisted molecular structure and donor twist favor the coexistence of TICT and AIE effects in probe **2TT-*o*C26B**, thereby simultaneously achieving long-wavelength emission and high-intensity emission. The maximum emission wavelength of **2TT-*o*C26B** is approximately 1030 nm, with a quantum yield (QY) as high as 11.5%. When **2TT-*o*C26B** is formulated into nanoparticles with DSPE-PEG-2000, it exhibits good dispersion and stability in aqueous solutions. The **2TT-*o*C26B** nanoparticles (NPs) display strong fluorescence emission in the near-infrared IIb region, with the quantum yield reaching 0.12% in the 1500–1600 nm range. Using these properties, successful fluorescence imaging of deep tissues such as blood vessels and the intestine in living mice was achieved. More importantly, after oral administration for 24 hours, **2TT-*o*C26B** NPs are completely excreted from the

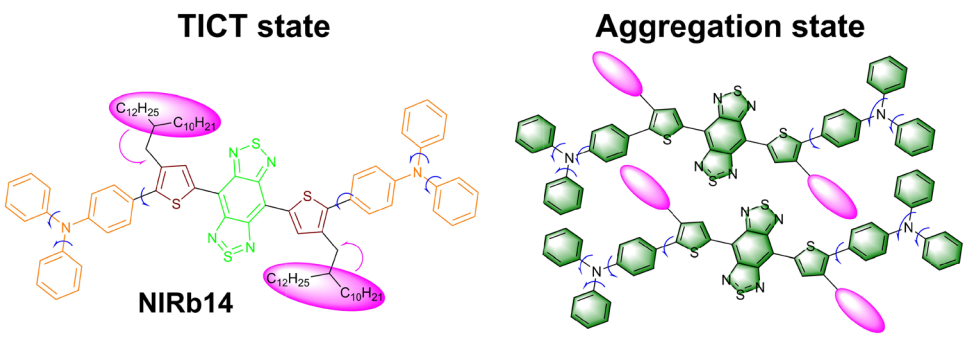

Fig. 74 Schematic illustration of the TICT state and aggregation state of the **NIRb14**. Image reproduced with permission from ref. 21. Copyright 2019, American Chemical Society.

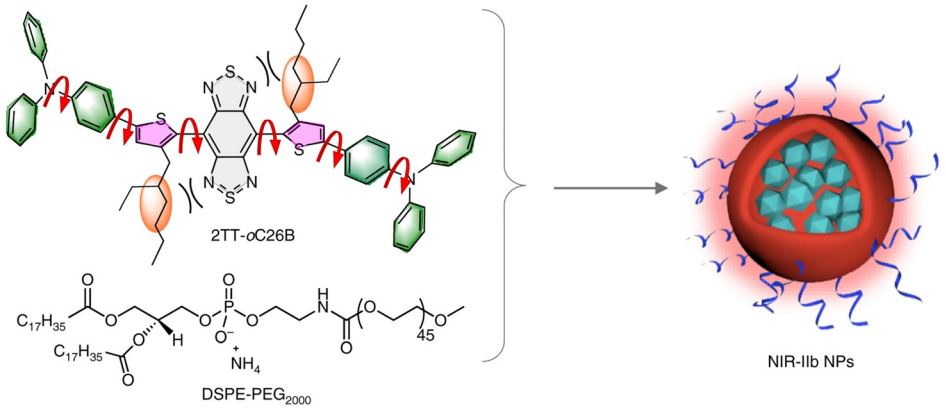

Fig. 75 Schematic illustration of **2TT-*o*C26B** NPs. Image reproduced with permission from ref. 338. Copyright 2020, Springer Nature.

body in the feces, demonstrating excellent biocompatibility and potential as an oral gastrointestinal diagnostic contrast agent.

Meng *et al.* developed a near-infrared (NIR) fluorescent probe, **TBB** (Fig. 76), based on TICT and AIE.[27] Its molecular structure features a rotatable donor–π–acceptor (D–π–A) framework, where the donor part is a triphenylamine group, the acceptor part is a biphenyl-substituted fumaronitrile unit, and they are connected by a conjugated styryl motif. This structural design allows for effective charge transfer processes within the molecule, leading to near-infrared emission. Additionally, **TBB** exhibits significant fluorescence enhancement upon aggregation due to restricted intermolecular interactions that reduce non-radiative decay pathways. In solvents of varying polarity, the fluorescence emission wavelength of **TBB** gradually increases from 580 nm to 784 nm with the increase of solvent polarity, while the absorption peak remains essentially unchanged at 365 nm. **TBB** exhibits temperature-sensitive properties, with its fluorescence intensity and lifetime gradually decreasing as the temperature rises. To construct a ratiometric fluorescent thermometer, **TBB** and **R110** were encapsulated in an amphiphilic polymer **F127** to form **TRF NPs**. **R110** serves as a reference dye, providing a stable fluorescence signal for calibrating the ratiometric fluorescent thermometer. **TRF NPs** exhibit good temperature response characteristics over the range of 25 °C to 65 °C, with a relative sensitivity of 2.37% $°C^{-1}$. Furthermore, **TRF NPs** can effectively monitor the temperature changes in HepG2 cells during photothermal therapy, from 25 °C to 53 °C, demonstrating their potential applicability for intracellular temperature sensing.

Lai *et al.* designed and developed a fluorescent probe **ANB** (Fig. 77), for turn-on imaging of lipid droplets (LDs) in cancer cells.[339] Its molecular structure includes naphthalimide and *para*-aminostyryl moieties. In nonpolar environments, such as inside LDs, **ANB** predominantly exhibits a LE state, emitting higher-energy blue-shifted fluorescence (green, ~560 nm in toluene). In polar solvents, however, **ANB** tends to form a TICT state, emitting lower-energy red-shifted fluorescence (red, ~670 nm in water). When **ANB** aggregates extensively within LDs, intermolecular interactions reduce rotational freedom, thus inhibiting non-radiative transition pathways, and significantly increase the fluorescence intensity. Moreover, **ANB** exhibits photochromic properties; when in the LE state, photoinduced protonation of **ANB** further enhances its fluorescence intensity, forming so-called PIEE-LDs (photoinduced emission enhancement lipid

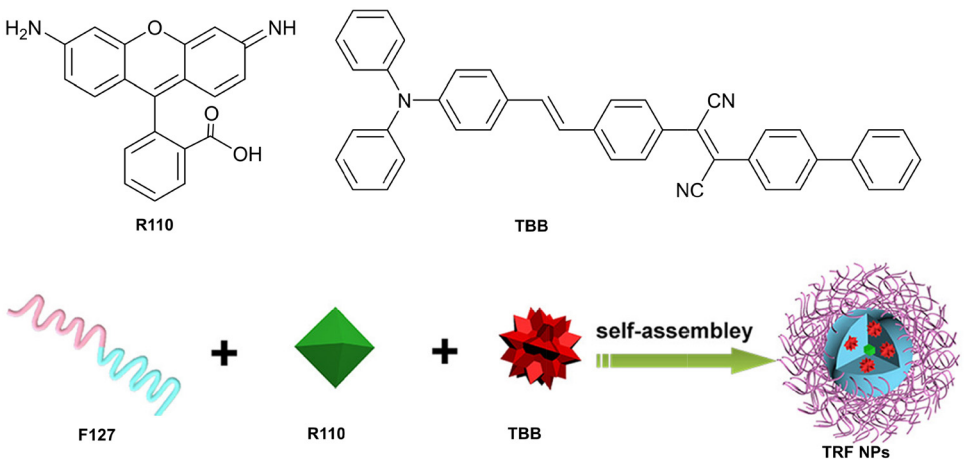

Fig. 76 Chemical structures of **TBB** and **R110**, and schematic of the fabrication of the **TRF NPs**. Image reproduced with permission from ref. 27. Copyright 2020, American Chemical Society.

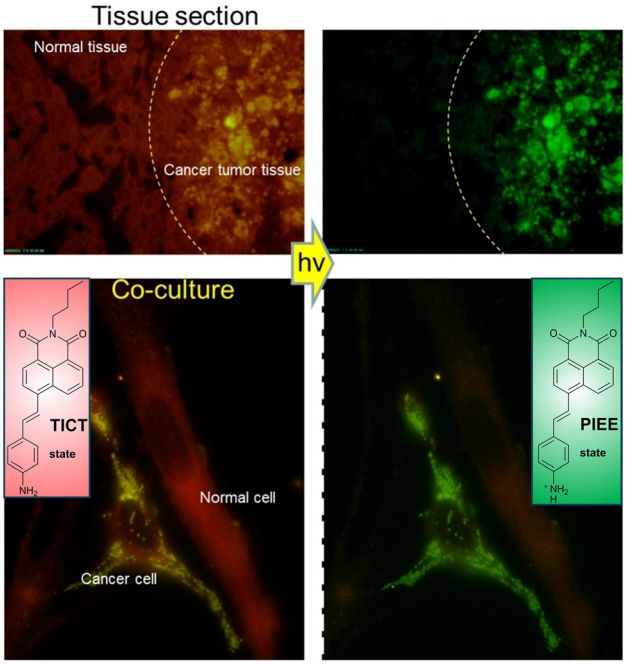

Fig. 77 Diagnosis of tumor tissue based on PIEE of **ANB**. Image reproduced with permission from ref. 339. Copyright 2021, Elsevier.

droplets). **ANB** can specifically localize and accumulate in LDs, allowing for prolonged fluorescence imaging and clear observation of the fusion process of LDs. Since cancer cells typically have more LDs than normal cells, the high selectivity and high contrast imaging capability of **ANB** for LDs can be used to distinguish tumor tissues from normal tissues.

Zeng *et al.* designed and developed a novel fluorescent probe, **BETA-1** (Fig. 78), based on both TICT and AIE mechanisms, achieving simultaneous dual-color imaging of LDs and mitochondria to study the dynamic interactions between these two organelles in living cells and organisms.[340] Where **BETA-1**, the *N*-methyl benzothiazolium acts as an electron acceptor with a cationic structure for targeting mitochondria, while triphenylamine serves as an electron donor, and as a lipophilic group, for targeting lipid droplets. Additionally, to improve the probe's lipophilicity, a highly lipophilic (neutral) benzothiazole moiety was introduced. In a high water fraction environment, **BETA-1** exhibits bright red light emission (680 nm) due to restricted intramolecular motion caused by molecular aggregation, which is attributed to the AIE effect; whereas in solvents of varying polarity, with an increase of solvent polarity, the emission peak of **BETA-1** shifts from 485 nm (in low-polarity toluene) to 540 nm (in high-polarity methanol (MeOH), acetonitrile (MeCN), and dimethyl sulfoxide (DMSO)), which is caused by the TICT effect. In LDs, due to their lipophilic environment, **BETA-1** exhibits cyan fluorescence emission ($\lambda_{ex}/\lambda_{em}$ = 405/430–500 nm); whereas in mitochondria, due to its positively charged structure, **BETA-1** can specifically accumulate in mitochondria and emits red fluorescence ($\lambda_{ex}/\lambda_{em}$ = 561/600–700 nm). **BETA-1** has been successfully used to record the continuous dynamic processes and long-term dynamic interactions of LDs and mitochondria. Furthermore, **BETA-1** has been used to investigate the interactions between LDs and mitochondria during ferroptosis and has been successfully applied for *in vivo* imaging of LDs and mitochondrial interactions in *C. elegans*.

Miao *et al.* designed and developed a fluorescent probe, **MP-NAP** (Fig. 79), based on a naphthalimide scaffold and modified with *N*-methylpyrrole (MP).[341] The fluorescence mechanism of **MP-NAP** is mainly based on TICT. In polar solvents, the charge transfer promotes the twisting of *N*-methylpyrrole relative to the naphthalimide scaffold, forming TICT state in the excited state, leading to fluorescence quenching *via* non-radiative transitions. In nonpolar solvents, however, the TICT effect is suppressed, the molecule maintains a planar structure, and thus exhibits strong fluorescence at 530 nm. **MP-NAP** also exhibits significant AIE characteristics. In solution, as the water ratio increases, **MP-NAP** begins to form molecular aggregates, significantly enhancing the fluorescence intensity at 530 nm. This is because molecular aggregation reduces local polarity and hinders TICT rotation, thereby restoring the fluorescence. **MP-NAP** can be used to image LDs in live cells, is capable of achieving bright fluorescence imaging without washing steps, and exhibits a higher signal-to-noise ratio compared to commercial Nile Red.

Based on the TICT and AIE mechanism, Wang *et al.* designed a fluorescent probe, **TICT-lipid** (Fig. 80), by introducing long alkyl chains and positively charged head groups.[342] With an increase of solvent polarity, the emission maximum of **TICT-lipid** shifts from 522 nm in low polarity solvents to 634 nm in high polarity solvents, indicating a significant TICT effect. The AIE properties of **TICT-lipid** were evaluated using DMSO–water mixtures with different water fractions (f_w). As the f_w increased from 0% to 40%, the fluorescence intensity of **TICT-lipid** significantly decreased along with a notable blue shift; however, as f_w increased from 40% to 90%, there was a remarkable enhancement in fluorescence intensity, which is a typical AIE characteristic. By mixing two solvents with similar polarity but different viscosities (ethylene glycol and glycerol), it was observed that the fluorescence intensity of **TICT-lipid** gradually increased as the glycerol fraction (f_g) rose from 0% to 100%, demonstrating that AIE is activated in highly viscous environments due to restricted intramolecular motions. **TICT-lipid** can insert into bacterial membranes, exhibiting high sensitivity to the degree of lipid packing and changes in environmental polarity. **TICT-lipid** has been successfully applied for detecting the degree of lipid packing in bacterial membranes, studying the action mechanisms of membrane-disrupting antibiotics, and bacterial membrane processes.

Sun *et al.* developed a fluorescent probe, **TBTNO$_2$** (Fig. 80), based on a TPE scaffold and thiazole derivative.[343] Its unique molecular structure allows it to exhibit significant solvatochromic effects and large Stokes shifts in solvents of different polarities. In pure tetrahydrofuran (THF), **TBTNO$_2$** exhibits pink fluorescence emission at 586 nm. As water, a poor solvent, is gradually added to the THF solution, the emission intensity of **TBTNO$_2$** significantly decreases and the emission wavelength red-shifts when the water content ranges from 0% to 5%. This phenomenon is attributed to the increased solvent polarity and

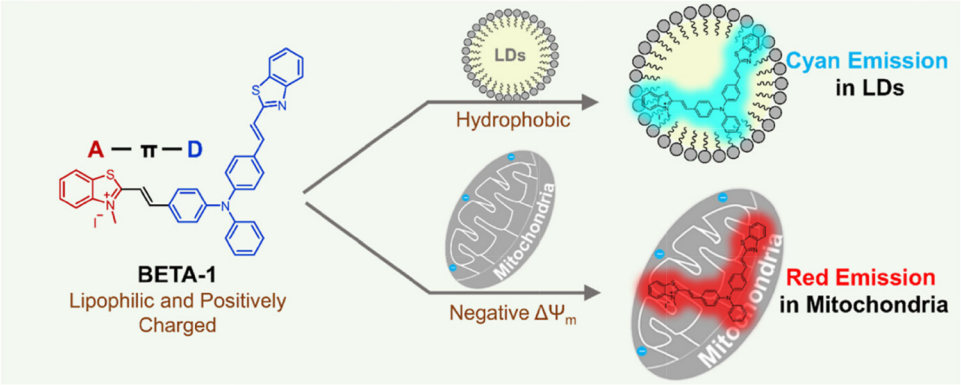

Fig. 78 Chemical structure of probe **BETA-1** and the schematic illustration of dual-color visualization of lipid droplets (LDs) and mitochondria using **BETA-1**. Image reproduced with permission from ref. 340. Copyright 2022, American Chemical Society.

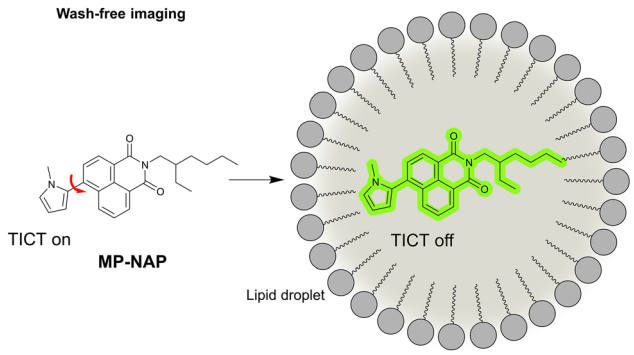

Fig. 79 Chemical structure and Schematic illustration of probe **MP-NAP** for the wash-free bioimaging of LDs.

strong intramolecular charge transfer (ICT), where intense solvent relaxation in the excited state leads to free rotation of phenyl rings around single bonds, facilitating the transition from ICT to TICT. Between water contents of 10% and 70%, the fluorescence emission of **TBTNO$_2$** is almost quenched due to the enhanced TICT process. Upon further increasing the water fraction to approximately 80%, the fluorescence intensity begins to increase again, indicating that molecules are gradually aggregating. Subsequently, as the water fraction increases up to 95%, the emission of **TBTNO$_2$** sharply rises. **TBTNO$_2$** exhibits high sensitivity and reliability for detecting trace amounts of water in organic solvents, making it suitable for monitoring the drying process of organic solvents and quantitative water analysis.

Lee *et al.* developed a fluorescent probe, **DDB** (Fig. 80), which possesses TICT and AIE characteristics, based on a diethylamino donor group and a barbiturate acceptor group, for the staining of microplastics.[344] Its unique molecular structure enables it to exhibit significant solvatochromic effects and large Stokes shifts in solvents of different polarities. In weakly polar solvents, the LE state emission of **DDB** is primarily observed at around 550 nm, whereas in strongly polar deionized water, a higher intensity TICT state emission appears near 700 nm. **DDB** has been successfully used for microplastic detection in soil and river water samples, making it valuable for environmental monitoring and research on microplastic pollution.

Gao *et al.* developed novel AIE photosensitizers, **TBBCyP** and **TBTCyP** (Fig. 80), based on the TICT and AIE mechanisms, featuring a D–A–π–A structure.[345] When the fraction of toluene is below 90% (f_T < 90%), both probes exhibit relatively weak fluorescence. However, once the fraction of toluene exceeds 90%, due to their poor solubility in toluene, **TBBCyP** and **TBTCyP** emit intense orange and red fluorescence at approximately 605 nm and 646 nm, respectively, which is indicative of a typical AIE characteristic. Additionally, the quantum yields of **TBBCyP** and **TBTCyP** in a DMSO/toluene mixture (v/v, 1 : 99) were determined to be 32.3% and 13.2%, respectively, demonstrating that **TBBCyP** exhibits a weaker TICT effect. In contrast, **TBTCyP** shows a more pronounced solvent effect and a stronger TICT effect, leading to lower fluorescence efficiency. **TBBCyP** and **TBTCyP** not only possess excellent AIE properties and biocompatibility but can also efficiently generate singlet oxygen, achieving mitochondria-targeted PDT.

Chen *et al.* developed a new multifunctional theranostic agent, **MBPN-T-BTD** (Fig. 80), based on methoxy-functionalized naphthalene-substituted triphenylamine, thiophene, and benzothiadiazole.[32] In pure THF solution, **MBPN-T-BTD** exhibits an emission range of 850–1400 nm with a maximum emission peak at 1045 nm. As the water content in the THF/water mixed solutions increases, the maximum emission peak of **MBPN-T-BTD** undergoes a red shift, and the fluorescence intensity significantly decreases until the water content reaches 40%, which is attributed to the emergence of the TICT effect due to the increased solvent polarity. When the water content further increases to 90%, the fluorescence intensity gradually recovers, which is due to the formation of aggregates that trigger a mechanism restricting intramolecular motion. **MBPN-T-BTD** not only exhibits AIE characteristics but also effectively exhibits TICT, thus ensuring excellent near-infrared fluorescence performance and photothermal conversion ability, enabling the treatment and diagnosis of oral cancer.

Wang *et al.* developed a near-infrared fluorescent probe named **DPX** (Fig. 80), designed to detect viscosity changes within biological systems.[346] The probe consists of a benzopyran linked to triphenylamine (TPA) *via* an alkene, forming a push–pull electronic system (D–π–A structure). **DPX** exhibits

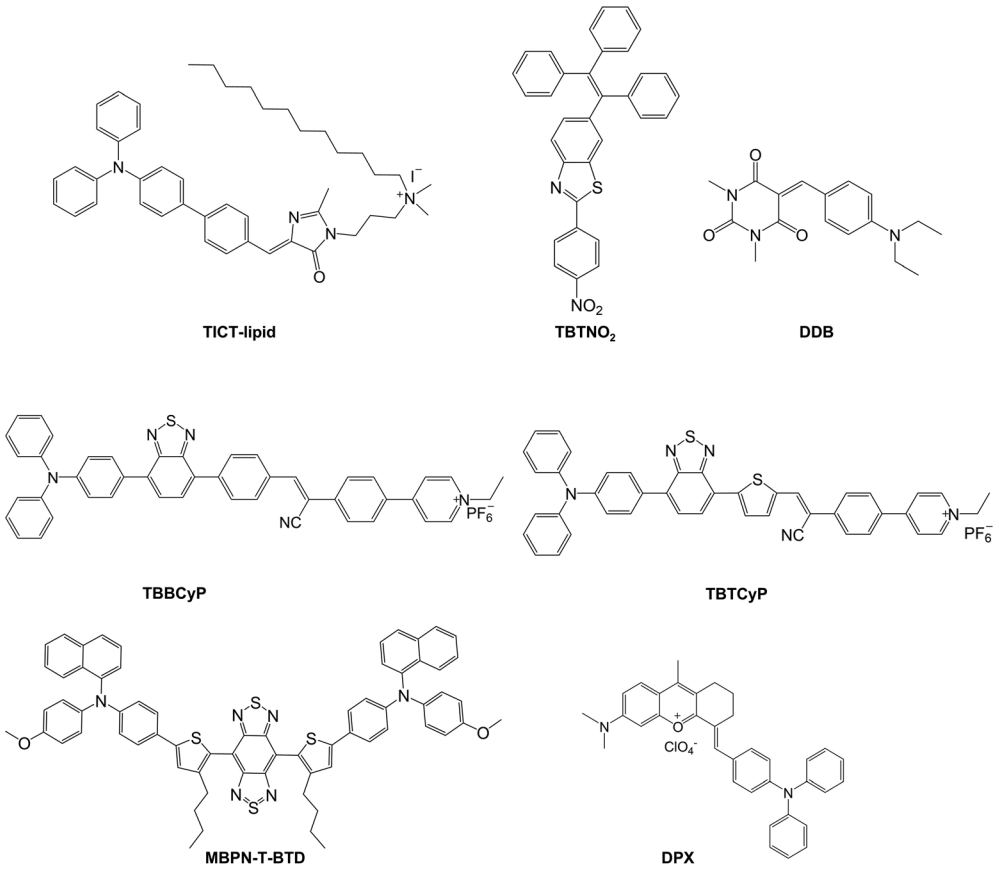

Fig. 80 Chemical structures of probe **TICT-lipid**, **TBTNO$_2$**, **DDB**, **TBBCyP**, **TBTCyP**, **MBPN-T-BTD** and **DPX**.

excellent AIE properties and TICT effects. Under excitation at 620 nm, the fluorescence of **DPX** in pure DMSO is weak (Φ = 0.14%), but it significantly enhances at 740 nm as the proportion of toluene increases. Moreover, **DPX** is more sensitive to viscosity than to polarity, especially in a PBS–glycerol mixed solvent system, where the fluorescence intensity at 725 nm gradually increases by about 140-fold as the solvent viscosity increases from 0.89 cP (0% glycerol) to 945 cP (99% glycerol). It can be used to detect viscosity changes in biological systems, and to visualize viscosity changes in liver damage caused by diabetes.

7.3 TICT/ESIPT

The combination of TICT and ESIPT creates a complex system with multiple excited-state relaxation pathways, significantly expanding the photophysical behaviour of fluorescent probes. The ESIPT process typically generates a large Stokes shift, effectively avoiding self-absorption and interference from the excitation light. In contrast, the TICT process is highly sensitive to environmental polarity. The interaction between these two mechanisms can be manifested as follows: (1) competition: a polar environment may simultaneously stabilize the TICT state and promote the formation of the keto form *via* ESIPT; these two processes compete for excited-state energy, resulting in ratiometric fluorescence changes. (2) Synergy: the occurrence of one process can create conditions for the other. For instance, the keto form formed after ESIPT may possess stronger electron-donating or accepting ability, thereby significantly altering the degree of intramolecular charge transfer and enhancing or weakening the TICT effect. (3) Sequential occurrence: After excitation, a molecule may first undergo ESIPT (proton transfer), followed by TICT (charge transfer and rotation), ultimately forming a hybrid excited state with unique fluorescence properties. Through precise design of molecular structures, the sequence and efficiency of these two processes can be regulated, enabling highly selective and high-contrast detection of specific analytes.

Liu *et al.* studied a fluorescent probe **H$_2$L** (Fig. 81), enabling the detection of aluminum ions (Al^{3+}) and zinc ions (Zn^{2+}).[347] The probe H_2L was first reported by Das *et al.*, but these authors did not invoke TICT in their proposed explanation of **H$_2$L**'s fluorescence response.[348] However, the later computational work of Liu *et al.* suggests that a photo-induced electron transfer (PeT) process upon irradiation of **H$_2$L** leads to a TICT state, whose existence leads to the fluorescence quenching of the probe. That is, under photoexcitation, the electrons in **H$_2$L** transition to form a twisted molecular conformation, so that the molecule exists in a TICT state, from which non-radiative relaxation occurs. In the absence of metal binding, this TICT state remains accessible, resulting in fluorescence quenching. However, upon chelation with Al^{3+} or Zn^{2+}, the metal ions form coordinate bonds with O/N atoms of **H$_2$L**, which rigidifies the conformation and inhibits

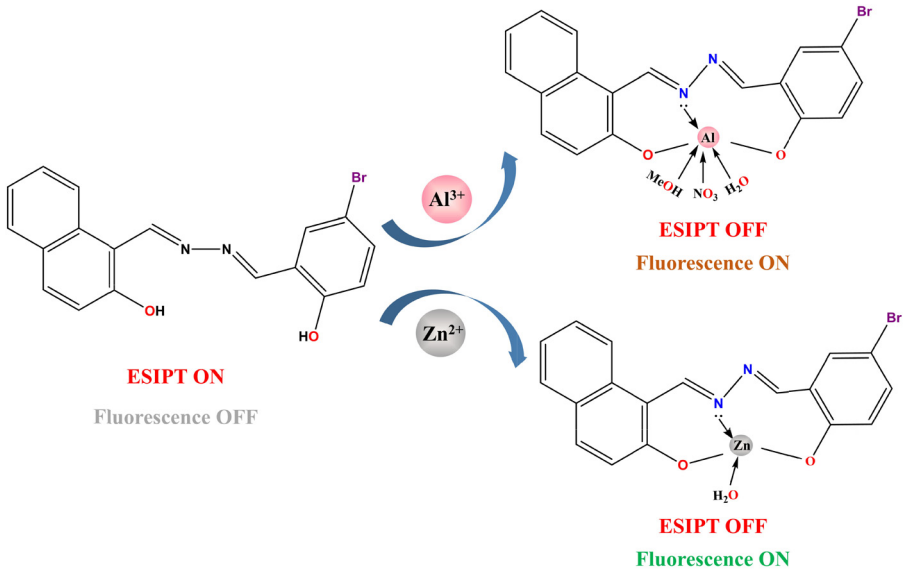

Fig. 81 The structure and response mechanism of H_2L for Al^{3+} and Zn^{2+}as proposed by the original authors.

TICT, thereby restoring the fluorescence signal. This "TICT-quenching → metal-induced TICT inhibition → fluorescence recovery" logic is critical for selective detection. Meanwhile, the ESIPT process can be operative for H_2L's unbound state, but would be removed upon metal coordination, as the –OH proton in question is not present in the metal complex. The ESIPT process is reportedly also influenced by solvent polarity, with high-polarity solvents promoting proton transfer. By adjusting the solvent polarity, selective detection of Al^{3+} and Zn^{2+} can be achieved. Specifically, a medium-polarity methanol–water mixture is selective for detecting Al^{3+}, whereas a high-polarity DMSO–water mixture is more selective for detecting Zn^{2+}.

7.4 AIE/ESIPT/TICT

The integration of AIE, ESIPT, and TICT into a single molecule represents a revolutionary design concept enabling the delivery of peak optical performance. This strategy combines their respective advantages: AIE ensures high luminescence efficiency in the aggregated state; ESIPT provides a large Stokes shift; and TICT endows responsiveness to environmental polarity and viscosity. The interactions among the three are highly intricate: the restriction of molecular motion by AIE serves as a prerequisite for activating ESIPT and suppressing non-radiative transitions of TICT. Moreover, the significant molecular structural rearrangement (enol–keto tautomerism) induced by ESIPT strongly influences the efficiency and direction of intramolecular charge transfer, thereby modulating the TICT process. This multi-mechanistic synergistic design can overcome the limitations of single- or dual-mechanism based probes, yielding powerful tools with ultra-high sensitivity, ratiometric signal output, that are adaptive to diverse environments. However, it also imposes higher demands for precise molecular design and synthesis.

Chen *et al.* developed a Schiff base containing probe **8** (Fig. 82), which incorporates a salicylaldehyde-derived α-cyanostilbene and benzophenone hydrazone.[349] Probe **8** exhibits red fluorescence in THF/H_2O mixed solutions and in the solid state. Specifically, probe **8** primarily emits at a wavelength of 434 nm, with a secondary emission wavelength around 650 nm, and is capable of providing bright red light emission in the solid state. This is attributed to the synergistic effects of AIE, ESIPT, and TICT. Probe **8** exhibits high selectivity and sensitivity towards Fe^{3+}, with a detection limit of 5.50×10^{-8} M and a binding constant of 1.69×10^5 M^{-1}. In real water samples, the detection results using probe **8** were satisfactory, with recovery rates ranging from 96–103% and standard deviations between 2.6–3.2%.

Pramanik *et al.* developed a fluorescent probe **HL** (Fig. 83), which was synthesized by the condensation of 2,6-diformyl-4-ethylphenol and *o*-anisidine at a ratio of 1:2.[350] **HL** exhibits several photophysical properties, including acting as a selective

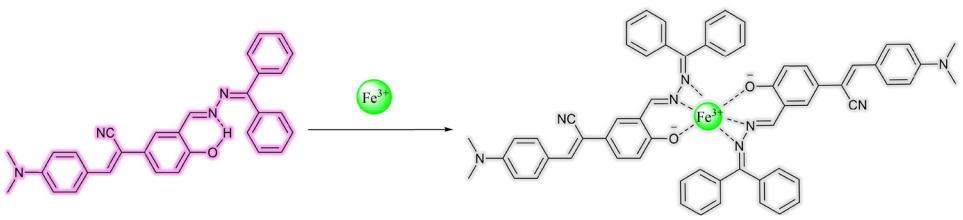

Fig. 82 The structure and possible response mechanism of probe **8** for Fe^{3+}.

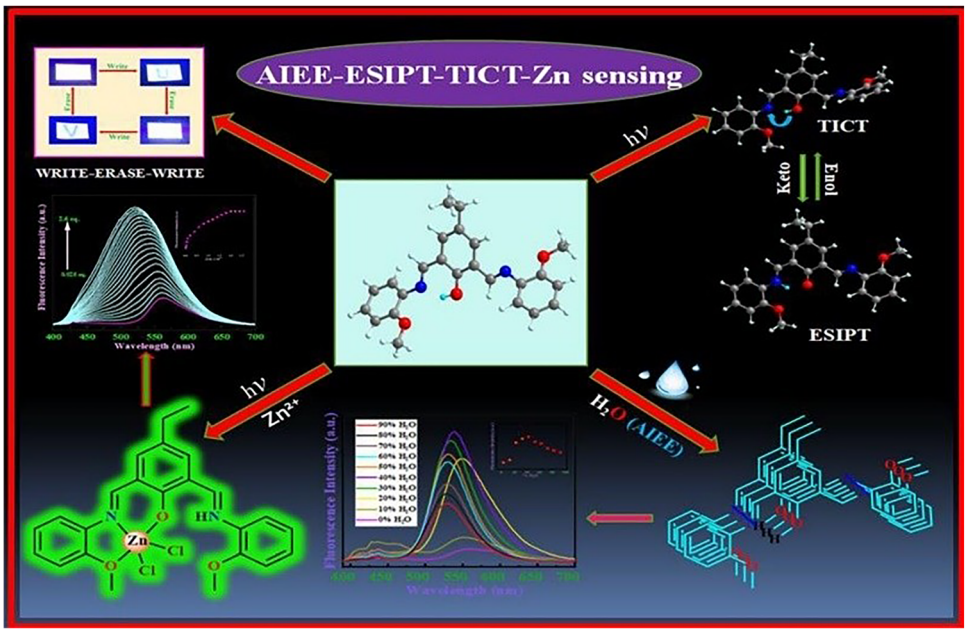

Fig. 83 The chemical structure of **HL**, its response mechanism to Zn^{2+}, and its AIEE, ESIPT, TICT properties. Image reproduced with permission from ref. 350. Copyright 2024, Elsevier.

"turn-on" fluorescent sensor for zinc ions (Zn^{2+}), aggregation-induced emission enhancement (AIEE), excited-state intramolecular proton transfer (ESIPT), and twisted intramolecular charge transfer (TICT). The unique properties of **HL** enable its application in inkless writing technology. Specifically, **HL** can achieve "write–erase–rewrite" functionality due to its reversible fluorescence changes under different conditions. Additionally, **HL** exhibited high selectivity and sensitivity towards zinc ions, making it useful as a fluorescent sensor for detecting Zn^{2+} in environmental or biological samples. The results of the fluorescence response at 521 nm showed that the detection of Zn^{2+} could be completed within 5 s.

Zhong *et al.* developed a fluorescent probe **HTQ-R** (Fig. 84) for visualizing hydrogen peroxide (H_2O_2) in rheumatoid

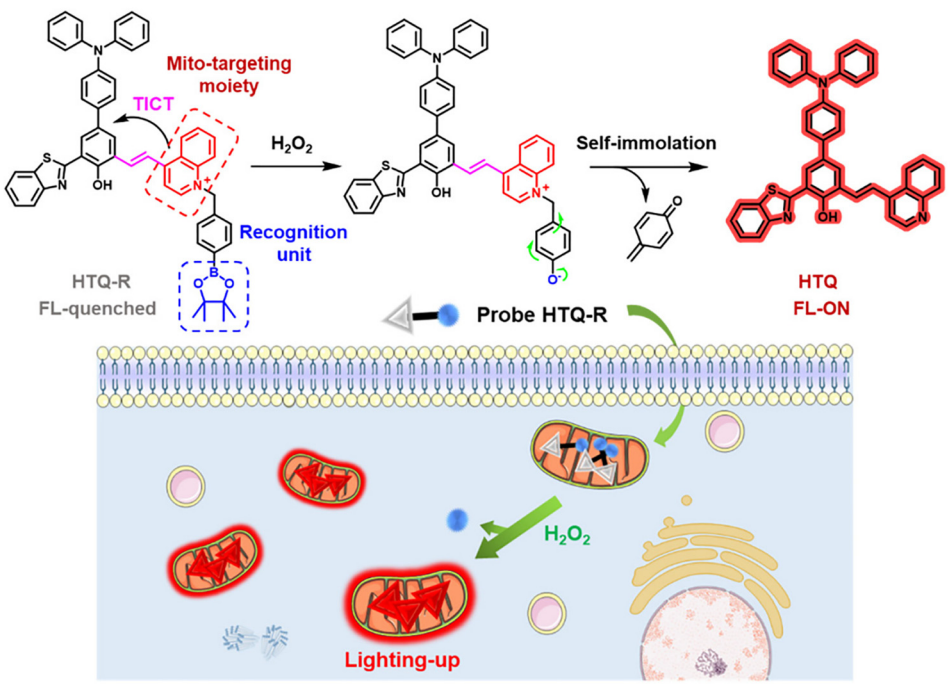

Fig. 84 Chemical structure and mechanistic illustration of responses of the red-emissive AIE probe **HTQ-R** to H_2O_2 specifically in mitochondria. Image reproduced with permission from ref. 351. Copyright 2023, The Royal Society of Chemistry.

arthritis (RA) mice.[351] **HTQ-R** is an aggregation-induced emission (AIE) probe based on the excited-state intramolecular proton transfer (ESIPT) effect. Its molecular structure features a quinolinium salt as the core, with a phenylboronic acid pinacol ester introduced as the recognition site for H_2O_2. This molecular design causes **HTQ-R** to be in a fluorescence quenched state initially due to the TICT effect. When **HTQ-R** is exposed to H_2O_2, the electrophilic boron atom in the phenylboronic acid pinacol ester is attacked by H_2O_2, forming a tetrahedral borate. Subsequently, the aryl group migrates from the boron atom to the adjacent oxygen atom, forming a borate ester. Next, under physiological conditions, the borate ester spontaneously hydrolyzes to generate a phenolic intermediate and boric acid/ester. Finally, through a 1,6-elimination reaction, the C–N bond breaks, completing the linker self-immolation process and releasing the fluorophore **HTQ**. The released **HTQ** contains an *ortho*-hydroxyphenyl group (proton donor) and a benzothiazole nitrogen atom (proton acceptor), enabling ESIPT: upon photoexcitation, a proton transfers from the hydroxyl to the nitrogen in the excited state. This linker cleavage process significantly reduces the electron-withdrawing ability of the quinolinium salt (by transforming it into a less electron-withdrawing neutral quinoline), thereby preventing the TICT process and restoring fluorescence emission at 620 nm. Notably, ESIPT is also responsible for **HTQ-R**'s large Stokes shift (220 nm), as the enol-to-keto tautomerisation in ESIPT widens the gap between excitation and emission wavelengths. Additionally, this large Stokes shift (220 nm) can reduce self-absorption and interference from autofluorescence. The triphenylamine motif in **HTQ-R** was incorporated into the probe design to confer AIE properties (after linker cleavage), and as expected the fluorophore **HTQ** exhibited fluorescence enhancement in solvent mixtures having greater proportions of water, confirming the AIE behaviour. The cationic structure of the quinolinium salt enables **HTQ-R** to accurately target mitochondria. **HTQ-R** was used to detect exogenous and endogenous H_2O_2 in live cells, achieving real-time monitoring of H_2O_2. Furthermore, **HTQ-R** exhibited a significant increase in fluorescence intensity in a dose-dependent manner in a rheumatoid arthritis (RA) mouse model.[351]

7.5 FRET/TICT

The integration of FRET and TICT constitutes an ingenious "division-of-labor and collaborative" strategy, providing a powerful platform for constructing high-performance NIR-II fluorescent probes. In this strategy, FRET, as an efficient intermolecular energy transfer mechanism, is responsible for the precise energy transfer from the donor to the acceptor, with its efficiency depending on spectral overlap and molecular distance. The core role of the TICT mechanism is the provision of dye molecules with strong TICT characteristics, since such molecules typically exhibit significantly red-shifted emission spectra and they can endow the acceptor chromophore with intrinsic NIR-II emission capability, providing the necessary foundation for NIR-II imaging. In such designs, the TICT process is not always engineered to respond to stimuli; instead, its inherent intramolecular rotational properties are utilized to regulate the competitiveness of non-radiative transition channels. Through molecular engineering strategies (*e.g.*, tuning the electron-donating/accepting push–pull abilities of donor–acceptor pairs or molecular conformations), the rates of radiative and non-radiative transitions can be finely balanced, thereby maintaining the measurable fluorescence of the dye while achieving sufficient intensity of NIR-II tail emission. The FRET process further converges energy onto these optimized TICT-type acceptors, significantly enhancing their fluorescence signals in the NIR-II region and realizing effective signal amplification. This strategy of using FRET can synergistically enhance the fluorescence of TICT-type chromophores with intrinsic NIR-II emission capability and represents one of the key approaches for developing high-brightness and high-stability NIR-II imaging probes.

Xia *et al.* developed a second near-infrared window (NIR-II) fluorescent probe **P-Dye-Nd-2** (Fig. 85).[352] This probe synergistically enhances NIR-II emission through the combination of twisted intramolecular charge transfer (TICT) and Förster resonance energy transfer (FRET), enabling efficient and stable NIR-II fluorescence imaging. **P-Dye-Nd-2** is a brush copolymer synthesized from poly(ethylene glycol)methacrylate (PEGMA) and a monomer containing a first near-infrared window (NIR-I) dye, IR-808, known as MA-IR-808. Following this, the copolymer is complexed with a neodymium chelator (Nd-DTPA) at a ratio of 16 : 1 to form the final probe structure. In aqueous solution, **P-Dye-Nd-2** spontaneously assembles into nanoparticles, where the π-conjugated backbone of the IR-808 molecules is encapsulated within the hydrophobic core, while the sulfonate groups are exposed to water. This arrangement promotes the twisted conformation of IR-808 molecules, enhancing the TICT process. Additionally, energy transfer between Nd-DTPA and IR-808 *via*

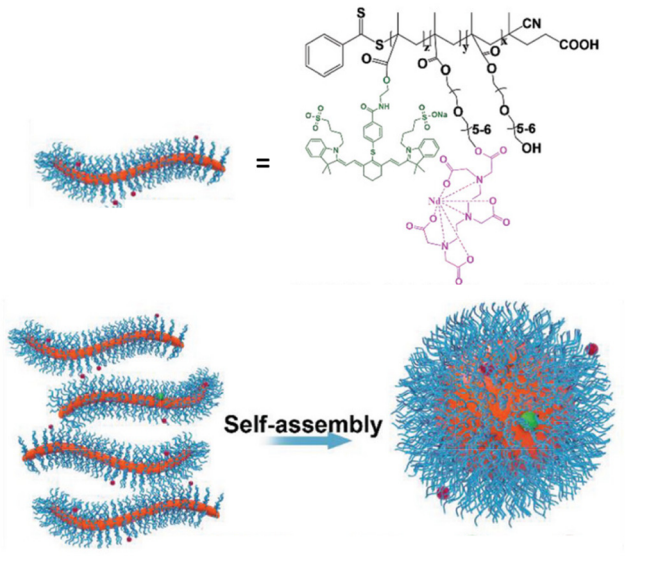

Fig. 85 Chemical structure and schematic illustration of self-assembly process of **P-Dye-Nd-2**. Image reproduced with permission from ref. 352. Copyright 2024, Wiley.

FRET further amplifies emission in the NIR-II region. In this FRET process, Nd-DTPA acts as the donor and IR-808 as the acceptor. Their close proximity (<10 nm) in the nanoparticles and the overlap between Nd-DTPA's emission and IR-808's absorption enable efficient energy transfer, further amplifying NIR-II emission by providing additional excitation energy to IR-808. **P-Dye-Nd-2** was used for dynamic angiography in immunodeficient nude mice, exhibiting significantly enhanced brightness and high spatial resolution. It was also applied for imaging a middle cerebral artery occlusion (MCAO) mouse model, clearly distinguishing the blood perfusion of the normal and ischemic sides of the brain. In a mouse model of acute kidney injury (AKI), **P-Dye-Nd-2** exhibited prolonged retention in damaged kidneys, which could aid in guiding surgery and predicting the progression of kidney disease.

8. Continuous/logic/dual/multiple-responsive TICT-based probes

Most small-molecule sensors used in biological systems are designed to detect a single analyte. This focus provides powerful tools for studying the role of individual species and has achieved significant results with minimal interference. However, in scientific research and clinical applications, it is often desirable to monitor two or more analytes simultaneously in the same biological sample to explore more complex biological processes and reaction mechanisms. Such multiplex detection capabilities are crucial for understanding the dynamic equilibria and interactions within biological systems and have significant clinical value in diagnosing and treating multiple diseases.

In this section, we focus on a subset of TICT-based probes that are engineered not only for viscosity sensitivity, a general property of TICT systems, but also for concurrent response to specific target molecules. These probes integrate multiple sensing mechanisms, enabling dual or multiplex analyte detection in a single measurement. This design strategy enhances their utility in biological imaging and diagnostics, particularly in contexts where interfering parameters such as viscosity and enzyme activity or ion concentration must be correlated. We will detail several representative probes based on the TICT mechanism that exemplify this advanced functionality, discuss their working principles, and demonstrate their applications in biological environments.

Zong *et al.* developed a bifunctional probe **NDI-6** based on a naphthalenediimide (NDI) (Fig. 86), which can detect Cu^{2+} and Hg^{2+}.[353] **NDI-6** contains a NDI molecule as an electron-withdrawing unit, as well as 8-aminoquinoline as an electron donor and ligand for Hg^{2+} and Cu^{2+} ions. This design endows **NDI-6** with strong intramolecular charge transfer capability, resulting in a low band-gap suitable for achieving long-wavelength emission and pronounced color changes. In the presence of Cu^{2+}, the absorption spectrum of **NDI-6** undergoes a red shift, changing the solution color from blue to green enabling naked-eye detection. This phenomenon is mainly due to the deprotonation reaction of the secondary amines in **NDI-6** by Cu^{2+}, enhancing intramolecular charge transfer. After adding Hg^{2+}, **NDI-6** exhibits intense red fluorescence centered at 612 nm, demonstrating a "turn-on" response. This is because the binding of Hg^{2+} to **NDI-6** inhibits the TICT effect, thereby enhancing fluorescence emission. The fluorescence change can be reversed by adding iodide ions (I^-).

Wang *et al.* developed two dual-response fluorescent probes, **CL-1** and **CL-2** (Fig. 87(a)), for the detection of pH and viscosity.[354] **CL-2** extends the conjugated system of **CL-1** to achieve longer fluorescence wavelengths. Over a pH range from 4 to 5, the fluorescence intensity of both **CL-1** and **CL-2** at 540 nm (λ_{ex} = 450 nm) and 585 nm (λ_{ex} = 456 nm), respectively, increases significantly due to protonation occurring within this pH range. As the viscosity increases, the fluorescence intensity of **CL-1** and **CL-2** at 540 nm (λ_{ex} = 450 nm) and 585 nm (λ_{ex} = 456 nm), respectively, also increases significantly. This is because, in high-viscosity environments, the free rotation of single bonds is hindered, thereby suppressing the TICT process and resulting in an enhanced fluorescence intensity. Based on this property, cell colocalization experiments revealed that **CL-1**

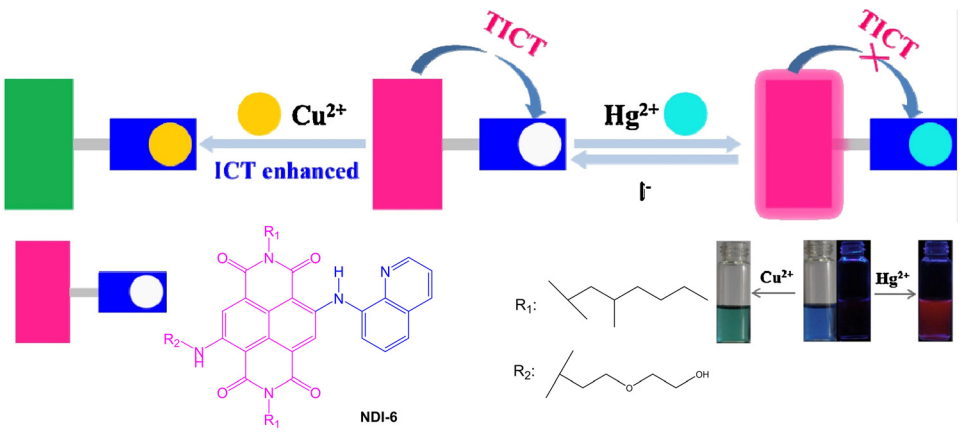

Fig. 86 Chemical structure and schematic illustration of the dual-function probe (**NDI-6**) towards Hg^{2+} and Cu^{2+}. Image reproduced with permission from ref. 353. Copyright 2017, Elsevier.

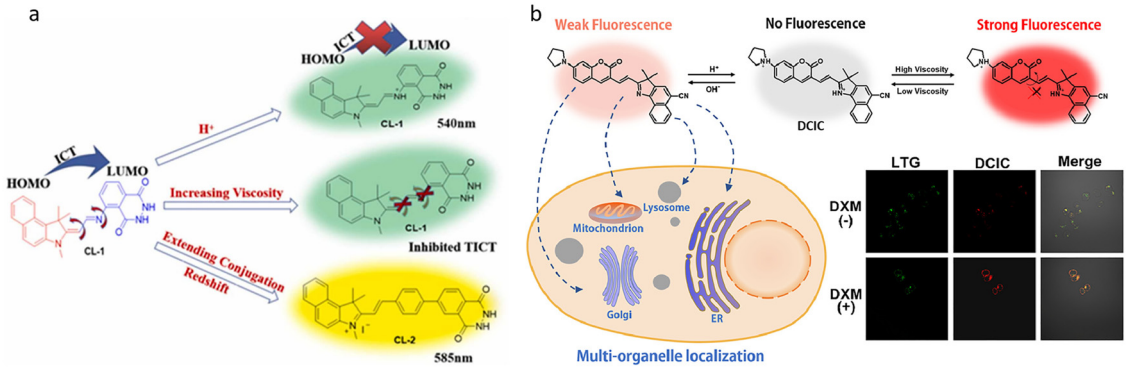

Fig. 87 Chemical structure and schematic illustration of the dual-function probe, (a) **CL-1** and **CL-2**, (b) **DCIC** for the detection of pH and viscosity. Image reproduced with permission from ref. 354 and 355. Copyright 2023, Elsevier. Copyright 2023, Elsevier.

and **CL-2** predominantly localize in lysosomes, exhibiting high overlap with the commercial lysosome dye LysoTracker Deep Red (LTDR), with Pearson correlation coefficients of 0.83 and 0.82, respectively. By administering a solution of **CL-1** and **CL-2** (100 μM, 50 μL) *via* tail vein injection into 4T1 tumor model mice, and performing fluorescence imaging 60 minutes later on the heart, liver, spleen, lungs, kidneys, and tumor, indicated that the fluorescence intensity in tumor tissues was significantly higher than in other organs. This indicates that the probes can serve as highly selective tools for tumor visualization. Recently, Wang and colleagues developed a long-wavelength probe, **DCIC** (Fig. 87(b)), based on a hemicyanine structure, for the detection of pH and viscosity.[355] The fluorescence intensity of the **DCIC** probe at 630 nm gradually increases with the increase in viscosity, enhancing 83-fold in 95% glycerol compared to pure PBS. Additionally, when the solution pH decreases from 8.0 to 2.0, the fluorescence intensity increases by approximately 5-fold. Furthermore, at the cellular level, after treating HeLa cells with dexamethasone (DXM), the fluorescence intensity of **DCIC** in lysosomes significantly increases, which is due to DXM increasing the viscosity of lysosomes, confirming the effectiveness of **DCIC** as a lysosomal viscosity detector.

Fu and colleagues developed a near-infrared fluorescent probe, **FNN** (Fig. 88), which incorporates 1,8-naphthalimide as the fluorescent core and a chalcone moiety as the responsive receptor, enabling the simultaneous detection of N_2H_4 and changes in viscosity.[356] In low-viscosity environments, **FNN** exhibits a high degree of intramolecular rotational freedom, leading to the occurrence of the TICT process and resulting in weak fluorescence. As the viscosity increases, intramolecular rotation is restricted, suppressing the TICT process and significantly enhancing **FNN**'s fluorescence intensity at 620 nm. N_2H_4 undergoes a Michael addition reaction to the chalcone moiety to form **FNN-1**, causing the fluorescence to blue-shift from 620 nm to 520 nm, with a significant increase in fluorescence intensity. **FNN** has been used to assess liver damage induced by hydrazine-based drugs. As such, in Huh7 cells, treatment with isoniazid (INH) leads to a significant increase in **FNN** fluorescence intensity in both channels, indicating the production of N_2H_4 and an increase in cellular viscosity.

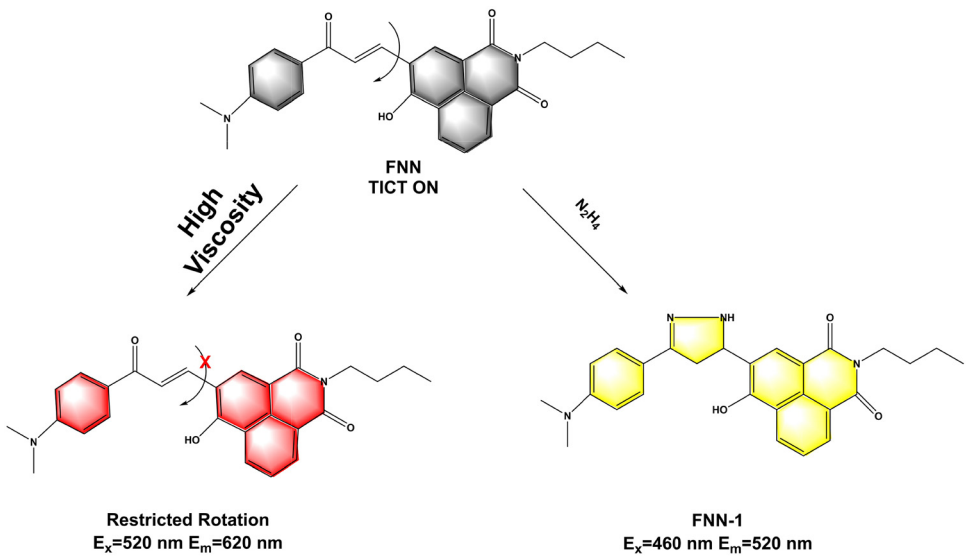

Fig. 88 Chemical structure and schematic illustration of the working principle of **FNN**. Image reproduced with permission from ref. 356. Copyright 2022, The Royal Society of Chemistry.

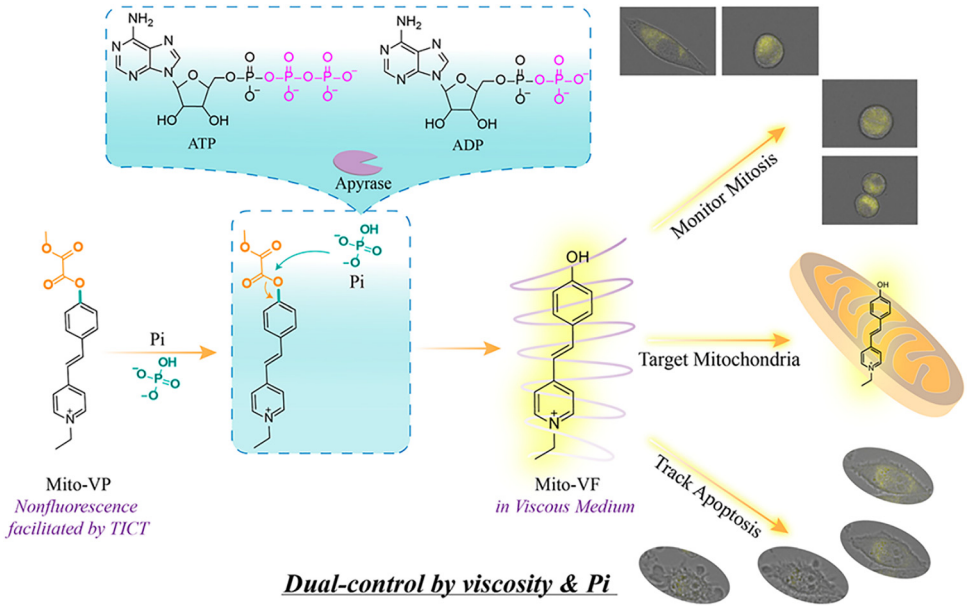

Fig. 89 Proposed sensing mechanism of the probe **Mito-VP** with Pi produced by ATP/ADP hydrolysis and its potential applications. Image reproduced with permission from ref. 357. Copyright 2021, American Chemical Society.

Zhang and colleagues have developed a novel fluorescent probe **Mito-VP** (Fig. 89), which tracks mitochondrial energy metabolism through dual monitoring of phosphate ion (Pi) levels and local microviscosity.[357] The design of **Mito-VP** utilizes a D–π–A structure formed by a strong electron donor (*N*,*N*-diethylaminobenzene) and an electron acceptor (pyridinium) connected through π bonds, and employs methyl oxalate as a reactive moiety for the specific recognition of Pi. **Mito-VF**, as a control probe, does not contain the methyl oxalate reactive moiety. Under 490 nm excitation, both **Mito-VF** and **Mito-VP** exhibit almost no fluorescence emission in low viscosity media, which is mainly due to the TICT process. When evaluated in a glycerol and TBS mixture (simulating a high viscosity environment), **Mito-VF** shows strong yellow fluorescence at 588 nm, while **Mito-VP** still shows minimal emission due to the inhibition of ICT. The product formed by the reaction of **Mito-VP** with Pi gradually enhances fluorescence at 588 nm, and exhibits a good linear relationship with the concentration of Pi (from 0 to 1000 μM), with a detection limit of 170 nM. Using **Mito-VP**, it is possible to monitor the changes of exogenous and endogenous Pi in real-time at the cellular level, which aids in understanding the process of cellular energy metabolism.

Similarly, based on the TICT emission mechanism, Qi *et al.* developed a probe, **VPCPP** (Fig. 90), for the simultaneous monitoring of local microviscosity, micropolarity, and carboxylesterase (CEs) activity in living cells.[358] Li *et al.* developed a multifunctional fluorescent probe, **VLAP** (Fig. 90), capable of detecting intracellular viscosity, polarity, and leucine aminopeptidase (LAP) activity simultaneously.[359] Liu *et al.* developed a novel activatable fluorescent probe, **EaV** (Fig. 90), designed for the simultaneous detection of intracellular esterase activity and viscosity.[360] Zhang *et al.* developed a near-infrared fluorescent probe, **Mito-Th** (Fig. 90), capable of simultaneous detection of mitochondrial viscosity and sulfur dioxide (SO_2).[361] Ren *et al.* developed a fluorescent probe, **Mito-VH** (Fig. 90), capable of the simultaneous detection of mitochondrial viscosity and hydrogen peroxide (H_2O_2).[362] Huang *et al.* developed a multifunctional fluorescent probe, **DPB** (Fig. 90), designed for the simultaneous detection of mitochondrial polarity, viscosity, and peroxynitrite ($ONOO^-$).[363] Kathuria *et al.* have developed two novel fluorescent sensors, **V3** and **V4** (Fig. 90), designed for the precise detection of Fe^{3+} and diethyl chlorophosphate (DCP).[364] Lei *et al.* developed a multifunctional near-infrared (NIR) fluorescent probe, **P-1** (Fig. 90), designed for the simultaneous detection of viscosity, peroxynitrite ($ONOO^-$), and autophagy (mitophagy) within mitochondria.[365] Ma *et al.* developed a dual-responsive fluorescent probe, **HT-Bzh** (Fig. 90), designed for the detection of bisulfite (HSO_3^-) and viscosity.[366] It is worth noting that while viscosity sensitivity is common to TICT probes, the probes discussed here are specifically designed to respond to both viscosity and another specific analyte (*e.g.*, esterase activity, ions, or reactive species). This dual functionality allows researchers to correlate changes in microviscosity with biochemical activity in real time, providing deeper insights into cellular processes such as metabolic dynamics, organelle dysfunction, or drug-induced toxicity.

9. Conclusion and outlook

The field of TICT-based fluorescent probes has witnessed substantial advancements, contributing significantly to the detection and monitoring of biologically and environmentally relevant species. These probes offer unparalleled advantages, including high sensitivity, selectivity, and cost-effective, user-friendly detection methods. The dual emission characteristic of

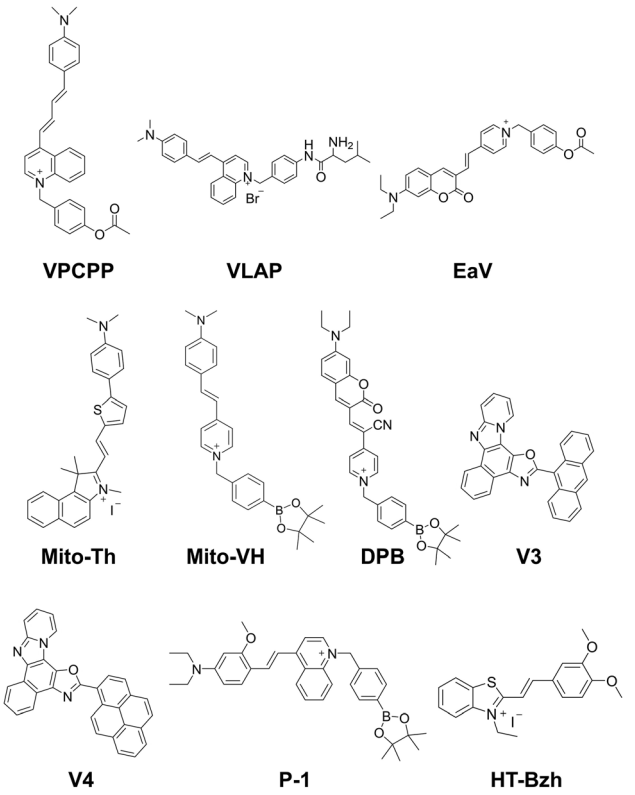

Fig. 90 Chemical structures of probe **VPCPP**, **VLAP**, **EaV**, **Mito-Th**, **Mito-VH**, **DPB**, **V3**, **V4**, **P-1**, and **HT-Bzh**.

TICT-based fluorophores provides ratiometric detection capabilities, enhancing the reliability and accuracy of sensing results by correcting for interferences.

The TICT mechanism enables the creation of probes that can exhibit distinct fluorescence changes upon interacting with target analytes, allowing for off/on or on/off switching of fluorescence in response to specific stimuli. By blocking or releasing the rotation of the rotors in probes, the switching of fluorescence signals between LE/ICT and TICT can be achieved. These kinds of off/on or on/off probes are commonly used for environmental on-site detection of ions and the imaging of biomacromolecules and cellular microenvironments. Besides, this design also provides the possibility of application of TICT-based probes in the field of reversible detection, such as using deprotonation and protonation to block and release intermolecular rotors, thereby realizing the switching of the TICT process and fluorescence responses. Sometimes, to achieve higher selectivity, analyte-responsive sites are introduced into probes. The reaction between response sites and target analytes can lead to chemical structure changes to terminate the TICT process. Such probes are often applied to the detection of small molecules, especially ROS and RNS. When the two design concepts mentioned above are combined to construct TICT-based probes, multiple detection can be achieved, such as logic based or dual responsive detection of small molecules and cellular microenvironments.

Despite these achievements, several challenges remain. The low fluorescence quantum yield of TICT-based fluorophores due to radiationless transitions can limit their sensitivity and applicability. Additionally, improving the photostability and biocompatibility of these probes is crucial for *in vivo* applications, where they must function without causing toxicity or disrupting normal biological processes. Therefore, researchers have started to construct probes incorporating TICT with other photophysical mechanisms to improve their sensing performances. For example, PeT effectively reduces the detection background, thereby solving the problem of poor sensitivity of such dual-emission probes. At the same time, AIE aims to enhance the emission by utilizing the concept of aggregation to improve the fluorescence quantum yield of TICT-based probes. When it comes to the over-sensitivity of TICT probes for environmental detection, ESIPT can reduce excitation light interference by the generation of a large Stokes shift. Additionally, FRET uses effective energy transfer to augment photostability and redshift the fluorescence emission wavelengths.

Future research should be focused on how to more effectively utilize TICT in combination with other fluorescence mechanisms to construct probes to address these challenges and to expand the application of TICT-based probes. Additionally, future efforts should target the development of smart probes capable of responding to multiple stimuli or with targeted delivery capabilities, especially the dual response to molecules and microenvironments, which constitute a potential visualization method for disease pathology exploration. Due to their red-shifted emission spectral characteristics, TICT-based fluorophores have great potential to construct NIR-I and NIR-II probes for intracellular imaging. Due to the advantages of deep tissue penetration, such probes can be used in biomedical fields such as non-invasive disease diagnosis and surgical navigation. As such, integration of TICT-based probes with advanced imaging techniques and developing multimodal probes that combine fluorescence detection with other sensing modalities are important areas of research that should be explored.

In conclusion, the field of TICT-based fluorescent probes is rapidly advancing, driven by continuous innovations that address existing challenges and expand their potential applications. As new materials and technologies emerge, we can expect further improvements in the performance and applicability of TICT-based fluorescent probes, paving the way for their use in a wide range of sensing applications, from environmental monitoring to medical diagnostics and therapeutics.

Conflicts of interest

There are no conflicts to declare.

Abbreviations

AAA	Abdominal aortic aneurysm
ACN	Acetonitrile
AcO^-	Acetate

ActD	Actinomycin D
AD	Alzheimer's disease
AIE	Aggregation-induced emission
AIEE	Aggregation-induced emission enhancement
AKI	Acute kidney injury
AMPK	5′ Adenosine monophosphate-activated protein kinase
ATPase	Adenosine triphosphatase
Aβ	Amyloid-β
BafA1	Bafilomycin A1
BBTD	Benzobisthiadiazole
BODIPY	Boron-dipyrromethene
BSA	Bovine serum albumin
CA	Cinnamaldehyde
CEs	Carboxylesterase
CHEF	Chelation-enhanced fluorescence
ClO^-	Hypochlorite anion
CN^-	Cyanide
$COCl_2$	Phosgene
COVID-19	Coronavirus disease
CTAB	Cetyltrimethylammonium bromide
Cu^{2+}	Copper ion
CYPs	Cytochromes P450
Cys	Cysteine
DAMN	Diaminomaleonitrile
DCM	Dichloromethane
DCP	Diethyl chlorophosphate
DMABN	4-(Dimethylamino)benzonitrile
DMSO	Dimethylsulfoxide
DNA	Deoxyribonucleic acid
DPA	Diphenylamine
DSPE-PEG-2000	1,2-distearoyl-*sn-glycero*-3-phosphoethanolamine-*N*-[carboxy(polyethylene glycol)-2000]
D–π–A	Donor–π–acceptor
EDA	Electron donor–acceptor
EE	Ethyl ether
ER	Endoplasmic reticulum
ESIPT	Excited-state intramolecular proton transfer
EtOH	Ethanol
FRET	Föster resonance energy transfer
GS	Ground state
GSH	Glutathione
HClO	Hypochlorous acid
$HClO_4$	Perchloric acid
HCHO	Formaldehyde
Hcy	Homocysteine
HEPES	*N*-2-Hydroxyethylpiperazine-*N*-2-ethanesulfonic acid
Hexane	*n*-Hexane
HIV-1	Human immunodeficiency virus type 1
HSA	Human serum albumin
ICT	Internal charge transfer
INH	Isoniazid
KI	Potassium iodide
LAP	Leucine aminopeptidase
LDs	Lipid droplets
LE	Locally excited state
LOD	Limit of detection
LTDR	LysoTracker deep red
MASH	Metabolic dysfunction-associated steatohepatitis
MCAO	Middle cerebral artery occlusion
MeOH	Methanol
MP	*N*-Methylpyrrole
MPO	Myeloperoxidase
mRNA	Messenger RNA
mtDNA	Mitochondrial DNA
NADH	Nicotinamide adenine dinucleotide hydride
NAFL	Non-alcoholic fatty liver disease
NH_2NH_2	Hydrazine
NIR	Near-infrared fluorescence
NO_2	Nitrogen dioxide
NO_x	Nitrogen oxides
NPs	Nanoparticles
NTR	Nitroreductase
PAI	Photoacoustic imaging
PAE	Poly(β-amino ester)
PBP	1,7-Dipyridyl-bis(pyrazolo)pyridine
PEG	Polyethylene glycol
PEGMA	Poly(ethylene glycol)methacrylate
PeT	Photoinduced electron transfer
Pi	Phosphate ion
PIEE-LDs	Photoinduced emission enhancement lipid droplets
PMA	Phorbol myristate acetate
PTT	Photothermal therapy
pK_a	Acid dissociation constant
$^{\bullet}OH$	Hydroxyl radical
$ONOO^-$	Peroxynitrite
RA	Rheumatoid arthritis
RCS	Reactive carbonyl species
RNA	Ribonucleic acid
RNase	Ribonuclease
RNS	Reactive nitrogen species
ROS	Reactive oxygen species
rRNA	Ribosomal RNA
RSS	Reactive sulfur species
SA	Serum albumin
SIM	Structured illumination microscopy
STED	Stimulated emission depletion
TBAOH	Tetra-*n*-butyl ammonium hydroxide
TCP	Tricresyl phosphate
TCy5	Thio-pentamethine cyanine
Tg mice	Transgenic mice
TICT	Twisted intramolecular charge transfer
THF	Tetrahydrofuran
ThT	Thioflavin T
TPA	Triphenylamine
TPE	Tetraphenylethylene
tRNA	Transfer RNA
V-ATPases	Vacuolar type H^+-ATPases
VDPs	Vicinal dithiol-containing proteins

VOCs	Volatile organic compounds
WHO	World Health Organization
^1L_a	A band with a longer ''anomalous'' wavelength
^1L_b	B band with a shorter ''normal'' wavelength
2PA	Two-photon absorption
α-syn	Alpha-synuclein
β-gal	β-Galactosidase
β-Lap	β-Lapachone
β-LG	β-Lactoglobulin
Φ_f	Fluorescence quantum yield
Φ_Δ^{rel}	Singlet oxygen generation efficiency

Data availability

No primary research results, software or code have been included and no new data were generated or analysed as part of this review.

Acknowledgements

Y. W. wishes to thank the University of Bath and Liverpool School of Tropical Medicine. T. D. J. wishes to thank the University of Bath and the Open Research Fund of the School of Chemistry and Chemical Engineering, Henan Normal University (2020ZD01) for support. S. E. L. thanks EPSRC for funding (EP/W036193/1). X.-P. H and H.-H. H. are grateful to the National Natural Science Foundation of China (no. 22377135, 22107029, 92253306, and 22477030), the Key R&D Program of Shandong (no. 2024CXPT028), the Shandong Laboratory Program (SYS202205), the Taishan Scholars Program (no. tsqn202312305), the Young Elite Scientists Sponsorship Program by Chinese Chemical Society, the Fundamental Research Projects of Science & Technology Innovation and development Plan in Yantai City (no. 2023JCYJ059), the Science and Technology Commission of Shanghai Municipality (grant no. 24DX1400200), the International Cooperation Program of Shanghai Science and Technology (no. 23490711600), the Shanghai Oriental Talents youth Program (no. QNKJ2024010), the Shanghai Xuhui District Hospital Local Cooperation Project (23XHYD-20), the Open Funding Project of the State Key Laboratory of Fine Chemicals, Dalian University of Technology (KF 2402), the Fundamental Research Funds for the Central Universities (222201717003), the Programme of Introducing Talents of Discipline to Universities (B16017), the Open Funding Project of the State Key Laboratory of Bioreactor Engineering, State Key Laboratory of Chemo/Biosensing and Chemometrics, Hunan University, Changsha 410082, P.R. China, the Ministry of Education Key Laboratory on signaling Regulation and Targeting Therapy of Liver Cancer (Naval Medical University) (grant. 2023-MEKLLC-MS/ZD-00*), and the State Key Laboratory of Drug Research (SKLDR-2025-KF-09).

References

1 M. Muyskens and E. Vitz, *J. Chem. Educ.*, 2006, **83**, 765–768.
2 B. Valeur and M. N. Berberan-Santos, *J. Chem. Educ.*, 2011, **88**, 731–738.
3 T. Ueno and T. Nagano, *Nat. Methods*, 2011, **8**, 642–645.
4 R. Ceredig, *Philos. Trans. R. Soc. A*, 2020, **378**, 20200105.
5 T. Terai and T. Nagano, *Pflügers Arch.*, 2013, **465**, 347–359.
6 Y. Fu and N. S. Finney, *RSC Adv.*, 2018, **8**, 29051–29061.
7 F. Wang, K. Wang, Q. Kong, J. Wang, D. Xi, B. Gu, S. Lu, T. Wei and X. Chen, *Coord. Chem. Rev.*, 2021, **429**, 213636.
8 M. Tian, Y. Ma and W. Lin, *Acc. Chem. Res.*, 2019, **52**, 2147–2157.
9 Z. Guo, S. Park, J. Yoon and I. Shin, *Chem. Soc. Rev.*, 2014, **43**, 16–29.
10 H. H. Han, H. Tian, Y. Zang, A. C. Sedgwick, J. Li, J. L. Sessler, X. P. He and T. D. James, *Chem. Soc. Rev.*, 2021, **50**, 9391–9429.
11 E. Lippert, W. Lüder and H. Boos, Proceedings of the IVth International Meeting on Molecular Spectroscopy, Bologna, 1959.
12 W. Rettig, *Angew. Chem., Int. Ed. Engl.*, 1986, **25**, 971–988.
13 I. Gómez, M. Reguero, M. Boggio-Pasqua and M. A. Robb, *J. Am. Chem. Soc.*, 2005, **127**, 7119–7129.
14 C. Wang, W. Chi, Q. Qiao, D. Tan, Z. Xu and X. Liu, *Chem. Soc. Rev.*, 2021, **50**, 12656–12678.
15 Y. Tu, Y. Yu, D. Xiao, J. Liu, Z. Zhao, Z. Liu, J. W. Y. Lam and B. Z. Tang, *Adv. Sci.*, 2020, **7**, 2001845.
16 K. Rotkiewicz, K. H. Grellmann and Z. R. Grabowski, *Chem. Phys. Lett.*, 1973, **19**, 315–318.
17 W. Rettig, *Electron Transfer I*, Berlin, 1994.
18 S. Sasaki, G. P. C. Drummen and G. Konishi, *J. Mater. Chem. C*, 2016, **4**, 2731–2743.
19 A. M. El-Zohry, E. A. Orabi, M. Karlsson and B. Zietz, *J. Phys. Chem. A*, 2021, **125**, 2885–2894.
20 M. Zhang, J. Li, L. Yu, X. Wang and M. Bai, *RSC Adv.*, 2020, **10**, 14520–14524.
21 S. Liu, X. Zhou, H. Zhang, H. Ou, J. W. Y. Lam, Y. Liu, L. Shi, D. Ding and B. Z. Tang, *J. Am. Chem. Soc.*, 2019, **141**, 5359–5368.
22 C. Cao, X. Liu, Q. Qiao, M. Zhao, W. Yin, D. Mao, H. Zhang and Z. Xu, *Chem. Commun.*, 2014, **50**, 15811–15814.
23 Y. Cai, C. Gui, K. Samedov, H. Su, X. Gu, S. Li, W. Luo, H. H. Y. Sung, J. W. Y. Lam, R. T. K. Kwok, I. D. Williams, A. Qin and B. Z. Tang, *Chem. Sci.*, 2017, **8**, 7593–7603.
24 J. Qi, C. Sun, A. Zebibula, H. Zhang, R. T. K. Kwok, X. Zhao, W. Xi, J. W. Y. Lam, J. Qian and B. Z. Tang, *Adv. Mater.*, 2018, **30**, 1706856.
25 M. M. A. Mazza and F. M. Raymo, *J. Mater. Chem. C*, 2019, **7**, 5333–5342.
26 H. Dong, Y. Wei, W. Zhang, C. Wei, C. Zhang, J. Yao and Y. S. Zhao, *J. Am. Chem. Soc.*, 2016, **138**, 1118–1121.
27 L. Meng, S. Jiang, M. Song, F. Yan, W. Zhang, B. Xu and W. Tian, *ACS Appl. Mater. Interfaces*, 2020, **12**, 26842–26851.
28 R. Rai, R. Bhandari, M. Kaleem, N. Rai, V. Gautam and A. Misra, *J. Photochem. Photobiol., A*, 2023, **441**, 114696.
29 A. Ito, S. Ishizaka and N. Kitamura, *Phys. Chem. Chem. Phys.*, 2010, **12**, 6641–6649.
30 X. Huang, J. Song, B. C. Yung, X. Huang, Y. Xiong and X. Chen, *Chem. Soc. Rev.*, 2018, **47**, 2873–2920.

31 S. H. Park, N. Kwon, J. H. Lee, J. Yoon and I. Shin, *Chem. Soc. Rev.*, 2020, **49**, 143–179.
32 H. Chen, P. Bao, Y. Lv, R. Luo, J. Deng, Y. Yan, D. Ding and H. Gao, *ACS Appl. Mater. Interfaces*, 2023, **15**, 56895–56908.
33 L. Zhao, H. Zhu, Y. Y. Duo, D. W. Pang, Z. G. Wang and S. L. Liu, *Adv. Healthcare Mater.*, 2023, **12**, 2301584.
34 W. Sun, X. Wang, Z. Cheng, X. Wang, N. Fan, P. Dong, M. Tong, Y. Liu and W. Sun, *Biomed. Pharmacother.*, 2023, **158**, 114071.
35 S. Zeng, H. Gao, C. Li, S. Xing, Z. Xu, Q. Liu, G. Feng and D. Ding, *Adv. Healthcare Mater.*, 2021, **10**, 2101063.
36 S. Chen, Y. Hong, Y. Liu, J. Liu, C. W. T. Leung, M. Li, R. T. K. Kwok, E. Zhao, J. W. Y. Lam, Y. Yu and B. Z. Tang, *J. Am. Chem. Soc.*, 2013, **135**, 4926–4929.
37 L. K. Putney and D. L. Barber, *J. Biol. Chem.*, 2003, **278**, 44645–44649.
38 J. R. Casey, S. Grinstein and J. Orlowski, *Nat. Rev. Mol. Cell Biol.*, 2010, **11**, 50–61.
39 R. A. Gottlieb, J. Nordberg, E. Skowronski and B. M. Babior, *Proc. Natl. Acad. Sci. U. S. A.*, 1996, **93**, 654–658.
40 T. A. Davies, R. E. Fine, R. J. Johnson, C. A. Levesque, W. H. Rathbun, K. F. Seetoo, S. J. Smith, G. Strohmeier, L. Volicer, L. Delva and E. R. Simons, *Biochem. Biophys. Res. Commun.*, 1993, **194**, 537–543.
41 H. Izumi, T. Torigoe, H. Ishiguchi, H. Uramoto, Y. Yoshida, M. Tanabe, T. Ise, T. Murakami, T. Yoshida, M. Nomoto and K. Kohno, *Cancer Treat. Rev.*, 2003, **29**, 541–549.
42 A. H. Futerman and G. V. Meer, *Nat. Rev. Mol. Cell Biol.*, 2004, **5**, 554–565.
43 N. Piwon, W. Günther, M. Schwake, M. R. Bösl and T. J. Jentsch, *Nat.*, 2000, **408**, 369–373.
44 F. Yu, Y. Wang, W. Zhu, Y. Huang, M. Yang, H. Ai and Z. Lu, *RSC Adv.*, 2014, **4**, 36849–36853.
45 M. Pérez-Sayáns, J. M. Somoza-Martína, F. Barros-Angueira, J. M. G. Rey and A. García-García, *Cancer Treat. Rev.*, 2009, **35**, 707–713.
46 F. Doria, M. Folini, V. Grande, G. Cimino-Reale, N. Zaffaroni and M. Freccero, *Org. Biomol. Chem.*, 2015, **13**, 570–576.
47 X. Zhu, Q. Lin, P. Chen, Y. P. Fu, Y. M. Zhang and T. B. Wei, *New. J. Chem.*, 2016, **40**, 4562–4565.
48 B. Kim, T. Nevitt and D. Thiele, *Nat. Chem. Biol.*, 2008, **4**, 176–185.
49 E. Madsen and J. D. Gitlin, *Annu. Rev. Neurosci.*, 2007, **30**, 317–337.
50 D. Strozyk, L. J. Launer, P. A. Adlard, R. A. Cherny, A. Tsatsanis, I. Volitakis, K. Blennow, H. Petrovitch, L. R. White and A. I. Bush, *Neurobiol. Aging*, 2009, **30**, 1069–1077.
51 Bharathi, S. S. Indi and K. S. J. Rao, *Neurosci. Lett.*, 2007, **424**, 78–82.
52 C. E. Jones, S. R. Abdelraheim, D. R. Brown and J. H. Viles, *J. Biol. Chem.*, 2004, **279**, 32018–32027.
53 L. Zong, Y. Song, Q. Li and Z. Li, *Sens. Actuators, B*, 2016, **226**, 239–244.
54 M. García, I. Romero and J. Portilla, *ACS Omega*, 2019, **4**, 6757–6768.
55 M. T. Wilson and B. J. Reeder, *Exp. Physiol.*, 2008, **93**, 128–132.
56 T. A. Rouault and W. H. Tong, *Nat. Rev. Mol. Cell Biol.*, 2005, **6**, 345–351.
57 M. Costas, M. P. Mehn, M. P. Jensen and L. Que, *Chem. Rev.*, 2004, **104**, 939–986.
58 D. W. Domaille, E. L. Que and C. J. Chang, *Nat. Chem. Biol.*, 2008, **4**, 168–175.
59 B. Halliwell and J. M. C. Gutteridge, *FEBS Lett.*, 1992, **307**, 108–112.
60 J. Xu, Z. Jia, M. D. Knutson and C. Leeuwenburgh, *Int. J. Mol. Sci.*, 2012, **13**, 2368–2386.
61 X. Huang, *Mutat. Res.*, 2003, **533**, 153–171.
62 S. Toyokuni, *Cancer Sci.*, 2009, **100**, 9–16.
63 K. V. Kowdley, *Gastroenterol.*, 2004, **127**, S79–S86.
64 T. Hirayama, K. Okuda and H. Nagasawa, *Chem. Sci.*, 2013, **4**, 1250–1256.
65 M. Lamoria, R. Kakkar and M. D. Milton, *J. Photochem. Photobiol. A*, 2024, **447**, 115267.
66 Mercury, **https://www.who.int/news-room/fact-sheets/detail/mercury-and-health**, (accessed October 2024).
67 F. Kahrizi, A. Salimi, F. Noorbakhsh, M. Faizi, F. Mehri, P. Naserzadeh, N. Naderi and J. Pourahmad, *Iran. J. Pharm. Res.*, 2016, **15**, 835–841.
68 A. C. Jackson, *Can. J. Neurol. Sci.*, 2018, **45**, 620–623.
69 H. L. Needleman, *JAMA*, 2006, **295**, 1835–1836.
70 T. Takeuchi, N. Morikawa, H. Matsumoto and Y. Shiraishi, *Acta Neuropathol.*, 1962, **2**, 40–57.
71 B. Weiss, *Toxicol. Sci.*, 2007, **97**, 223–225.
72 V. Tharmaraj and K. Pitchumani, *Anal. Chim. Acta*, 2012, **751**, 171–175.
73 Q. Li, M. Peng, H. Li, C. Zhong, L. Zhang, X. Cheng, X. Peng, Q. Wang, J. Qin and Z. Li, *Org. Lett.*, 2012, **14**, 2094–2097.
74 Y. M. Zhang, B. B. Shi, P. Zhang, J. Q. Huo, P. Chen, Q. Lin, J. Liu and T. B. Wei, *Sci. China Chem.*, 2013, **56**, 612–618.
75 A. K. Jha, S. Umar, R. K. Arya, D. Datta and A. Goel, *J. Mater. Chem. B*, 2016, **4**, 4934–4940.
76 L. Zong, Y. Xie, Q. Li and Z. Li, *Sens. Actuators, B*, 2017, **238**, 735–743.
77 C. J. Frederickson, J. Koh and A. I. Bush, *Nat. Rev. Neurosci.*, 2005, **6**, 449–462.
78 E. L. Que, D. W. Domaille and C. J. Chang, *Chem. Rev.*, 2008, **108**, 1517–1549.
79 A. I. Bush, *Trends Neurosci.*, 2003, **26**, 207–214.
80 F. Chimienti, G. A. Rutter, M. B. Wheeler and N. Wijesekara, *Zinc in human health*, IOS Press, 2011.
81 A. Voegelin, S. Pfister, A. C. Scheinost, M. A. Marcus and R. Kretzschmar, *Environ. Sci. Technol.*, 2005, **39**, 6616–6623.
82 Z. P. Zheng, Q. Wei, W. X. Yin, L. T. Wan, X. Huang, Y. Yu and Y. P. Cai, *RSC Adv.*, 2015, **5**, 27682–27689.
83 R. K. Rude, *Am. J. Cardiovasc. Dis.*, 1989, **63**, G31–G34.
84 A. Hartwig, *Mutat. Res.*, 2001, **475**, 113–121.
85 Y. Liu, M. Han, H. Y. Zhang, L. X. Yang and W. Jiang, *Org. Lett.*, 2008, **10**, 2873–2876.
86 S. Bose, V. Ramesh and J. W. Locasale, *Trends Cell Biol.*, 2019, **29**, 695–703.

87 X. Gao, S. H. Lin, F. Ren, J. T. Li, J. J. Chen, C. B. Yao, H. B. Yang, S. X. Jiang, G. Q. Yan, D. Wang, Y. Wang, Y. Liu, Z. Cai, Y. Y. Xu, J. Chen, W. Yu, P. Y. Yang and Q. Y. Lei, *Nat. Commun.*, 2016, **7**, 11960.
88 Q. Lin, X. Liu, T. B. Wei and Y. M. Zhang, *Sens. Actuators, B*, 2014, **190**, 459–463.
89 Z. Xu, X. Chen, H. N. Kim and J. Yoon, *Chem. Soc, Rev.*, 2010, **39**, 127–137.
90 D. Shan, C. Mousty and S. Cosnier, *Anal. Chem.*, 2004, **76**, 178–183.
91 B. Chen, Y. Ding, X. Li, W. Zhu, J. P. Hill, K. Ariga and Y. Xie, *Chem. Commun.*, 2013, **49**, 10136–10138.
92 G. Balamurugan, P. Venkatesan, S. P. Wu and S. Velmathi, *RSC Adv.*, 2016, **6**, 24229–24235.
93 O. A. Pegu and G. Das, *J. Mater. Chem. C*, 2024, **12**, 6519–6527.
94 M. P. Curtis, A. J. Hicks and J. W. Neidigh, *Chem. Res. Toxicol.*, 2011, **24**, 418–428.
95 V. N. Nguyen, J. Ha, M. Cho, H. Li, K. M. K. Swamy and J. Yoon, *Coord. Chem. Rev.*, 2021, **439**, 213936.
96 Z. M. Prokopowicz, F. Arce, R. Biedron, C. L.-L. Chiang, M. Ciszek, D. R. Katz, M. Nowakowska, S. Zapotoczny, J. Marcinkiewicz and B. M. Chain, *J. Immunol.*, 2010, **184**, 824–835.
97 J. I. Kang and L. C. Sowers, *Chem. Res. Toxicol.*, 2008, **21**, 1211–1218.
98 S. Sugiyama, K. Kugiyama, M. Aikawa, S. Nakamura, H. Ogawa and P. Libby, *Arterioscler., Thromb., Vasc. Biol.*, 2004, **24**, 1309–1314.
99 Y. W. Yap, M. Whiteman and N. S. Cheung, *Cell. Signalling*, 2007, **19**, 219–228.
100 M. Miljkovic-Lolic, R. Silbergleit, G. Fiskum and R. E. Rosenthal, *Brain Res.*, 2003, **971**, 90–94.
101 J. D. Hayes, A. T. Dinkova-Kostova and K. D. Tew, *Cancer Cell*, 2020, **38**, 167–197.
102 Z. Lou, P. Li, Q. Pan and K. Han, *Chem. Commun.*, 2013, **49**, 2445–2447.
103 Z. Lou, S. Yang, P. Li, P. Zhou and K. Han, *Phys. Chem. Chem. Phys.*, 2014, **16**, 3749–3756.
104 S. Mu, L. Jiang, H. Gao, J. Zhang, H. Sun, X. Shi, X. Liu and H. Zhang, *Anal. Chim. Acta*, 2022, **1191**, 339287.
105 S. Shao, T. Yang and Y. Han, *Sens. Actuators, B*, 2023, **392**, 134041.
106 G. K. Kolluru, X. Shen, S. C. Bir and C. G. Kevil, *Nitric Oxide*, 2013, **35**, 5–20.
107 S. Das, in *Toxicology Cases for the Clinical and Forensic Laboratory*, ed. H. Ketha and U. Garg, Elsevier, 2020, ch. 20, pp. 387–396.
108 C. S. Maldonado, A. Weir and W. K. Rumbeiha, *Toxicol. Mech, Methods*, 2023, **33**, 183–196.
109 P. D. Beer and P. A. Gale, *Angew. Chem., Int. Ed.*, 2001, **40**, 486–516.
110 L. Zong, M. Zhang, Y. Song, Y. Xie, J. Feng, Q. Li and Z. Li, *Sens. Actuators, B*, 2018, **257**, 882–888.
111 M. Ren, B. Deng, X. Kong, K. Zhou, K. Liu, G. Xu and W. Lin, *Chem. Commun.*, 2016, **52**, 6415–6418.
112 J. Meng, H. C. Liu, Y. Y. Guo, F. Wang, D. J. Pi and Q. Z. Yu, *Spectrochim. Acta, Part A*, 2023, **288**, 122191.
113 W. Li, Y. Wang and R. Zhang, *Spectrochim. Acta A*, 2023, **302**, 123125–123132.
114 H. Tian, J. Qian, Q. Sun, H. Bai and W. Zhang, *Anal. Chim. Acta*, 2013, **788**, 165–170.
115 X. Cheng, H. Jia, J. Feng, J. Qin and Z. Li, *Sens. Actuators, B*, 2013, **184**, 274–280.
116 Y. Sun, S. Fan, S. Zhang, D. Zhao, L. Duan and R. Li, *Sens. Actuators, B*, 2014, **193**, 173–177.
117 L. Zhu, J. Xu, Z. Sun, B. Fu, C. Qin, L. Zeng and X. Hu, *Chem. Commun.*, 2015, **51**, 1154–1156.
118 H. Yin, B. Zhang, H. Yu, L. Zhu, Y. Feng, M. Zhu, Q. Guo and X. Meng, *J. Org. Chem.*, 2015, **80**, 4306–4312.
119 S. Yu, X. Yang, Z. Shao, Y. Feng, X. Xi, R. Shao, Q. Guo and X. Meng, *Sens. Actuators, B*, 2016, **235**, 362–369.
120 C. Szabo, H. Ischiropoulos and R. Radi, *Nat. Rev. Drug Discov.*, 2007, **6**, 662–680.
121 S. Bartesaghi and R. Radi, *Redox Biol.*, 2018, **14**, 618–625.
122 R. Radi, *J. Biol. Chem.*, 2013, **288**, 26464–26472.
123 P. Pacher, J. S. Beckman and L. Liaudet, *Physiol. Rev.*, 2007, **87**, 315–424.
124 F. Torreilles, S. Salman-Tabcheh, M.-C. Guérin and J. Torreilles, *Brain Res. Rev.*, 1999, **30**, 153–163.
125 Z. Zhan, L. Chai, H. Yang, Y. Dai, Z. Wei, D. Wang and Y. Lv, *Anal. Chem.*, 2023, **95**, 5585–5593.
126 G. Wang, Z. Wan, Z. Cai, J. Li, Y. Li, X. Hu, D. Lei and X. Dou, *Anal. Chem.*, 2022, **94**, 11679–11687.
127 J. L. Sessler, P. A. Gale and W.-S. Cho, *Anion Receptor Chemistry*, Royal Society of Chemistry, UK, 2006.
128 D. L. Correll, *J. Environ. Qual.*, 1998, **27**, 261–266.
129 (*a*) B. B. Shi, Y. M. Zhang, T. B. Wei, Q. Lin, H. Yao, P. Zhang and X. M. You, *Sens. Actuators, B*, 2014, **190**, 555–561; (*b*) B. B. Shi, Y. M. Zhang, T. B. Wei, P. Zhang, Q. Lin and H. Yao, *New J. Chem.*, 2013, **37**, 3737–3744.
130 J. A. Knight, *Ann. Clin. Lab. Sci.*, 2000, **30**, 145–158.
131 H. Ahsan, A. Ali and R. Ali, *Clin. Exp. Immunol*, 2003, **131**, 398–404.
132 H. Sheng, K. Nakamura, T. Kanno, K. Sasaki and Y. Niwano, *Interface Oral Health Science*, Springer, Tokyo, 2014, 203–216.
133 B. Balasubramanian, W. K. Pogozelski and T. D. Tullius, *Proc. Natl. Acad. Sci. U. S. A.*, 1998, **95**, 9738–9743.
134 H. Wiseman and B. Halliwell, *Biochem. J*, 1996, **313**, 17–29.
135 P. Huang, L. Feng, E. A. Oldham, M. J. Keating and W. Plunkett, *Nat.*, 2000, **407**, 390–395.
136 M. Talha, A. R. Mir, S. Habib, M. Abidi, M. S. Warsi, S. Islam and Moinuddin, *Spectrochim. Acta, Part A*, 2021, **255**, 119640.
137 L. Chen, X. Wu, H. Yu, L. Wu, Q. Wang, J. Zhang, X. Liu, Z. Li and X. F. Yang, *Anal. Chem.*, 2021, **93**, 14343–14350.
138 X. F. Wang and M. S. Cynader, *J. Neurosci.*, 2001, **21**, 3322–3331.
139 W. Wang, O. Rusin, X. Xu, K. K. Kim, J. O. Escobedo, S. O. Fakayode, K. A. Fletcher, M. Lowry, C. M. Schowalter, C. M. Lawrence, F. R. Fronczek, I. M. Warner and R. M. Strongin, *J. Am. Chem. Soc.*, 2005, **127**, 15949–15958.

140 X. Wei, X. Yang, Y. Feng, P. Ning, H. Yu, M. Zhu, X. Xi, Q. Guo and X. Meng, *Sens. Actuators, B*, 2016, **231**, 285–292.
141 T. Salthammer, *Angew. Chem., Int. Ed.*, 2013, **52**, 3320–3327.
142 H. W. Chen, H. Li and Q. H. Song, *ACS Omega*, 2018, **3**, 18189–18195.
143 K. Tulpule and R. Dringen, *J. Neurochem.*, 2013, **127**, 7–21.
144 C. M. Thompson, R. Ceder and R. C. Grafström, *Toxicol. Lett.*, 2010, **193**, 1–3.
145 J. O'Sullivan, M. Unzeta, J. Healy, M. I. O'Sullivan, G. Davey and K. F. Tipton, *Neurotoxicology*, 2004, **25**, 303–315.
146 L. J. Walport, R. J. Hopkinson, R. Chowdhury, R. Schiller, W. Ge, A. Kawamura and C. J. Schofield, *Nat. Commun.*, 2016, **7**, 11974.
147 R. Q. He, J. Lu and J. Y. Miao, *Sci. China Life Sci.*, 2010, **53**, 1399–1404.
148 B. Kalyanaraman and B. K. Sinha, *Environ. Health Perspect.*, 1985, **64**, 179–184.
149 A. Umar, M. M. Rahman, S. H. Kim and Y.-B. Hahn, *Chem. Commun.*, 2008, 166–168.
150 C. Batchelor-McAuley, C. E. Banks, A. O. Simm, T. G. J. Jones and R. G. Compton, *Analyst*, 2006, **131**, 106–110.
151 D. P. Elder, D. Snodin and A. Teasdale, *J. Pharm. Biomed. Anal.*, 2011, **54**, 900–910.
152 C. A. Reilly and S. D. Aust, *Chem. Res. Toxicol.*, 1997, **10**, 328–334.
153 X. Chen, Y. Xiang, Z. Li and A. Tong, *Anal. Chim. Acta*, 2008, **625**, 41–46.
154 B. Chen, X. Sun, X. Li, H. Ågren and Y. Xie, *Sens. Actuators, B*, 2014, **199**, 93–100.
155 D. Zhou, Y. Wang, J. Jia, W. Yu, B. Qu, X. Li and X. Sun, *Chem. Commun.*, 2015, **51**, 10656–10659.
156 R. C. Gupta, S. K. Dwivedi, R. Ali, S. S. Razi, R. Tiwari, S. Krishnamoorthi and A. Misra, *Spectrochim. Acta, Part A*, 2020, **232**, 118153.
157 F. Rezende, R. P. Brandes and K. Schröder, *Antioxid. Redox Signal.*, 2018, **29**, 585–602.
158 S. G. Rhee, T. S. Chang, W. Jeong and D. Kang, *Mol. Cell*, 2010, **29**, 539–549.
159 P. Leanderson, K. Wennerberg and C. Tagesson, *J. Carcinog.*, 1994, **15**, 137–139.
160 M. T. Lin and M. F. Beal, *Nature*, 2006, **443**, 787–795.
161 K. Brieger, S. Schiavone, F. J. Miller and K. H. Krause, *Swiss Med. Wkly.*, 2012, **142**, w13659.
162 M. Kumar, N. Kumar, V. Bhalla, P. R. Sharma and Y. Qurishi, *Chem. Commun.*, 2012, **48**, 4719–4721.
163 F. Wu, H. Yu, Q. Wang, J. Zhang, Z. Li and X. F. Yang, *Dyes Pigm.*, 2021, **190**, 109335–109342.
164 M. P. P. Monterola, B. W. Smith, N. Omenetto and J. D. Winefordner, *Anal. Bioanal. Chem.*, 2008, **391**, 2617–2626.
165 Y. Sun, Y. Shu, T. Xu, M. Shui, Z. Zhao, Y. Gu and X. Wang, *Cent. Eur. J. Energ. Mater.*, 2012, **9**, 411–423.
166 T. W. Hesterberg, W. B. Bunn, R. O. Mcclellan, A. K. Hamade, C. M. Long and P. A. Valberg, *Crit. Rev. Toxicol.*, 2009, **39**, 743–781.
167 J. B. Chen, B. Li, Y. Xiong and J. Sun, *Sens. Actuators, B*, 2018, **255**, 275–282.
168 J. D. Larkin, K. A. Frimat, T. M. Fyles, S. E. Flower and T. D. James, *New J. Chem.*, 2010, **34**, 2922–2931.
169 Y. Zhang, Z. He and G. Li, *Talanta*, 2010, **81**, 591–596.
170 R. Hosseinzadeh, M. Mohadjerani, M. Pooryousef, A. Eslami and S. Emami, *Spectrochim. Acta, Part A*, 2015, **144**, 53–60.
171 S. Liu, H. Bai, Q. Sun, W. Zhang and J. Qian, *RSC Adv.*, 2015, **5**, 2837–2843.
172 D. Oesch and N. W. Luedtke, *Chem. Commun.*, 2015, **51**, 12641–12644.
173 H. Saito, Y. Sobue, T. Sugaya, S. Iwatsuki, M. Inamo and K. Ishihara, *ChemPhotoChem*, 2023, **7**, e202200271.
174 L. Suo, W. Huang, Q. Zhu, L. Ma and M. Hu, *J. Sci. Food Agric.*, 2018, **98**, 5287–5293.
175 A. Marklund, B. Andersson and P. Haglund, *Chemosphere*, 2003, **53**, 1137–1146.
176 H. Liu, N. Zhu, M. Li, X. Huang, P. Wu, Z. Hu and J. Shuai, *Sci. Total Environ.*, 2020, **713**, 136488.
177 S. Sun, J. Jiang, H. Zhao, H. Wan and B. Qu, *Chemosphere*, 2020, **241**, 124971.
178 M. J. Fabianska, B. Kozielska, J. Konieczynski and P. Bielaczyc, *Environ. Pollut.*, 2019, **244**, 351–360.
179 Q. Luo, Y. Shan, A. Muhammad, S. Wang, L. Sun and H. Wang, *Environ. Sci. Pollut. Res. Int.*, 2018, **25**, 31752–31761.
180 Y. Tian, X. Huang, H. Li, Q. Chen, X. Gong, H. Chen, M. Fan and Z. Gong, *Anal. Chim. Acta*, 2024, **1285**, 342009.
181 J. Bartzis, P. Wolkoff, M. Stranger, G. Efthimiou, E. I. Tolis, F. Maes, A. W. Norgaard, G. Ventura, K. K. Kalimeri, E. Goelen and O. Fernandes, *J. Hazard. Mater.*, 2015, **285**, 37–45.
182 H. L. Wang, L. Nie, J. Li, Y. F. Wang, G. Wang, J. H. Wang and Z. P. Hao, *Chin. Sci. Bull.*, 2013, **58**, 724–730.
183 A. K. Pathak, R. K. Gangwar, P. Priyadarshini and V. K. Singh, *Optik*, 2017, **149**, 43–48.
184 G. Brundrett, *Int. J. Ambient Energy*, 2010, **31**, 161.
185 A. K. Pathak and C. Viphavakit, *Sens. Actuators A*, 2022, **338**, 113455–113479.
186 M. Zhang, Y. Zhang, Y. Li, J. Wei, L. Xu, J. Yuan, Z. Xu, Y. Duan and T. Han, *Dyes Pigm.*, 2023, **220**, 111704.
187 D. G. Levitt and M. D. Levitt, *Int. J. Gen. Med.*, 2016, **9**, 229–255.
188 J. Rozga, T. Piatek and P. Malkowski, *Ann. Transplant.*, 2013, **18**, 205–217.
189 E. Gremese, D. Bruno, V. Varriano, S. Perniola, L. Petricca and G. Ferraccioli, *J. Clin. Med.*, 2023, **12**, 6017–6031.
190 M. Dockal, D. C. Carter and F. Rüker, *J. Biol. Chem.*, 1999, **274**, 29303–29310.
191 G. Sudlow, D. J. Birkett and D. N. Wade, *Mol. Pharmacol.*, 1975, **11**, 824–832.
192 D. C. Carter and J. X. Ho, *Adv. Protein Chem*, 1994, **45**, 153–203.
193 S. Naveenraj and S. Anandan, *J. Photochem. Photobiol., C*, 2013, **14**, 53–71.
194 A. Bujacz, *Acta Crystallogr., Sect. D: Biol. Crystallogr.*, 2012, **68**, 1278–1289.
195 S. I. Reja, I. A. Khan, V. Bhalla and M. Kumar, *Chem. Commun.*, 2016, **52**, 1182–1185.

196 H. Li, Q. Yao, J. Fan, J. Du, J. Wang and X. Peng, *Dyes Pigm.*, 2016, **133**, 79–85.
197 P. Shen, J. Hua, H. Jin, J. Du, C. Liu, W. Yang, Q. Gao, H. Luo, Y. Liu and C. Yang, *Sens. Actuators, B*, 2017, **247**, 587–594.
198 C. Liu, W. Yang, Q. Gao, J. Du, H. Luo, Y. Liu and C. Yang, *J. Lumin.*, 2018, **197**, 193–199.
199 S. Samanta, S. Halder and G. Das, *Anal. Chem.*, 2018, **90**, 7561–7568.
200 P. Li, Y. Wang, S. Zhang, L. Xu, G. Wang and J. Cui, *Tetrahedron Lett.*, 2018, **59**, 1390–1393.
201 D. J. Zheng, J. Xu, M. M. Su, Z. G. Sun, Q. C. Jiao, Y. S. Yang and H. L. Zhu, *Sens. Actuators, B*, 2018, **271**, 82–89.
202 J. Du, W. Ma, Q. Gu, Q. Yao, S. Long, W. Sun, J. Fan and X. Peng, *Sens. Actuators, B*, 2019, **287**, 118–123.
203 S. Lee, D. B. Sung, S. Kang, S. Parameswaran, J. H. Choi, J. S. Lee and M. S. Han, *Sensors*, 2019, **19**, 5298–5310.
204 Y. Luo, Q. Q. Yu, J. J. Gao, X. X. Lang, H. Y. Li, X. F. Yu, X. Y. Qi and M. Q. Wang, *Bioorg. Med. Chem. Lett.*, 2021, **53**, 128438.
205 Y. Ke, J. Cao, J. Gong and N. Fu, *Sens. Actuators, B*, 2022, **352**, 131015–131023.
206 L. Su, F. Yang, W. Li, H. Li, C. Wang, Q. Wang and L. Yuan, *Mater. Chem. Front.*, 2022, **6**, 3084–3093.
207 Y. Fan, F. Wang, F. Hou, L. Wei, G. Zhu, D. Zhao, Q. Hu, T. Lei, L. Yang, P. Wang and G. Ge, *Chin. Chem. Lett.*, 2023, **34**, 107557–107560.
208 H. Wang, J. Wang, G. Ma, J. Zhou, L. Du, H. Wu, X. Zhang, Y. He and J. Zhou, *Chem. Eng. J.*, 2023, **464**, 142551.
209 M. Zhang, J. Cao, C. Huang, M. Liu, Y. Li, C. Wang and Y. Tu, *Dyes Pigm.*, 2023, **208**, 110867.
210 Y. Zhang, W. Zhou, N. Xu, G. Wang, J. Li, K. An, W. Jiang, X. Zhou, Q. Qiao, X. Jiang and Z. Xu, *Chin. Chem. Lett.*, 2023, **34**, 107472–107475.
211 A. Bandyopadhyay, R. Hazra, D. Roy and A. Bhattacharya, *Chem. Asian J.*, 2024, **19**, e202301055.
212 Y. Dai, J. Gong, J. Cao, W. Chen and N. Fu, *Dyes Pigm.*, 2024, **222**, 111893.
213 J. W. Taanman, *Biochim. Biophys. Acta*, 1999, **1410**, 103–123.
214 E. A. Schon, S. DiMauro and M. Hirano, *Nat. Rev. Genet.*, 2012, **13**, 878–890.
215 S. Anderson, A. T. Bankier, B. G. Barrell, M. H. L. Debruijn, A. R. Coulson, J. Drouin, I. C. Eperon, D. P. Nierlich, B. A. Roe, F. Sanger, P. H. Schreier, A. J. H. Smith, R. Staden and I. G. Young, *Nature*, 1981, **290**, 457–465.
216 M. Zeviani and V. Carelli, *Curr. Opin. Neurol*, 2007, **20**, 564–571.
217 M. Falkenberg, N. G. Larsson and C. M. Gustafsson, *Annu. Rev. Biochem.*, 2007, **76**, 679–699.
218 C. A. Nadalutti, S. Ayala-Peña and J. H. Santos, *Am. J. Physiol. Cell Physiol.*, 2022, **322**, 136–150.
219 I. M. Serrano, M. Hirose, C. C. Valentine, S. Roesner, E. Schmidt, G. Pratt, L. Williams, J. Salk, S. Ibrahim and P. H. Sudmant, *Nat. Ecol. Evol.*, 2024, **8**, 1021–1034.
220 Y. Wang, H. Niu, K. Wang, G. Wang, J. Liu, T. D. James and H. Zhang, *Anal. Chem.*, 2022, **94**, 7510–7519.
221 Y. S. Choi, W. Patena, A. D. Leavitt and M. T. McManus, *RNA*, 2012, **18**, 394–401.
222 K. V. Morris, *Nutr. Rev.*, 2008, **66**, S31–S32.
223 S. M. Fica, N. Tuttle, T. Novak, N. S. Li, J. Lu, P. Koodathingal, Q. Dai, J. P. Staley and J. A. Piccirilli, *Nature*, 2013, **503**, 229–234.
224 C. Cao, P. Wei, R. Li, Y. Zhong, X. Li, F. Xue, Y. Shi and T. Yi, *ACS Sens.*, 2019, **4**, 1409–1416.
225 H. Wang, X. Lu, F. Chen, Y. Ding, H. Zheng, L. Wang, G. Zhang, J. Yang, Y. Bai, J. Li, J. Wu, M. Zhou and L. Xu, *Brief. Bioinform*, 2020, **21**, 85–95.
226 X. Lu, Y. Ding, Y. Bai, J. Li, G. Zhang, S. Wang, W. Gao, L. Xu and H. Wang, *Front. Cell Dev. Biol.*, 2020, **8**, 242.
227 Z. Wang, C. Wang, T. Fang and Y. Liu, *Dyes Pigm.*, 2022, **200**, 110126.
228 W. Jiang, Q. Qiao, J. Chen, P. Bao, Y. Tao, Y. Zhang and Z. Xu, *Adv. Sci.*, 2024, **11**, 2309743.
229 K. M. Trujillo, S. S. F. Yuan, E. Y. H. P. Lee and P. Sung, *J. Biol. Chem.*, 1998, **273**, 21447–21450.
230 S. Vescia, D. Tramontano, G. Augustitocco and G. Dalessio, *Cancer Res.*, 1980, **40**, 3740–3744.
231 T. M. Marti and O. Fleck, *Cell. Mol. Life Sci.*, 2004, **61**, 336–354.
232 D. Basso, C. Fabris, A. Meani, G. Delfavero, A. Panucci, D. Vianello, A. Piccoli and R. Naccarato, *Tumori*, 1985, **71**, 529–532.
233 S. Li, M. G. Hu, Y. Sun, N. Yoshioka, S. Ibaragi, J. Sheng, G. Sun, K. Kishimoto and G. Hu, *Mol. Cancer Res*, 2013, **11**, 1203–1214.
234 O. A. Shklyaeva, N. L. Mironova, E. M. Malkova, O. S. Taranov, E. I. Ryabchikova, M. A. Zenkova and V. V. Vlasov, *Dokl. Biochem. Biophys.*, 2008, **420**, 108–111.
235 (*a*) J. Du, N. Huang, Z. Xiang, Y. Dong, Q. Gao, W. Yang and C. Yang, *J. Lumin.*, 2018, **204**, 162–168; (*b*) W. Yang, C. L. Liu, Q. Y. Gao, J. Y. Du, P. Shen and C. Y. Yang, *J. Fluoresc.*, 2017, **27**, 391–398.
236 C. Gitler, B. Zarmi and E. Kalef, *Anal. Biochem.*, 1997, **252**, 48–55.
237 B. A. Maron, S. S. Tang and J. Loscalzo, *Antioxid. Redox Signal.*, 2013, **18**, 270–287.
238 J. Ying, N. Clavreul, M. Sethuraman, T. Adachi and R. A. Cohen, *Free Radic. Biol. Med.*, 2007, **43**, 1099–1108.
239 M. Valko, C. J. Rhodes, J. Moncol, M. Izakovic and M. Mazur, *Chem. - Biol. Interact.*, 2006, **160**, 1–40.
240 L. J. Matthias and P. J. Hogg, *Antioxid. Redox Signaling*, 2003, **5**, 133–138.
241 G. Bánhegyi, J. Mandl and M. Csala, *J. Neurochem.*, 2008, **107**, 20–34.
242 X. J. Dai, W. J. Li, D. D. Xie, B. X. Liu, L. Gong and H. H. Han, *Small*, 2025, **21**, 2410030.
243 Y. Wang, Y. Zhong, Q. Wang, X. F. Yang, Z. Li and H. Li, *Anal. Chem.*, 2016, **88**, 10237–10244.
244 J. Zhang, P. Cheng and K. Pu, *Bioconjugate Chem.*, 2019, **30**, 2089–2101.
245 X. Li, Y. Pan, H. Chen, Y. Duan, S. Zhou, W. Wu, S. Wang and B. Liu, *Anal. Chem.*, 2020, **92**, 5772–5779.

246 X. Li, W. Qiu, J. Li, X. Chen, Y. Hu, Y. Gao, D. Shi, X. Li, H. Lin, Z. Hu, G. Dong, C. Sheng, B. Jiang, C. Xia, C. Y. Kim, Y. Guo and J. Li, *Chem. Sci.*, 2020, **11**, 7292–7301.
247 X. Chai, H. H. Han, A. C. Sedgwick, N. Li, Y. Zang, T. D. James, J. Zhang, X. L. Hu, Y. Yu, Y. Li, Y. Wang, J. Li, X. P. He and H. Tian, *J. Am. Chem. Soc.*, 2020, **142**, 18005–18013.
248 B. Lozano-Torres, I. Galiana, M. Rovira, E. Garrido, S. Chaib, A. Bernardos, D. Muñoz-Espín, M. Serrano, R. Martínez-Máñez and F. Sancenón, *J. Am. Chem. Soc.*, 2017, **139**, 8808–8811.
249 D. Asanuma, M. Sakabe, M. Kamiya, K. Yamamoto, J. Hiratake, M. Ogawa, N. Kosaka, P. L. Choyke, T. Nagano, H. Kobayashi and Y. Urano, *Nat. Commun.*, 2015, **6**, 6463–6469.
250 X. Zhen, J. Zhang, J. Huang, C. Xie, Q. Miao and K. Pu, *Angew. Chem., Int. Ed.*, 2018, **57**, 7804–7808.
251 Y. Niu, H. Wang, Y. Wang and L. Feng, *Microchem. J.*, 2021, **166**, 106205–106212.
252 J. L. Cummings and G. Cole, *JAMA*, 2002, **287**, 2335–2338.
253 J. Hardy and D. J. Selkoe, *Sci.*, 2002, **297**, 353–356.
254 V. L. Villemagne, S. Burnham, P. Bourgeat, B. Brown, K. A. Ellis, O. Salvado, C. Szoeke, S. L. Macaulay, R. Martins, P. Maruff, D. Ames, C. C. Rowe, C. L. Masters and AIBL, *Lancet Neurol.*, 2013, **12**, 357–367.
255 O. Hansson, *Nat. Med.*, 2021, **27**, 954–963.
256 B. A. Gordon, T. M. Blazey, Y. Su, A. Hari-Raj, A. Dincer, S. Flores, J. Christensen, E. McDade, G. Wang, C. Xiong, N. J. Cairns, J. Hassenstab, D. S. Marcus, A. M. Fagan, C. R. Jack, R. C. Hornbeck, K. L. Paumier, B. M. Ances, S. B. Berman, A. M. Brickman, D. M. Cash, J. P. Chhatwal, S. Correia, S. Förster, N. C. Fox, N. R. Graff-Radford, C. la Fougere, J. Levin, C. L. Masters, M. N. Rossor, S. Salloway, A. J. Saykin, P. R. Schofield, P. M. Thompson, M. M. Weiner, D. M. Holtzman, M. E. Raichle, J. C. Morris, R. J. Bateman and T. L. Benzinger, *Lancet Neurol.*, 2018, **17**, 241–250.
257 N. Yue, H. Fu, Y. Chen, X. Gao, J. Dai and M. Cui, *Eur. J. Med. Chem.*, 2022, **243**, 114715.
258 S. Neupane, E. D. Cecco and A. Aguzzi, *J. Mol. Biol.*, 2023, **435**, 167930.
259 P. Gracia, J. D. Camino, L. Volpicelli-Delay and N. Cremades, *Int. J. Mol. Sci.*, 2020, **21**, 8043.
260 Y. Venkatesh, N. Marotta, V. M. Y. Lee and E. J. Petersson, *Chem. Sci.*, 2024, **15**, 6053–6063.
261 G. Anwar, D. Chen, Q. Chen, C. Xia and J. Yan, *Spectrochim. Acta, Part A*, 2024, **307**, 123637.
262 L. M. Needham, J. Weber, J. A. Varela, J. W. B. Fyfe, D. T. Do, C. K. Xu, L. Tutton, R. Cliffe, B. Keenlyside, D. Klenerman, C. M. Dobson, C. A. Hunter, K. H. Müller, K. O'Holleran, S. E. Bohndiek, T. N. Snaddon and S. F. Lee, *Chem. Sci.*, 2020, **11**, 4578–4583.
263 R. Tao, N. Wang, T. Shen, Y. Tan, Y. Ren, W. Wei, M. Liao, D. Tan, C. Tang, N. Xu, H. Wang, X. Liu and X. Li, *Theranostics*, 2022, **12**, 2549–2559.
264 C. Wang, W. Jiang, D. Tan, L. Huang, J. Li, Q. Qiao, P. Yadav, X. Liu and Z. Xu, *Chem. Sci.*, 2023, **14**, 4786–4795.
265 J. Miao, M. Miao, Y. Jiang, M. Zhao, Q. Li, Y. Zhang, Y. An, K. Pu and Q. Miao, *Angew. Chem., Int. Ed.*, 2023, **62**, e202216351.
266 H. Cheng, Y. Zhao, H. Xu, Y. Hu, L. Zhang, G. Song and Z. Yao, *Dyes Pigm.*, 2020, **180**, 108456.
267 Y. Y. Liu, X. F. Chen, J. W. Hu, Z. W. Chen, L. J. Zhang, M. J. Cao and G. M. Liu, *J. Agric. Food Chem.*, 2016, **64**, 1999–2011.
268 L. C. Chang, H. F. Lee, M. J. Chung and V. C. Yang, *Bioconjugate Chem.*, 2005, **16**, 147–155.
269 Y. Yu, K. Bruzdoski, V. Kostousov, L. Hensch, S. Hui, F. Siddiqui, A. Farooqui, A. Kouta, F. Zhang, J. Fareed, J. Teruya and R. J. Linhardt, *Carbohydr. Polym.*, 2020, **244**, 116443–116451.
270 X. Gao, K. Li, Y. Xiao, J. Dai, Z. Shen, G. Lv and Y. Yang, *ChemistrySelect*, 2024, **9**, e202303466.
271 U. M. Zanger and M. Schwab, *Pharmacol. Ther.*, 2013, **138**, 103–141.
272 J. Wu, X. Guan, Z. Dai, R. He, X. Ding, L. Yang and G. Ge, *Coord. Chem. Rev.*, 2021, **427**, 213600.
273 S. N. de Wildt, G. L. Kearns, J. S. Leeder and J. N. van den Anker, *Clin. Pharmacokinet.*, 1999, **37**, 485–505.
274 K. Takayama, Y. Hagihara, Y. Toba, K. Sekiguchi, F. Sakurai and H. Mizuguchi, *Biomater.*, 2018, **161**, 24–32.
275 K. Takayama and H. Mizuguchi, *Drug Metab. Dispos.*, 2017, **32**, 12–20.
276 K. Takayama, R. Negoro, T. Yamashita, K. Kawai, M. Ichikawa, T. Mori, N. Nakatsu, K. Harada, S. Ito, H. Yamada, Y. Yamaura, K. Hirata, S. Ishida and H. Mizuguchi, *Cell. Mol. Gastroenterol. Hepatol.*, 2019, **8**, 513–526.
277 Y. Xie, J. Yao, W. Jin, L. Ren and X. Li, *Front. Cell Dev. Biol.*, 2021, **9**, 765980.
278 K. Hanaoka, T. Ikeno, S. Iwaki, S. Deguchi, K. Takayama, H. Mizuguchi, F. Tao, N. Kojima, H. Ohno, E. Sasaki, T. Komatsu, T. Ueno, K. Maeda, H. Kusuhara and Y. Urano, *Sci. Adv.*, 2024, **10**, eadi8847.
279 G. Kontopidis, C. Holt and L. Sawyer, *J. Dairy Sci.*, 2004, **87**, 785–796.
280 A. R. Madureira, C. I. Pereira, A. M. P. Gomes, M. E. Pintado and F. X. Malcata, *Food Res. Int.*, 2007, **40**, 1197–1211.
281 J. Ashley, R. D'Aurelio, M. Piekarska, J. Temblay, M. Pleasants, L. Trinh, T. Rodgers and I. Tothill, *Biosensors*, 2018, **8**, 32.
282 R. W. R. Crevel, J. L. Baumert, S. Luccioli, A. Baka, S. Hattersley, J. Hourihane, S. Ronsmans, F. Timmermans, R. Ward and Y. Chung, *Food Chem. Toxicol.*, 2014, **67**, 277–287.
283 T. Gadly, B. S. Patro and G. Chakraborty, *J. Mol. Liq.*, 2023, **391**, 123259–123267.
284 A. Host, *Ann. Allergy Asthma Immunol.*, 2002, **89**, 33–37.
285 S. C. Lee, J. Heo, H. C. Woo, J. A. Lee, Y. H. Seo, C. L. Lee, S. Kim and O. P. Kwon, *Chem. – Eur. J.*, 2018, **24**, 13706–13718.
286 M. K. Kuimova, S. W. Botchway, A. W. Parker, M. Balaz, H. A. Collins, H. L. Anderson, K. Suhling and P. R. Ogilby, *Nat. Chem.*, 2009, **1**, 69–73.
287 X. Yang, D. Zhang, Y. Ye and Y. Zhao, *Coord. Chem. Rev.*, 2022, **453**, 214336–214352.
288 K. Lubyphelps, *Curr. Opin. Cell Biol.*, 1994, **6**, 3–9.
289 A. P. Minton, *J. Biol. Chem.*, 2001, **276**, 10577–10580.
290 O. Nadiv, M. Shinitzky, H. Manu, D. Hecht, C. T. Roberts, D. Leroith and Y. Zick, *Biochem. J*, 1994, **298**, 443–450.

291 P. Mecocci, M. F. Beal, R. Cecchetti, M. C. Polidori, A. Cherubini, F. Chionne, L. Avellini, G. Romano and U. Senin, *Mol. Chem. Neuropathol.*, 1997, **31**, 53–64.
292 W. V. Humphreys, A. Walker and D. Charlesworth, *Br. J. Surg.*, 1976, **63**, 559–561.
293 W. T. Choo, M. L. Teoh, S. M. Phang, P. Convey, W. H. Yap, B. H. Goh and J. Beardall, *Front. Pharmacol.*, 2020, **11**, 1086.
294 G. Ciuffetti, G. Schillaci, R. Lombardini, M. Pirro, G. Vaudo and E. Mannarino, *Am. J. Hypertens.*, 2005, **18**, 1005–1008.
295 L. J. Tamariz, J. H. Young, J. S. Pankow, H. C. Yeh, M. I. Schmidt, B. Astor and F. L. Brancati, *Am. J. Epidemiol.*, 2008, **168**, 1153–1160.
296 P. E. Porporato, N. Filigheddu, J. M. Bravo-San Pedro, G. Kroemer and L. Galluzzi, *Cell Res.*, 2018, **28**, 265–280.
297 X. Dai, B. Dong, M. Ren and W. Lin, *J. Mater. Chem. B*, 2018, **6**, 381–385.
298 Y. Zhang, Z. Li, W. Hu and Z. Liu, *Anal. Chem.*, 2019, **91**, 10302–10309.
299 L. Tang, L. Zhou, X. Yan, K. Zhong, X. Gao, X. Liu and J. Li, *Dyes Pigm.*, 2020, **182**, 108644–108652.
300 L. Chen, Y. Feng, Y. Dang, C. Zhong and D. Chen, *Anal. Bioanal. Chem.*, 2020, **412**, 7819–7826.
301 M. Sun, T. Wang, X. Yang, H. Yu, S. Wang and D. Huang, *Talanta*, 2021, **225**, 121996–122003.
302 Y. Liang, Y. Zhao, C. Lai, X. Zou and W. Lin, *J. Mater. Chem. B*, 2021, **9**, 8067–8073.
303 S. Zhang, Y. Zhang, L. Zhao, L. Xu, H. Han, Y. Huang, Q. Fei, Y. Sun, P. Ma and D. Song, *Talanta*, 2021, **233**, 122592–122598.
304 C. Wang, T. Wang, M. Zhao, F. Dai, Z. Niu, W. Zhang and Y. Ma, *Dyes Pigm.*, 2021, **194**, 109593.
305 Y. Zhang, B. Xu, H. Chen, B. Fang, H. Wang and L. Hu, *Chem. Pap.*, 2021, **75**, 2517–2523.
306 G. Q. Fu, Q. T. Liao, Z. Q. Wang, Z. K. Tan, G. J. Mao, B. Yang and C. Y. Li, *Anal. Chim. Acta*, 2022, **1226**, 340192.
307 Y. Tang, J. Peng, Q. Zhang, S. Song and W. Lin, *Talanta*, 2022, **249**, 123647–123653.
308 H. Song, W. Zhang, Y. Zhang, C. Yin and F. Huo, *Chem. Eng. J.*, 2022, **445**, 136448–136454.
309 J. Cheng, Z. Li, L. Nong, P. Huang and W. Lin, *Anal. Chim. Acta*, 2022, **1221**, 340104.
310 X. Hao, J. Zhan, C. Geng and W. Lin, *Spectrochim. Acta A*, 2023, **284**, 121807–121813.
311 C. Zong, Q. Lu, J. Niu, F. Meng and X. Yu, *Spectrochim. Acta, Part A*, 2023, **299**, 122883.
312 Y. Ma, J. Niu, X. Liang, L. Wang, Y. Zhang, H. Lv, T. Wang, J. Wang, X. Zhang, S. Xu, Q. Zhu, Z. Jiang and W. Lin, *Chem. Eng. J.*, 2023, **464**, 142767.
313 W. Liu, T. Wang, L. Wang, Y. Wang, S. Hu and D. Tian, *Spectrochim. Acta, Part A*, 2024, **304**, 123329.
314 Q. Zhang, W. Liu, L. Jiang, Y. J. He, C. J. Wu, S. Z. Ren, B. Z. Wang, L. Liu, H. L. Zhu and Z. C. Wang, *Analyst*, 2024, **149**, 2956–2965.
315 L. Zhang, G. Li, H. Zheng and W. Lin, *New. J. Chem.*, 2024, **48**, 4565–4569.
316 J. J. Chao, H. Zhang, Z. Q. Wang, Q. R. Liu, G. J. Mao, Y. Li and C. Y. Li, *Anal. Chim. Acta*, 2024, **1285**, 342024-342031.
317 Y. Yang, R. Guo, K. Hu, M. Xu, T. Liang and W. Lin, *Luminescence*, 2024, **39**, e4749.
318 T. Zhang, F. Huo and C. Yin, *Sens. Actuators, B*, 2024, **404**, 135236.
319 L. Hu, J. Yang, C. Zhang, J. Pan, S. Shen, L. Su, X. Shen, J. He and H. Wang, *Sens. Actuators, B*, 2024, **398**, 134776.
320 B. Valeur and M. N. Berberan-Santos, *Molecular Fluorescence: Principles and Applications*, Wiley, Germany, 2013.
321 Z. Zhang, Z. Gou, B. Dong and M. Tian, *Sens. Actuators, B*, 2022, **355**, 131349–131357.
322 F. Meng, J. Niu, H. Zhang, R. Yang, Q. Lu, Y. Yu, Z. Liu, G. Niu and X. Yu, *Sens. Actuators, B*, 2021, **329**, 129148–129156.
323 M. Cao, T. Zhu, M. Zhao, F. Meng, Z. Liu, J. Wang, G. Niu and X. Yu, *Anal. Chem.*, 2022, **94**, 10676–10684.
324 X. C. Feng, G. Zhang, R. Sun, Y. J. Xu and J. F. Ge, *Sens. Actuators, B*, 2023, **394**, 134469–134477.
325 Y. Q. Zhao, L. Yu, L. Zhu, J. Liang, Y. Zhou and J. S. Kim, *CCS Chem.*, 2024, **6**, 733–748.
326 H. M. Wang, Y. C. Li, L. L. Sun, M. Y. Tang, J. Liu, J. Cai, L. Dong, J. Li, Y. Zang, H. H. Han and X. P. He, *Chin. Chem. Lett.*, 2024, **35**, 109603.
327 H. M. Wang, L. Dong, Q. L. Hao, L. L. Sun, X. R. Li, Y. W. Yuan, M. Y. Tang, J. Gong, Y. Zang, J. Li, T. D. James, X. P. He and H. H. Han, *Adv. Funct. Mater.*, 2025, e25887, DOI: **10.1002/adfm.202425887**.
328 K. L. He, L. L. Sun, W. J. Li, L. Dong, C. L. Ding, M. C. Tan, K. X. Zhang, J. Gong, L. Zhang and H. H. Han, *Sci. China Chem.*, 2025, **68**, 5086–5096, DOI: **10.1007/s11426-025-2730-2**.
329 C. Duangkamol, P. Muangsopa, S. Rattanopas, P. Wongsuwan, T. Khrootkaew, P. Chueakwon, N. Niamnont, K. Chansaenpak and A. Kamkaew, *Dyes Pigm.*, 2023, **216**, 111365.
330 Y. Zhou, Q. Wang, S. Chanmungkalakul, X. Wu, H. Xiao, R. Miao, X. Liu and Y. Fang, *Chem. – Eur. J.*, 2024, **30**, e202303707.
331 K. Hanaoka, S. Iwaki, K. Yagi, T. Myochin, T. Ikeno, H. Ohno, E. Sasaki, T. Komatsu, T. Ueno, M. Uchigashima, T. Mikuni, K. Tainaka, S. Tahara, S. Takeuchi, T. Tahara, M. Uchiyama, T. Nagano and Y. Urano, *J. Am. Chem. Soc.*, 2022, **144**, 19778–19790.
332 H. Niu, J. Liu, H. M. O'Connor, T. Gunnlaugsson, T. D. James and H. Zhang, *Chem. Soc. Rev.*, 2023, **52**, 2322–2357.
333 L. Zhao, X. He, Y. Huang, S. Zhang, H. Han, L. Xu, X. Wang, D. Song, P. Ma and Y. Sun, *Anal. Bioanal. Chem.*, 2020, **412**, 7211–7217.
334 L. L. Li, K. Li, M. Y. Li, L. Shi, Y. H. Liu, H. Zhang, S. L. Pan, N. Wang, Q. Zhou and X. Q. Yu, *Anal. Chem.*, 2018, **90**, 5873–5878.
335 Y. Yuan, S. Xiong, L. Lv, W. Hu, X. Xiong, C. Li and H. Deng, *Chem. Eng. J.*, 2023, **471**, 144341–144349.
336 F. Han, S. A. Abedi, S. He, H. Zhang, S. Long, X. Zhou, S. Chanmungkalakul, H. Ma, W. Sun, X. Liu, J. Du, J. Fan and X. Peng, *Adv. Sci.*, 2024, **11**, 2305761–2305771.
337 J. Luo, Z. Xie, J. W. Y. Lam, L. Cheng, H. Chen, C. Qiu, H. S. Kwok, X. Zhan, Y. Liu, D. Zhu and B. Z. Tang, *Chem. Commun.*, 2001, 1740–1741.

338 Y. Li, Z. Cai, S. Liu, H. Zhang, S. T. H. Wong, J. W. Y. Lam, R. T. K. Kwok, J. Qian and B. Z. Tang, *Nat. Commun.*, 2020, **11**, 1255–1264.
339 Z. L. Lai, J. S. Chang, Y. C. Chan, C. C. Chang, C. Y. Li and S. W. Huang, *Sens. Actuators, B*, 2021, **330**, 129269–129280.
340 S. T. Zeng, W. Shao, Z. Y. Yu, L. Fang, G. X. Tang, Y. Y. Fang, S. B. Chen, Z. S. Huang, J. H. Tan and X. C. Chen, *ACS. Sens.*, 2022, **8**, 40–50.
341 R. Miao, J. Li, C. Wang, X. Jiang, Y. Gao, X. Liu, D. Wang, X. Li, X. Liu and Y. Fang, *Adv. Sci.*, 2022, **9**, 2104609–2104617.
342 C. Wang, J. Wang, K. Xue, M. Xiao, K. Wu, S. Lv, B. Hao and C. Zhu, *Anal. Chem.*, 2022, **94**, 3303–3312.
343 H. Sun, X. X. Tang, B. X. Miao, Y. Yang and Z. Ni, *Sens. Actuators, B*, 2018, **267**, 448–456.
344 J. J. Lee, J. Kang and C. Kim, *J. Hazard. Mater.*, 2024, **465**, 133168–133182.
345 F. Gao, C. Y. Wang, Y. Chen, F. Z. Xu, J. W. Zou, Z. Q. Guo and W. H. Zhu, *Green Chem. Eng.*, 2023, **4**, 448–453.
346 H. Wang, H. Zheng, W. Zhang, L. Yang, M. Yu and Z. Li, *Sens. Actuators, B*, 2023, **394**, 134347.
347 X. M. Liu, D. X. Ma and X. H. Ju, *MRS Commun.*, 2023, **13**, 634–640.
348 B. Das, M. Dolai, A. Dhara, A. Ghosh, S. Mabhai, A. Misra, S. Dey and A. Jana, *J. Phys. Chem. A*, 2021, **125**, 1490–1504.
349 M. Chen, W. Chen, Q. Zhu, L. Yang, X. Zhang, D. Xie, J. Chen, Y. Wu, Y. Zhu and M. Zhu, *J. Fluoresc.*, 2025, **35**, 2203–2214.
350 A. Pramanik, R. Das, P. J. Boruah, S. Majumder and S. Mohanta, *Spectrochim. Acta A*, 2024, **308**, 123780–123792.
351 S. Zhong, S. Huang, B. Feng, T. Luo, F. Chu, F. Zheng, Y. Zhu, F. Chen and W. Zeng, *Org. Biomol. Chem.*, 2023, **21**, 5063–5071.
352 B. Xia, F. Ren, X. Ma, Z. C. Yang, Z. L. Jiang, W. W. Fang, N. W. Wang, J. L. Hu, W. D. Zhu, T. He, Q. Li, B. Q. Cao and Z. Li, *Adv. Healthc. Mater.*, 2024, **13**, 2400760–2400769.
353 L. Zong, C. Wang, Y. Song, Y. Xie, P. Zhang, Q. Peng, Q. Li and Z. Li, *Sens. Actuators, B*, 2017, **252**, 1105–1111.
354 X. Wang, L. Wang, T. Jin, K. Sun and J. Yang, *Sens. Actuators, B*, 2023, **375**, 132935–132941.
355 H. Wang, Y. Sun, X. Lin, W. Feng, Z. Li and M. Yu, *Chin. Chem. Lett.*, 2023, **34**, 107626–107630.
356 M. Fu, K. Wang, J. Xue, Y. Li, M. Bian and Q. Zhu, *Org. Biomol. Chem.*, 2022, **20**, 3359–3364.
357 P. Zhang, X. Guo, J. Gao, H. Liu, C. Wan, J. Li, Q. Zhang, Y. Song and C. Ding, *ACS Sens.*, 2021, **6**, 4225–4233.
358 Y. L. Qi, H. R. Wang, L. L. Chen, B. Yang, Y. S. Yang, Z. X. He and H. L. Zhu, *Anal. Chem.*, 2022, **94**, 4594–4601.
359 R. Li, J. Guo, Y. Duan, X. Liu, L. Gui, Y. Xu, X. Kong, Y. Li, H. Chen and Z. Yuan, *Chem. Eng. J.*, 2022, **435**, 135043–135055.
360 J. Liu, X. Xu, P. Xie, X. Yang, Y. Ye and Y. Zhao, *Sens. Actuators, B*, 2023, **396**, 134594.
361 X. Zhang, H. Yan, F. Huo, J. Chao and C. Yin, *Sens. Actuators, B*, 2021, **344**, 130244–130251.
362 M. Ren, B. Deng, K. Zhou, X. Kong, J. Y. Wang and W. Lin, *Anal. Chem.*, 2017, **89**, 552–555.
363 Y. Huang, M. Li, Q. Zan, R. Wang, S. Shuang and C. Dong, *Anal. Chem.*, 2023, **95**, 10155–10162.
364 V. Kathuria, Kiran, P. Rani, Mayank, G. Joshi, R. Kumar, J. Sindhu, P. Kumar, A. Negi and S. Kumar, *J. Photochem. Photobiol.*, 2023, **443**, 114841.
365 P. Lei, M. Li, C. Dong and S. Shuang, *ACS Biomater. Sci. Eng.*, 2023, **9**, 3581–3589.
366 X. Ma, X. Zhang, B. Zhang, D. Yang, H. Sun, Y. Tang and L. Shi, *Food Chem.*, 2024, **430**, 136930.